

Abstract

OWEN, MICHAEL PARKER. Hydrodynamics of Mass Transfer and Accretion in Close Binary Systems With Compact Objects. (Under the direction of John M. Blondin)

Most stars are formed in binary or multiple systems. Many of these stars will undergo some period of mass transfer at some point during their lifetimes. Hence it is useful to understand the dynamics of mass transfer in binary star systems in order to better understand the current population of stars in the Galaxy and their evolution. A natural class of objects for study are the close binaries that contain compact objects such as neutron stars and black holes. These systems are bright X-ray emitters, allowing us to study the circumstellar gas within them. We use numerical hydrodynamic modeling to study mass transfer processes in the high-mass X-ray binaries, including the evolutionary sequence between wind fed and disk fed systems, elliptical orbit X-ray binaries, and the global dynamics of LMC X-4 in 3D. We also investigate the properties of high resolution 3D accretion disks, including transport via global waves modes, the effects of tidal stream impact, and the fluid response of tilted disks.

Hydrodynamics of Mass Transfer and Accretion in Close Binary Systems With Compact Objects

BY
MICHAEL P. OWEN

A DISSERTATION SUBMITTED TO THE GRADUATE FACULTY OF
NORTH CAROLINA STATE UNIVERSITY
IN PARTIAL FULFILLMENT OF THE
REQUIREMENTS FOR THE DEGREE OF
DOCTOR OF PHILOSOPHY

DEPARTMENT OF PHYSICS

RALEIGH
SEPTEMBER 2003

APPROVED BY:

CHAIR OF ADVISORY COMMITTEE

Dedication

To Rachel, with all my love.

Biography

Michael Parker Owen was born in La Jolla, California on January 21, 1972, the youngest of the six children of Robert Craft Owen and Betty Parker Owen. At a very young age he moved with his family to Wilmington, North Carolina, where he mis-spent his youth before graduating E. A. Laney High School in 1990. He went on to acquire a Bachelor of Science degree in physics with a minor in mathematics from North Carolina State University in 1994, graduating *magna cum laude*. Michael worked briefly for the NC State astrophysics group as an undergraduate, and returned to the astrophysics group as a graduate student to pursue research on accretion disks in High Mass X-Ray Binaries (HMXBs) such as LMC-X4. He received his Option B, or *en route*, Master's degree in the fall of 1998, before leaving academia for the greener pastures and finances of the real world, working as both a requirements engineer and a technical analyst. Three years later he fled the real world to return to what he really enjoyed, teaching and research, in order to complete this degree program. Michael lives in Durham, North Carolina with his beautiful wife Rachel, four dogs, two cats, and a partridge in a pear tree.

Acknowledgments

I would like to thank my adviser, Dr. John Blondin who, lo these many years, has put up with more than any reasonable adviser should be expected to. His guidance and understanding of astrophysics has made this project possible, and I am truly grateful.

I would like to thank my family, including my father (who has never ceased to believe in me), my mother (who finally convinced me that I was, indeed, just putting one over on the taxpayers with this astrophysics stuff), my Aunt Rita (who came to my rescue at a critical time in a manner I have not forgotten), and my brother Greg (who seems genuinely proud to have an astrophysicist for a brother).

I would also like to thank the other members of my committee, who were chosen because I felt they had the greatest positive impact on me during my long, long, *long* tenure at NC State.

Most importantly, I would like to thank my beautiful wife Rachel, who has supported me in every conceivable way; emotionally, financially, even politically. She is the light of my life, without whom I would not have had the strength to return and finish what I'd stated so many years ago.

Table of Contents

List of Figures	vii
1 Introduction	1
1.1 Accretion as a Power Source	2
1.1.1 The Spectrum to Expect	3
1.1.2 The Effect of the Luminosity on the Flow	5
1.2 Accretion in Binary Systems	7
1.2.1 Wind Accretion in Detached Binaries	10
1.2.2 Roche Lobe Overflow	12
1.2.3 Binary Evolution	14
1.3 Accretion Disks	15
1.3.1 Viscous Transport	16
1.3.2 Non-Viscous Transport by Global Waves Modes	21
1.3.3 Tilted Disks, Precession, & Radiation Torque	24
1.4 Observing Accretion onto Compact Objects in Close Binaries	29
1.4.1 Nomenclature	29
1.4.2 Geometric Considerations	30
1.4.3 Observational Techniques	31
1.4.4 Kinds of Accreting Close Binaries with Compact Objects	36
1.4.5 Observations	39
1.5 This Work	44
2 Computational Fluid Dynamics	48
2.1 The Equations of Fluid Dynamics	48
2.1.1 The Equation of State	50
2.1.2 Eulerian <i>vs.</i> Lagrangian Coordinates	51
2.2 Numerical Methods	52
2.2.1 Finite Differences	52
2.2.2 The Riemann Problem	53
2.2.3 The Piecewise-Parabolic Method	54
2.2.4 Lagrangian Remap	54
2.2.5 Initial & Boundary Conditions	55

2.3	Grid Forces and Fictitious Forces	56
2.3.1	Curvilinear Coordinates	57
2.3.2	Rotating Frames	59
2.4	Parallel Decomposition Using MPI	60
3	Mass Transfer in High Mass X-ray Binaries	62
3.0.1	Wind Accretion and Roche Lobe Overflow (RLOF)	62
3.0.2	Elliptical Orbit XRBs	65
3.0.3	3D Global Hydrodynamic Modeling of LMC X-4	69
3.1	Numerical Model	72
3.1.1	Modifications for Elliptical Orbits	78
3.1.2	Modifications for 3D Simulations	80
3.2	Results	82
3.2.1	Wind Accretion and RLOF	82
3.2.2	Elliptical-Orbit Binary Stars	86
3.2.3	Hydrodynamic Modeling of LMC X-4	96
4	3D Hydrodynamic Disks	109
4.0.4	Local and Global Transport	110
4.0.5	Effects of the Stream Impact	114
4.0.6	Tilted Disks	114
4.1	An Idealized Disk Model	116
4.2	Computational Method	118
4.3	Numerical Simulations	121
4.3.1	Vertical Shock Structure and Dynamics	122
4.3.2	Tidal Bulging of the Outer Disk	128
4.3.3	Epicyclic Motions	130
4.3.4	$n = 3$ and $n = 15/8$	131
4.4	Transport	133
4.4.1	Tidal Stream	136
4.4.2	Tilted Disks	143
4.5	Discussion	149
5	Conclusions	154
5.1	Mass Transfer and Accretion in High Mass X-Ray Binaries	154
5.1.1	Wind Accretion <i>vs.</i> Roche Lobe Overflow	154
5.1.2	Mass Transfer in Elliptical Orbit X-Ray Binaries	155
5.1.3	Global Hydrodynamic Simulations of LMC X-4	156
5.2	3D Hydrodynamic Disks	157
	Bibliography	161

List of Figures

1.1	The X-Ray Sky	5
1.2	Geometry of a Binary Star	9
1.3	Binary Configurations	10
1.4	Wind Accretion in a Detached Binary	11
1.5	Roche Lobe Overflow in a Semi-detached Binary	13
1.6	Viscous Transport of Angular Momentum	18
1.7	Geometry of an Accretion Disk	23
1.8	Radiatively Driven Warping	28
1.9	Observational Classes Due to Inclination	30
1.10	Eclipse Mapping	34
1.11	Line Profiles	35
2.1	Piecewise-Parabolic Fluid Variable Re-construction	54
2.2	The 1D Hydrodynamic Solver	55
3.1	L_x as a Function of Roche Lobe Overflow	83
3.2	$L_x(t)$ for Full RLOF, Wind Accreting, and Transitional Cases	85
3.3	Slow Rotator	87
3.4	J, \dot{J}, L_x for the Slow Rotator	89
3.5	Fast Rotator	90
3.6	J, \dot{J}, L_x for the Fast Rotator	92
3.7	The Global Hydrodynamic Model of LMC X-4	97
3.8	Time Series of the Circumstellar Gas	98
3.9	The Five Key System Components	99
3.10	The Accretion Disk	101
3.11	The Disk Wind	103
3.12	Disk Wind and the Circumstellar Gas	105
4.1	Computational Domain	119
4.2	Spirals Waves in the Disk	122
4.3	The Disk at Early Time	123
4.4	The Disk at Late Time	124
4.5	Formation and Vertical Instability of Spiral Shocks	126

4.6	The Vertical Ram Pressure Gradient Instability	127
4.7	Evolution of the disk	129
4.8	Tidal Bulging of the Outer Disk	130
4.9	Epicyclic Motions of the Disk Interior	132
4.10	All Cases at Late Time	133
4.11	$\alpha_{\dot{M}}(t)$	134
4.12	$\alpha_{\dot{L}}(t)$	134
4.13	$\alpha_{W_{R\phi}}(t)$	135
4.14	$\alpha_{W_{R\phi}}(t)$ at Small Radii	135
4.15	Space-time Diagram of $\alpha_{\dot{M}}(R, t)$ fo $n = 3$	137
4.16	Space-time Diagram of $\alpha_{\dot{M}}(R, t)$ for $n = 0$	138
4.17	Period Doubling Behavior	139
4.18	Disks With Tidal Stream	141
4.19	α With Tidal Stream, $n = 0$	142
4.20	α With Tidal Stream, $n = 15/8$	144
4.21	Morphology of the Tilted Disks	145
4.22	Precession of the Tilted Disks	147
4.23	Evolution of the Tilt Angle	148

Chapter 1

Introduction

Consider a roller coaster. All the way through your clanking, groaning ascent to the top of the first peak, you, your fellow passengers, and the very car you're riding in are being imbued with energy, gravitational potential energy. After cresting, you begin your gut-wrenching descent. The gravitational potential energy stored within you is quickly turned into kinetic energy as you roar around the coaster (not to mention some of the chemical energy you stored up at breakfast being turned into acoustic energy as you scream your head off). As you alternately climb and descend your allotted quantity of energy is sloshed back and forth between kinetic and potential, all the while being gradually eaten away, *dissipated*, by the friction of the wheels on the track heating both up, the drag of the air you blast through robbing you to move the air, the roar of the car being carried away on the wind. In the end, all of your last remaining supplies of your original gravitational potential energy are abruptly ripped away in a squeal of brakes as you stop. All of your original gravitational potential energy has been liberated and dissipated. Your mass has been added to that of the Earth, and the energy that kept

you separate from her is now gone. This, essentially, is *accretion*.

Accretion according to the dictionary is “Growth or increase in size by gradual external addition,” but we are more interested in the liberation of energy that occurs during this process, in other words, we are interested in accretion as a *power source*. In astrophysics, many luminous sources are powered by accretion, including protostars, cataclysmic variables, X-ray binaries, γ -ray bursters, quasars, active galactic nuclei, etc. For our purposes, we will be concentrating on the accretion of material onto a compact star, such as a white dwarf, neutron star, or black hole.

1.1 Accretion as a Power Source

Consider a particle of mass m at a large distance r from a star of mass M and radius R . The gravitational potential energy of the particle due to the star is $-GMm/r$, where G is Newton’s universal gravitational constant. If the particle is allowed to fall freely to the surface of the star, its gravitational potential energy will decrease to $-GMm/R$. The difference is the amount of gravitational potential energy liberated during the fall, which is converted into the kinetic energy of the falling particle. For $r \gg R$, the energy liberated becomes:

$$\Delta E = -\frac{GMm}{R}.$$

If we now “rain” material onto the star at a rate $\dot{M} \equiv dM/dt$ the energy liberated per unit time is:

$$L_{acc} = \frac{dE}{dt} = -\frac{GM\dot{M}}{R}.$$

This is the *accretion luminosity*. We see that the accretion luminosity depends on two parameters, the compactness of the accretor M/R , and the mass accretion rate \dot{M} , and can be tremendously efficient at liberating energy. The maximum amount of energy that can be liberated from an amount of mass is given by Einstein's relation $E = mc^2$, if the mass is *entirely* converted into energy via annihilation. The maximum luminosity is then $L_{\max} = \dot{m}c^2$. Any other process such as nuclear fission, fusion, or accretion will have some efficiency η with which it can liberate energy, $L = \eta\dot{m}c^2$. The efficiency of thermonuclear fusion of hydrogen is 0.007, whereas the efficiency of accreting onto a stellar mass black hole or the surface of a neutron star is about 0.1; accretion onto such a compact object is 15–20 times more efficient as a power source than is nuclear fusion. Accretion onto super-massive ($M \gtrsim 10^9 M_\odot$) black holes in AGN and quasars (whose luminosities approach and exceed 10^{47} erg sec⁻¹) requires an accretion rate of approximately $20M_\odot \text{ yr}^{-1}$, compared to the burn rate of $250M_\odot \text{ yr}^{-1}$ required by nuclear fusion. Considering that these sources vary on a timescale of weeks or days, they must be contained in a volume smaller than our solar system. We see that accretion is the only viable candidate to power these objects.

1.1.1 The Spectrum to Expect

It is important to know what we can observe about these sources, what to look for. Typically, we expect the material being accreted is a gas; it will emit some characteristic spectrum of radiation depending on the properties of the flow. If the emitted radiation has time to come into equilibrium with the gas (*i.e.* if the gas is optically thick, trapping

the photons for a long time), then the emitted spectrum would be that of a blackbody of temperature

$$T_{BB} = (L_{acc}/4\pi R_{\star}^2\sigma)^{1/4}.$$

Note the dependence on the mass accretion rate (implicit in the accretion luminosity L_{acc}); the more stuff accretes, the hotter it gets, which makes sense, since you are liberating energy at a higher rate. If, on the other hand, the released energy is converted entirely into thermal energy and the photons immediately escape (*i.e.* the gas is optically thin), the thermal energy of each hydrogen atom in the gas, $\frac{3}{2}kT$ for the protons plus another $\frac{3}{2}kT$ for the electrons, is equal to the gravitational potential energy released:

$$2 \times \frac{3}{2}kT_{Th} \approx \frac{GMm_p}{R}.$$

Hence the gas will be at the thermalized temperature $T_{Th} = GMm_p/3kR$. Lastly, we will define the radiation temperature as the temperature corresponding to the energy of an average photon: $h\bar{\nu} = kT_{rad}$, or $T_{rad} = h\bar{\nu}/k$.

The emitted spectrum will then have a radiation temperature that falls somewhere between the two extremes, the optically thick blackbody case, and the optically thin thermal emission case: $T_{BB} \leq T_{rad} \leq T_{Th}$. Using numbers for an accreting neutron star, we find the minimum (blackbody) temperature to be about 10^7 K, and the maximum optically thin temperature to be about 6×10^{11} K. Hence we expect emission primarily in the X-ray to γ -ray:

$$1 \text{ keV} \leq h\bar{\nu} \leq 50 \text{ MeV}.$$

X-rays and γ -rays cannot penetrate the Earth's atmosphere, so ground-based detection is not an option. Extra-solar X-ray sources were first discovered in the 1960s

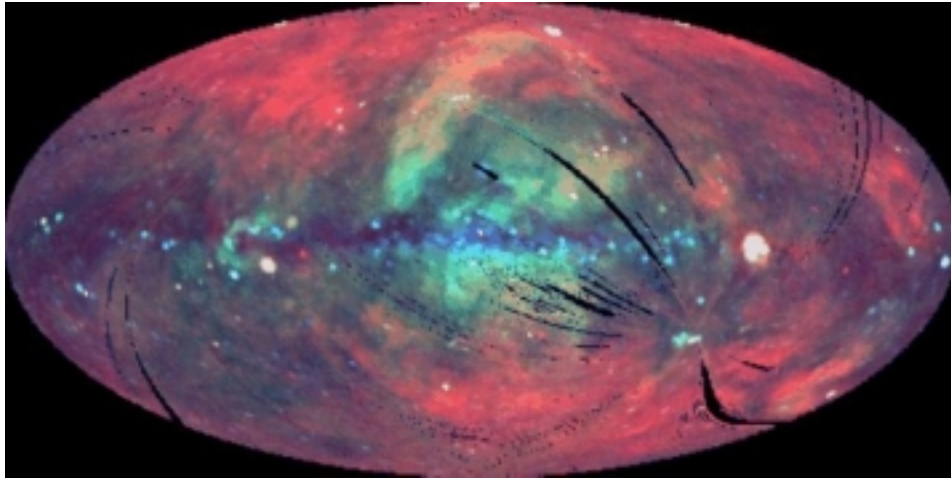


Figure 1.1: The sky in X-rays. From the ROSAT mission, NASA. Astronomy Picture of the Day.

with rocket-borne X-ray detectors. In 1962 American Science and Engineering (AS&E) discovered the cosmic X-ray source Scorpius X-1, the very first extra-solar X-ray point source to be discovered, using a rocket launched detector. Dedicated X-ray telescope launches blossomed in the 1970s with satellite such as Ariel 5, HEAO-1, SAS-3, OSO-8, Uhuru, and arguably the most important, Einstein, launched in 1978. Ever more sensitive X-ray telescopes have continued to be developed and launched, culminating in recent years with satellites such as ASCA, EXOSAT, Ginga, RXTE, and ROSAT. These missions show our galaxy and its neighbors to be veritable hives of X-ray sources, as in Figure 1.1.

1.1.2 The Effect of the Luminosity on the Flow

We have calculated that an intense flux of high energy photons will be produced by accretion onto a compact star. This tremendous luminosity can have a feedback effect

on the accretion flow via three mechanisms: 1) radiation pressure, 2) heating (or cooling), 3) photoionization. For now, let us assume that the in-falling gas is entirely hydrogen. The intense X-ray flux will heat the gas via scattering. If the gas becomes hot enough, the radiation will *photoionize* the gas, stripping the atoms of their electrons, creating essentially a two-fluid plasma of ions and electrons. The radiation then exerts a force on the free electrons via Thompson scattering; the electrons in turn drag the ions along via Coulomb attraction. This radiation pressure acts to oppose the force of gravity such that the net force felt by the ions (which contain most of the mass of the gas) is lowered in proportion to the luminosity:

$$F_G = \left(GMm_p - \frac{L\sigma_T}{4\pi c} \right) \frac{1}{r^2},$$

where m_p is the mass of the proton (*i.e.* an ionized hydrogen atom), c is the speed of light, and σ_T is the cross section for Thompson scattering, assuming the gas is fully ionized.

Because of this feedback, the radiation pressure due to the accretion luminosity acts as a throttle to the mass accretion rate. The inward force felt by a parcel of gas vanishes for a particular value of the luminosity:

$$L_{Edd} = \frac{4\pi GMm_p c}{\sigma_T},$$

the *Eddington limit*.

This condition need not hold in physical systems where the accretion is not spherically symmetric, for example if accretion were to occur primarily at the star's equator while radiation was emitted primarily at the poles, or if the accretion is non-steady. However,

it does provide a rough estimate for the maximum luminosity of a star of a given mass. For example, it can be shown that the maximum accretion luminosities of accreting compact stars such as white dwarfs and neutron stars (both about the mass of the Sun) are about 10^{38} erg s^{-1} . For comparison, the luminosity of the Sun, due to thermonuclear fusion rather than accretion, is 3.89×10^{33} erg sec^{-1} .

1.2 Accretion in Binary Systems

So, do we observe compact X-ray sources that could be attributed to accretion onto compact stars? Indeed we do; we find them in *close binary star systems*. They come in several flavors, the so-called cataclysmic variables (CVs), which are believed to be accreting white dwarfs and emit primarily in the extreme ultraviolet and soft X-ray, and the X-ray binaries (XRBs), which are believed to be accreting neutron stars and black holes, which emit primarily in the X-ray. All of these bright sources have companion stars feeding them their requisite mass accretion rates \dot{M} via various mechanisms of mass transfer. To understand the mass transfer and types of accretion processes in these systems, let us consider their geometry.

For simplicity, we shall restrict ourselves (for now) to the case of two stars in circular orbit around each other with the mass donor rotating synchronously with the binary orbit. Circularization of the orbit and synchronous rotation within a close binary system are expected due to tidal forces between the two stars. Consider two stars of masses M_1 and M_2 in circular orbit with binary separation a . Kepler's law yields an orbital period

of:

$$P^2 = \frac{4\pi^2 a^3}{G(M_1 + M_2)}.$$

It is convenient to examine this system using a frame of reference that rotates with the binary orbit. This frame rotates with an angular frequency given by:

$$\omega^2 = \frac{G(M_1 + M_2)}{a^3}.$$

In this frame we may write an expression for the *effective potential* felt by a parcel of gas. This includes the gravitational potential of the two stars, as well as the centrifugal potential due to the rotating frame. The effective potential can then be written:

$$\Phi_{\text{eff}}(\mathbf{r}) = -\frac{GM_1}{r_1} - \frac{GM_2}{r_2} - \frac{1}{2}\omega^2 r_{cm}^2,$$

where r_1 , r_2 , and r_{cm} are the distances to M_1 , M_2 , and the binary center of mass, respectively. This is called the *Roche potential*. There exists along the line of centers connecting M_1 and M_2 a point where the effective potential has zero slope, and hence the net force vanishes. This is called the *inner Lagrange point*, or L1. It is a saddle point in the Roche potential, being a maximum along the line of centers, but a minimum transverse to it. This means that a particle displaced to the side of the L1 point will experience a restoring force, but a particle displaced toward one of the two masses will accelerate toward that mass. The value of the effective potential at L1 defines the *critical potential*; an equipotential surface of this potential is composed of two lobes, known as Roche lobes, connected at the L1 point like an hourglass or dumbbell. The L1 point acts as a throat where material can more easily move from one lobe to the other.

The particular geometry of the Roche lobes, *i.e.* their relative sizes, is determined

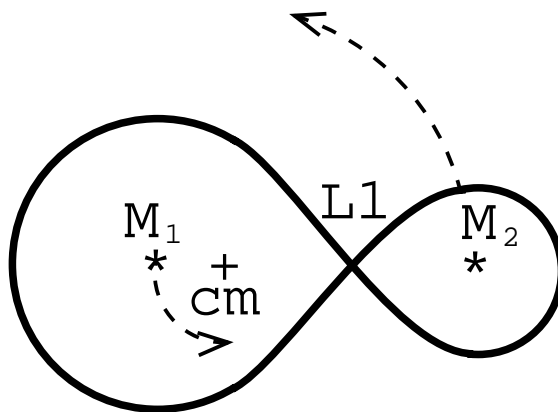


Figure 1.2: Stars M_1 and M_2 rotate about their common center of mass cm . The critical surface of the effective potential forms the figure-8 shaped Roche lobes, connected at the inner Lagrange point, $L1$.

only by the mass ratio $q \equiv M_2/M_1$, and the orbital angular frequency ω . Depending on the sizes of the two stars relative to their respective Roche lobes, we can classify three distinct types of binary: contact, detached, and semi-detached. For our discussion, we will always take the accreting star to be M_1 and the donor star to be M_2 .

A contact binary occurs when both stars are large enough that they fill their Roche lobes and their surfaces are essentially in contact; such systems are not expected to survive very long in this state before evolving toward a common stellar envelope, and becoming a single star.

Most binary systems are detached binaries. Neither star fills its Roche lobe. This does not mean that mass cannot be transferred between the two; for example, if one star possesses a stellar wind, this wind could be gravitationally focused and accreted by its companion; this mechanism of mass transfer is called wind accretion.

In a semi-detached binary, one star fills its Roche lobe while the other does not.

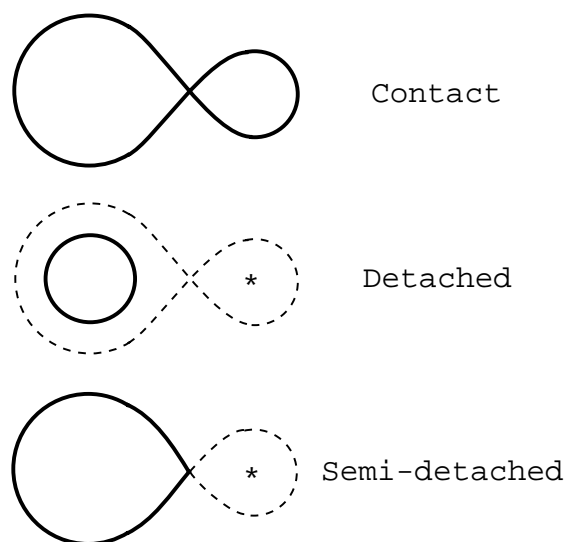


Figure 1.3: Contact binaries have surfaces that are in contact with each other, while detached binaries surfaces are well within their Roche lobes. Semi-detached binaries have only one lobe-filling star.

Material can escape from the envelope of the lobe-filling star (the donor) through the L1 saddle point and fall toward the other star (the accretor). This is commonly referred to as Roche lobe overflow (RLOF).

1.2.1 Wind Accretion in Detached Binaries

If a star of mass M is placed in a uniform wind of density ρ moving at speed u , gravitational attraction will focus a column of wind onto the accreting star. The size of the accretion cylinder is determined by the speed of the flow and the mass of the accretor; in order for gas to accrete it must have kinetic energy less than the gravitational binding energy at its (undeviated) point of closest approach:

$$\frac{1}{2}u^2 = \frac{GM}{r_{\text{acc}}}.$$

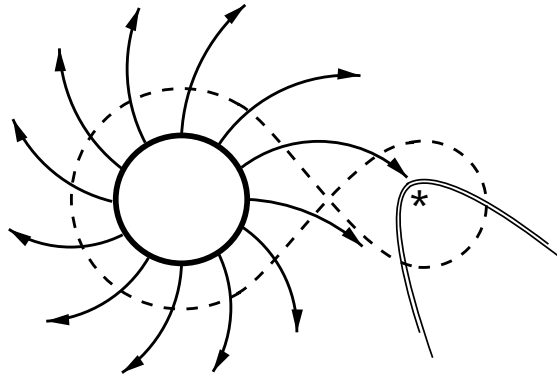


Figure 1.4: The stellar wind from the donor star (trailing in the rotating frame due to conservation of angular momentum) in this detached binary is gravitationally captured by a compact accretor, forming a bow shock.

The mass accretion rate is then $\rho u \pi r_{\text{acc}}^2$:

$$\dot{M}_{\text{wind}} = \frac{4\pi\rho(GM)^2}{u^3}. \quad (1.1)$$

This is called *Bondi-Hoyle* accretion [Bondi and Hoyle, 1944].

In the case of a wind fed accretor within a binary system, we expect deviations from this ideal, as we expect there to be gradients in the density and velocity of the wind [Taam and Fryxell, 1988]. Also, we generally expect the flow to be supersonic, implying that a bow shock will develop ahead of the accreting star. The bow shock may effect the accretion rate, as some of the kinetic energy will be dissipated crossing the shock, meaning that a larger gas column may accrete, but back pressure behind the bow shock may be strong enough to choke accretion. The precise result will of course depend on the detailed dynamics of the interacting wind and shock, including radiative heating and cooling [Taam et al., 1991]. In the ideal case, we expect no net accumulation of angular momentum on the accretor, but again transverse gradients in density and velocity may

change this. Still, Equation 1.1 provides a rough constraint on the wind for systems whose luminosity is believed to be powered by wind accretion.

1.2.2 Roche Lobe Overflow

Lubow and Shu [1975] and Lubow and Shu [1976] form the foundation of our understanding of mass transfer in semi-detached binaries. In these systems, the surface of the Roche-filling star is essentially unbound at the L1 point; the thermal gas pressure will force material through the saddle point in the Roche potential at the sound speed (implying that as the stream accelerates toward the accretor the flow is always supersonic). We thus expect the formation of a stream of material from the surface of the donor star. We call this the *tidal stream*. From the accreting star's point of view, the L1 point lies at a distance r_{L1} that depends on the mass ratio of the system, and rotates about the accretor with angular velocity ω . The gas then contains an angular momentum per unit mass given by ωr_{L1}^2 . In other words, this stream of material cannot fall straight into the accreting star; it is in orbit.

Without interference, a particle released from the L1 point will follow a ballistic path around the accretor, passing closest to it at some periastron point. If the radius of the accretor is smaller than the radius of this periastron, the stream gas will continue to orbit, eventually intersecting other stream material. We may expect these colliding gas flows to circularize at a radius given by a Keplerian orbit with specific angular momentum ωr_{L1}^2 :

$$\ell = r_{circ}v_{\phi} = (GM_1r_{circ})^{1/2} = \omega r_{L1}^2.$$

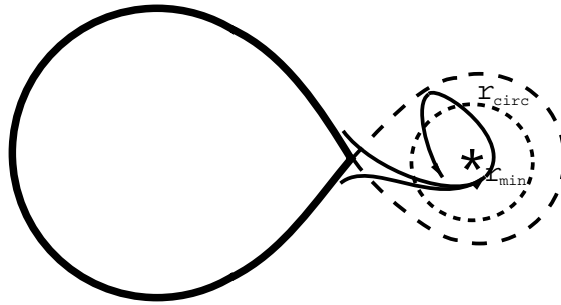


Figure 1.5: The photosphere of the donor star is unbound at the L1 point, and forms a gas stream that pours into the compact star's Roche lobe. This stream enters the Roche lobe at the sound speed (since it is gas pressure that pushes it through the L1 point), and accelerates toward the accretor. The supersonic flow follows a ballistic trajectory, passing the compact star at a radius r_{\min} before colliding and circularizing at radius r_{circ} .

For example, in a system with $q = 1$ (equal mass stars), where $r_{L1}/a = 1/2$, $r_{\text{circ}}/a = 1/8$. If angular momentum were conserved this gas would form a torus at the circularization radius. If angular momentum can diffuse outward while gas can drift inward, then a disk is formed. This configuration is known as an *accretion disk*.

For the case of accretion onto a compact object, the point of closest approach of the stream is less than the circularization radius of the incoming material; it stands to reason that the stream will have to strike the disk in these systems. Since the gas stream starts out its journey from the L1 point moving at the sound speed (remember, it leaks through the L1 point due to thermal pressure from the donor's photosphere) and is in free fall toward the accretor, we expect the stream material to be supersonic when it strikes the disk. We may expect strong shocks at this high velocity impact, heating the gas via dissipation, creating a hot spot. However, this may not always be the case; if the impact is sufficiently oblique, or the ratio of the density of the disk to the stream is sufficiently large (which it may well be, since for a steady state disk we expect the

disk to accrete matter slowly), or the gas stream is only just supersonic (as may be the case in very low mass ratio systems, where the disk may extend nearly to the L1 point) then emission by a hot spot may be diminished. Splashing of stream material at the disk edge, or expansion of the disk edge due to heating by the stream impact, may contribute to phase-dependent modulation of flux from the accretor by increasing the column density of material along our line of sight to the source at certain phases.

1.2.3 Binary Evolution

Binary stars over their lifetimes may experience different epochs during which mass transfer occurs or does not. Also, the same binary star may experience multiple types of mass transfer during its evolution. For example, a star may begin to drive a wind during one evolutionary phase, leading to wind-fed accretion onto its companion. This same star may evolve to a larger radius, filling its Roche lobe, leading to RLOF. The binary separation of the system will decrease over time as orbital angular momentum is carried away in a stellar wind, which may act to drive wind-fed systems toward RLOF. We may then see wind accretion and RLOF as the two extremes in a continuum of mass transfer states. We may ask ourselves, what is the transition like between these two extremes? How sharp is this transition, and are we able to identify any likely candidates to be in this regime? Later in this work, we define the Roche lobe overflow parameter λ , which is a measure of the “filling factor” of the donor star; *i.e.* how close it is to filling its Roche lobe, and examine the role it plays in determining whether a given system will be a “wind accretor,” a “disk accretor,” or something in between (see Chapter 3).

Another factor affecting the mode of mass transfer is orbital eccentricity; although circularization is usually a good assumption, exceptions are known. Within the X-ray binaries, one of the two stars will be a collapsed object that will have lost a significant fraction of its mass explosively. This process is expected to alter the eccentricity of the binary orbit, and circularization of an elliptical orbit will take some amount of time, during which we may observe an X-ray binary in non-circular orbit. The elliptical orbit X-ray binary GX 301-2 provides an excellent laboratory for investigating many of the typical assumptions about X-ray binaries, as well as unique phenomena, since the accreting neutron star periodically plunges deep into the companion star's stellar wind, very close to the companion. This essentially forces the system to undergo Roche lobe overflow once every binary orbit (see Chapter 3).

1.3 Accretion Disks

We may understand some important concepts about accretion disks merely from first principles. We know that the gas flow will involve dissipative processes such as shocks that will heat up the disk. Radiation will carry energy away from the disk in the form of a disk luminosity; in other words, the disk will shine. The ultimate source of the disk's luminosity must be liberated gravitational potential energy, *i.e.* some portion of the gas in the disk must move inward. But for this to occur, angular momentum must be lost in order for a gas parcel to drop to a lower orbit. Typically, angular momentum transfer involves internal torques within the disk and takes place much more slowly than energy loss via radiation. Hence the gas parcels rapidly lose as much energy as they can for a

given angular momentum, meaning that the gas orbits are likely near-circular (circular orbits have the lowest energy in the absence of the perturbation of the companion's gravity), with gas slowly spiraling inward as potential energy is liberated and angular momentum is transported outward. In order for angular momentum to be transported outward some fraction of the disk gas must carry it out. This implies that the outer disk spirals out while the inner disk spirals in.

Circular orbits imply that the gas flow is *Keplerian*: $v_{kep} = \sqrt{GM/r}$. In the case of an accretion disk, material that falls onto the surface of the accreting compact object impacts with grazing incidence with specific energy $-GM/R_\star + \frac{1}{2}v_{kep}^2 = -\frac{1}{2}GM/R_\star$. For a mass accretion rate \dot{M} , the disk luminosity is then half the total accretion luminosity:

$$L_{disk} = \frac{GM\dot{M}}{2R_\star} = \frac{1}{2}L_{acc}.$$

The other half of the accretion luminosity is either liberated at the accretor's surface, or may be lost in the case of a black hole accretor, which has no rigid surface for the accretion flow to impact.

Since the operation of our accretion disk as a machine for energy extraction depends on the transport of angular momentum, it behooves us to examine how such transport may take place.

1.3.1 Viscous Transport

The astute reader will notice where the hand-waving has occurred: in the transport of angular momentum. How exactly is angular momentum transferred through the disk? One way is via *viscous torques* within the disk. Consider the Keplerian orbital velocity

of the gas, which varies inversely with the square root of the radius. This means that gas orbiting at smaller radii is moving faster, and gas orbiting at larger radii is moving slower. Imagine that two successive annuli of the disk rotate as rigid hoops with the appropriate Keplerian orbital velocity. Now imagine that each hoop exerts some drag on the hoop next to it. You can see that the fast moving inner hoop will act to speed up the slow moving outer hoop, and vice versa. In other words, the drag between concentric annuli (viscosity) acts to transfer angular momentum from the inner annulus to the outer one. The inner annulus, now moving at sub-Keplerian velocity for its radius, will fall inward, accelerating until it reaches equilibrium. The outer annulus, now moving at super-Keplerian velocity for its radius, will move outward. Hence viscosity within the disk allows angular momentum to be transferred outward while mass moves inward, liberating gravitational potential energy.

Consider now two neighboring annuli of width δr sharing the surface of radius r , assuming the disk to be in equilibrium. We can see from the Keplerian flow that the inner annulus will be moving faster than the outer annulus, just as in our two-hoop model. The chaotic motions of the fluid ensure that fluid elements are continually exchanged across the surface at radius r with characteristic speed \bar{v} . Elements moving outward will carry an average angular momentum density of $\rho(r - \delta r/2)^2 \Omega(r - \delta r/2)$, while fluid elements moving inward will carry an average angular momentum density of $\rho(r + \delta r/2)^2 \Omega(r + \delta r/2)$, where $\Omega(r \pm \delta r/2)$ is the average angular velocity of the Keplerian flow within the two annuli. Because we have restricted the flow to be in equilibrium, the net mass flux across the surface r will be zero. The net angular momentum flux is

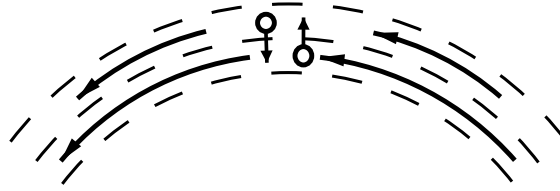


Figure 1.6: Two neighboring annuli in a Keplerian accretion disk exchange fluid elements in equilibrium. The net mass flux is zero, but the fluid elements from the inner annulus carry different angular momentum than do those from the outer annulus. Hence a net angular momentum flux exists, exerting a torque that acts to slow the inner annulus and speed up the outer one.

non-zero. Let the disk have a thickness H . The net angular momentum flux is then

$$2\pi r \rho \bar{v} H [(r - \delta r/2)^2 \Omega(r - \delta r/2) - (r + \delta r/2)^2 \Omega(r + \delta r/2)],$$

or perhaps more clearly, since $r \gg \delta r$:

$$-2\pi r^3 H \rho \bar{v} \delta r \frac{\Omega(r + \delta r/2) - \Omega(r - \delta r/2)}{\delta r}.$$

The fraction is just $\Omega' = d\Omega/dr$, while we may define $\rho H \equiv \Sigma$, the *surface density*, or the mass per unit surface area, of the disk. We will also define the standard coefficient of kinematic viscosity $\nu \equiv \bar{v} \delta r$ (also called the *shear viscosity*). Hence the net *torque* (the rate of change of the angular momentum) of the inner annulus on the outer annulus is

$$\tau(r) = 2\pi r^3 \nu \Sigma \Omega'.$$

Meanwhile, the work on an annulus of the disk between r and $r + dr$ by the net torque due to its neighboring annuli (interior and exterior) is

$$\Omega \frac{\partial \tau}{\partial r} dr = \frac{\partial}{\partial r} (\tau \Omega) dr - \tau \Omega' dr.$$

The $\frac{\partial}{\partial r} (\tau \Omega) dr$ term is a convection term; it represents the convection of rotational kinetic

energy through the disk via the torque; this energy can only have sources or sinks according to the boundary conditions at the inner and outer edges of the disk. But the second term, $-r\Omega'dr$, represents a local energy sink; the torques act to dissipate the gas' mechanical energy, which must go into internal energy, heating the disk. This loss of mechanical energy, which can only come from the gas' rotational energy, is what drops the gas to a lower orbit, liberating gravitational potential energy in order to speed the gas back up to Keplerian velocity.

We see then that the efficiency of the disk in communicating angular momentum, and hence its efficiency as a machine for extracting gravitational potential energy, is dependent upon the viscosity ν . What then can we say about the magnitude of ν ? Unfortunately, we can say a lot.

Let us consider the Reynolds number of the flow, which is a measure of the relative importance of the inertia of the fluid flow to the viscosity:

$$Re = \frac{rv_\phi}{\bar{v}\delta r}.$$

If $Re \ll 1$, viscous forces dominate the flow (as in motor oil). If $Re \gg 1$, viscosity is unimportant. Using typical values for the size and speed of flow expected within accretion disks, and taking δr and \bar{v} to be the mean free path between collisions and the sound speed of the gas, respectively, we find that the molecular Reynolds number exceeds 10^{14} , making the normal kinematic viscosity completely negligible. Molecular viscosity cannot extract the energy we require.

However, the large magnitude of Re_{mol} seems to imply that it is likely that accretion disk flow is *turbulent*, since most laboratory fluids become turbulent by $Re = 1000$.

Turbulent flow is characterized by large scale chaotic motions. \bar{v} and δr now become the turnover velocity and size of the largest turbulent eddies within the flow. Unfortunately our ignorance of turbulent fluid flow is profound. We cannot state *a priori* at what point the hypothetical turbulence would saturate, since this would depend on unknown physical mechanisms within the disk. We can provide an upper limit for both δr and \bar{v} at best. We know that the size of the largest turbulent eddies cannot exceed the thickness of the disk, so $\delta r \leq H$, and we know that the turbulent velocities are likely not supersonic, since if they were the turbulent motions would be dissipated away by shocks, so $\bar{v} \leq c_s$, where c_s is the sound speed.

Hence we parameterize all of our ignorance in the infamous α -*prescription* of Shakura and Sunyaev [1973]

$$\nu \equiv \alpha c_s H,$$

where we expect on the previously stated physical grounds that $\alpha < 1$.

Unfortunately for us, recent work by Balbus and Hawley [1998] shows that the radial gradients in the Keplerian flow act to stabilize it; indeed the disk is *not* hydrodynamically turbulent. However, we note that molecular interactions or hydrodynamic turbulence need not be the only physical mechanisms that can create viscosity within the disk. Any mechanism that can couple the shearing flows within the disk, and hence transport angular momentum, will act like a viscosity. One promising mechanism is the so-called *magneto-rotational instability*, or MRI, of Balbus and Hawley [1998]. Consider two magnetized fluid elements rotating in neighboring annuli. If the disk is in Keplerian rotation (for example) the inner element will begin to pull away from the outer element.

But the tension in the magnetic field between the two elements acts as a spring, coupling the two elements, that is being stretched. The inner element will be slowed, and the outer element will be accelerated, *i.e.* angular momentum is transferred from the inner element to the outer element. The inner element falls in while the outer element moves out, exactly as in our previous example. Thus the MRI provides a magnetohydrodynamic viscosity to the disk.

1.3.2 Non-Viscous Transport by Global Waves Modes

All of the angular momentum transport mechanisms we have discussed so far have been *local* effects; in other words effects that are dependent only on local quantities within an infinitesimal portion of the disk and behave like a fluid viscosity. However, angular momentum can be transported by completely non-viscous effects such as global wave modes (Goldreich and Tremaine [1980]; Lynden-Bell and Kalnajs [1972]; Papaloizou and Pringle [1977]), such as spiral shocks, which can act as an angular momentum sink (Larson [1989]; Sawada et al. [1986b]; Shu [1976]; Spruit [1987]). Consider a shock within the disk at some obliquity to the fluid flow. As the flow crosses the shock, some portion of its mechanical energy is dissipated, heating up the disk. Hence a gas parcel crossing this shock loses rotational kinetic energy, and will fall toward the accretor, liberating gravitational potential energy. This argument depends, of course, on whether or not the angular momentum carried by the fluid element can be carried away.

Up to this point we have assumed the flow of our accretion disk to be Keplerian. Implicit in this assumption is the neglect of the presence of the binary companion that,

from the disk's point of view, orbits it. Just as the gravity of the moon orbiting the earth distorts the fluid covering the earth (the oceans) causing high and low tides, the orbiting presence of a massive companion causes tides within an accretion disk. Consider again the disk in a frame rotating with the binary. The gravity of the companion, as well as the centrifugal and Coriolis forces due to the rotating frame, will vary with azimuth around the disk. This implies that the equilibrium orbits of the disk are no longer Keplerian. Paczynski [1977] identifies a family of closed pseudo-elliptical orbits that are solutions to the restricted three-body problem (in absence of pressure forces) in the region of the accretor. Differential accelerations around the disk due to the tidal forces will cause some regions of the flow to move faster than others; the flow will develop over-dense regions where the flow is slower, as well as rarefied regions where the flow is faster. These disturbances are sheared out by the Keplerian flow into spirals, and pressure gradients in the flow will steepen them into shock waves as they propagate inward. These are the famous two-armed trailing spiral shock waves of accretion disks in binary systems. Let us examine them in detail.

The equilibrium position of the spiral shock is determined by a balance between the ram pressure ahead of the shock and the gas pressure behind it. Since the ram pressure ahead of the shock is proportional to the speed of the flow perpendicular to the shock squared, and the speed of the flow increases with decreasing radius, we see that the obliquity of the shocks must increase to keep the ram pressure of order the gas pressure. Hence, the spirals become more tightly wound at smaller radii:

$$\rho v_\phi^2 \sin^2 \theta \propto c_s^2 \rho,$$

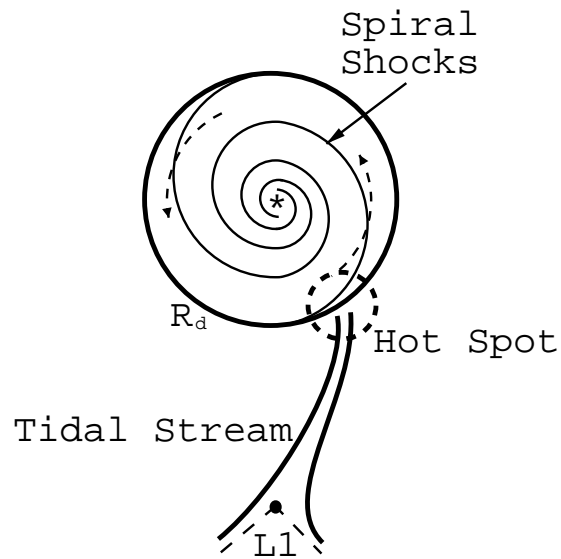


Figure 1.7: The accretion disk's outer radius r_D is greater than the circularization radius, due to the outward flux of mass and angular momentum. The outer radius lies at the *tidal truncation radius*, where the tides are so strong that the outer disk is torn apart. The flow within the disk strikes the spiral shocks at an angle determined by a balance of ram pressure ahead of the shock and the thermal pressure behind it; at smaller radii the Keplerian velocity increases, requiring the spirals to wrap more tightly to maintain this balance.

or

$$\sin \theta \propto \frac{1}{\mathcal{M}},$$

where θ is the shock angle (the angle between the pre-shock flow and the shock) and \mathcal{M} is the Mach number of the flow, v/c_s . Since the shock can only dissipate kinetic energy from the component of the velocity perpendicular to the shock, this implies that the spiral shocks become less and less efficient at dissipating energy at small radii, since this component becomes ever smaller. Eventually, the shock is wound so tightly that the flow is all but parallel to the shock, and the shock essentially ceases to exist. In other words, dissipation by the spiral shocks turns off at smaller radii. If the Mach number of the disk is large enough everywhere, dissipation by spiral shocks will be negligible throughout the disk.

The spiral shocks are two armed because the disturbance that creates them, the tidal forces, is an $m = 2$ mode (to first order). Shu [1976] postulate that the impact of the tidal stream could drive a one armed spiral into the disk, since there is only a single propagating disturbance (the impact) to be sheared out by the flow; this $m = 1$ mode should drive accretion in the same manner as the tidally driven $m = 2$ spiral modes. Hence it is possibly that the actual disk structure may have both one and two armed spiral modes propagating through it.

1.3.3 Tilted Disks, Precession, & Radiation Torque

There is considerable observational evidence that some systems contain tilted, precessing accretion disks, so it would be wise to develop an understanding of the dynamics of a

tilted disk, and how it might get that way.

Consider an accretion disk that orbits in a plane other than that of the binary orbit. The orbits of this disk experience non-symmetric tidal forces around the disk; thus each annulus of the disk will experience a *tidal torque* (this is true whether the disk is tilted or not). Consider a top that is spinning about an axis off the vertical. The gravitational force causes the top to experience a torque that is perpendicular to the angular momentum vector; the magnitude of the angular momentum stays the same, but the direction changes; *i.e.* the axis of rotation of the top precesses. Similarly, tidal torques will cause the direction of a tilted disk in a close binary to precess. Because the accretion disk is a fluid, communication of the tidal torques makes the precession rate relatively independent of radius (in other words the disk precesses more or less coherently, as though it were a rigid body), while the net torque depends on the outer radius of the disk, where the tidal forces (and hence the torques) are strongest. Larwood shows that the ratio of the orbital period to the precession period is

$$\frac{P_{\text{orb}}}{P_{\text{prec}}} = \frac{3}{7} \left(\frac{q^2}{1+q} \right)^{1/2} \left(\frac{R_d}{a} \right)^{3/2} \cos i. \quad (1.2)$$

where R_d is the radius of the accretion disk, and i is the inclination of the disk relative to the binary orbital plane ($i = 0$ is in the binary orbital plane) [Larwood, 1998a].

Katz [1973] proposed periodic obscuration by a precessing tilted accretion disk to explain recently-discovered super-orbital periodicities observed in the light curves of the X-ray binary Her X-1. Roberts [1974] proposed a “slaved disk model” in which the donor star rotates with an angular momentum vector misaligned with the binary orbital angular momentum vector, hence material transferred through the L1 point would also have a

misaligned angular momentum vector. However, the net angular momentum transferred over an orbital period is still aligned with the binary orbital angular momentum, since half the time the accretor is above the donor's equator, and half below; the residence time of the disk gas would have to be extremely brief. Also, the axial tilt of the donor would decay due to tidal friction on a timescale shorter than the orbital circularization timescale, and Her X-1 is believed to be circular or near-circular.

The likely candidate is thought to be *radiation driven warping*. Motivated by Petterson (Petterson [1977a]; Petterson [1977c]; Petterson [1977b]) and Iping and Petterson [1990], Pringle [1996] showed that a centrally illuminated disk is unstable to warping by re-radiation back-pressure. To understand how radiation driven warping works, we need to understand how the disk is illuminated by the central source.

Consider an accretion disk that is everywhere in local hydrostatic equilibrium. For a given fluid element at some small distance z (the disk is thin) above the binary orbital plane, the cylindrical-radial component of the accretor's gravity is balanced by the centrifugal force (we shall neglect the companion for the moment):

$$\frac{GM}{R^2} \frac{r}{R} = \frac{v_\phi^2}{r},$$

where R is the distance to the accretor and r is the cylindrical radius. Since the disk is thin, we arrive at the familiar Keplerian velocity profile:

$$v_\phi(r) \approx \sqrt{\frac{GM}{r}}.$$

The disk is supported vertically against collapse due to the accretor's gravity by hydrostatic equilibrium:

$$f_z = -\frac{GM}{R^2} \rho \frac{z}{R} - \frac{dP}{dz} = 0.$$

For convenience, consider an isothermal equation of state $P = c_s^2 \rho$. Rearranging we find:

$$\frac{d\rho}{\rho} = -\frac{GM}{c_s^2 R^3} z dz,$$

or

$$\rho(z) = \rho_0 e^{-z^2/H^2},$$

where H is the *scale height* of the disk, *i.e.* its thickness, and is defined by

$$H^2(R) \equiv \frac{2c_s^2}{GM} R^3.$$

We see that the thickness of the disk increases with increasing radius as the 3/2 power, thus the disk is *concave*.

Because of this concavity the disk surface will intercept some amount of flux from the central source. In the case of an accreting neutron star or black hole in an X-ray binary, that flux will be mainly hard X-rays. Since the X-rays are traveling radially, direct radiation pressure can exert no torque on an orbiting fluid annulus that absorbs them. However, they can and do heat up the disk surface, causing *re-radiation* of the reprocessed X-ray flux. Since this re-radiation is preferentially normal to the disk surface, it *can* exert a torque on the surface. Since the disk has two surfaces, one might expect that the net torque would remain zero, but Pringle has shown that even an initially flat disk is unstable to radiation torques if the central source is sufficiently luminous [Pringle, 1996].

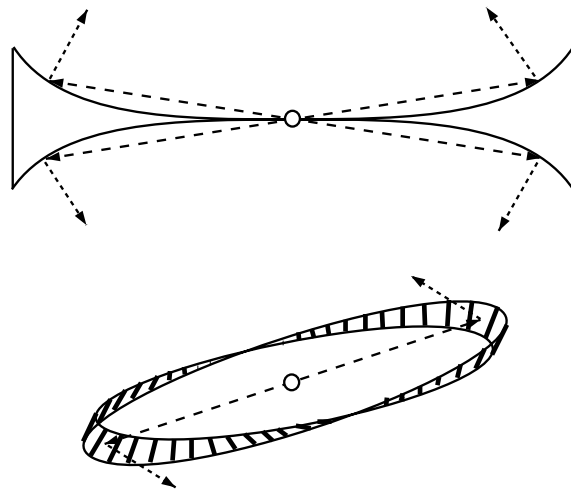


Figure 1.8: The concavity of the accretion disk’s surface implies that it will be strongly illuminated by the central X-ray source. While the direct X-ray flux can exert no torque, the force due to thermal re-radiation of absorbed X-rays is normal to the surface, and can exert a net torque. The disk is unstable to warping via this mechanism if the central luminosity is high; once the symmetry is broken and opposite surfaces become shadowed on opposite limbs of any annuli, torques can easily warp the disk.

Such radiation torques can drive the disk out of the plane, tilting and twisting it, creating a warped disk. Once out of the plane, radiation and tidal torques will induce precession of the disk, yielding super-orbital periodicities via cyclic changes in the orientation of the system over time. Even though the primary must orbit the tilted disk once every binary orbit, the particular orientation of disk and companion as a function of phase now changes for us, the observers. At one point, the disk may be facing us, providing an unobstructed view of the hard X-ray source (excepting eclipses by the companion), in other words a “high” state, while at some time later, precession of the disk may obscure the hard X-ray source completely behind the edge of the disk, leaving only coronal emission or perhaps cold X-ray reflection from the companion, *i.e.* a “low” state.

1.4 Observing Accretion onto Compact Objects in Close Binaries

We have built up a rather extensive catalog of physical possibilities for accreting systems in binary stars. Let us now examine the observational evidence for them. Indeed we do see a plethora of galactic and near-galactic point X-ray sources which can be attributed to accretion onto a compact object in a binary star. Generally, these fall into three classes: the high mass X-ray binaries (HMXBs), the low mass X-ray binaries (LMXBs), and the so-called cataclysmic variables. The first two collectively make up the XRBs. In this section we will examine both the observational classes, and the various observational techniques used to investigate them.

1.4.1 Nomenclature

Let me first digress and discuss X-ray source naming conventions. Historically, point X-ray sources are identified by the constellation they occupy and an X designation signifying their brightness relative to other X-ray sources in that constellation; Her X-1 is the brightest X-ray source in the constellation Hercules. Near-galactic sources in the Small and Large Magellanic Clouds receive SMC and LMC designations; hence LMC X-4 is the fourth brightest X-ray source in the Large Magellanic Cloud. Fainter sources from newer catalogs may have other designations, such as GX 301-2.

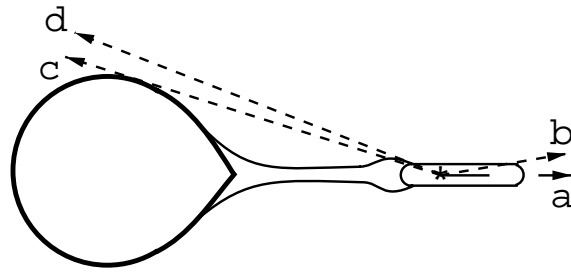


Figure 1.9: At high inclination (a), the hard X-ray source is obscured by the disk and only scattered or reflected X-rays, or X-rays emitted from a hot diffuse corona above and below the disk, can be seen. At slightly lower elevations (b) the hard X-ray source can be seen, with the flux modulated by the outer edge of the disk. Eclipsing will be observed up to point (c), the position of which depends on the mass ratio of the system (and hence the relative sizes of the disk and donor). Specific features of the system structure such as attenuation of X-ray flux by a splashing impacting tidal stream may be observed up to moderate inclinations (d) beyond which only the hard X-ray source can be seen.

1.4.2 Geometric Considerations

We may predict some observational properties of accreting binary systems simply due to the geometry of our problem, as in Figure 1.9. The binary will orbit in a plane that makes some angle, called the inclination, with our line of sight. If we are observing in the plane of the orbit, we should observe the disk and its donor periodically eclipse each other as they rotate. If we are looking straight down toward the orbital plane, we should observe no eclipsing. Since both the donor and the disk have physical extent, we expect that the shape of observed light curves will vary according to the inclination of the system; for example, for certain inclinations the disk or donor may partially, rather than fully, eclipse its companion.

1.4.3 Observational Techniques

We do not have the luxury of studying accreting binaries from close up; rather we must rely solely on the photons that wend their way to our various instruments. Furthermore, these systems are much too far away to be directly imaged. Therefore astronomers have developed clever ways to massage the photons into divulging information about these systems. Our entire understanding of accreting binaries comes from the interpretation of time dependent continuum and line emission via various observational techniques.

Light Curves and Total Flux

We are interested in the time-dependent flux from the system, or the *light curve*. Typically, observations of binary stars are made as a function of *orbital phase*, which is essentially time, normalized to the binary period. Hence phases 0 and 1 correspond to mid-eclipse (although some authors use the opposite convention) of the accretor (this definition is clearly problematic if no eclipse exists). The timescale of the variability tells us the physical scale of the source of the variability. Very rapid fluctuations in hard X-ray luminosity likely arise near the accretor. Longer term, but still short, fluctuations in soft X-ray or UV may correspond to the dynamics of the disk. Changes on the orbital timescale such as eclipses give us information about the global structure of the binary. Very long timescale variations (longer than the orbital period) may tell us about the global evolution of the system, as we shall see later. If a distance to the object can be determined, total flux measurements allow us to ascertain the system's absolute luminosity.

Spectra

The detailed spectra of a system can provide a wealth of information; we may expect to identify red-shifted and blue-shifted emission due to both the binary rotation and the rotation of the accretion disk, should one exist. We expect that different regions of the system will have different temperatures, optical depths, ionization states, etc. and will be emitting different spectra. Soft X-rays can provide column densities within a system, while UV line profiles can provide stellar wind parameters. We expect different systems (for example accreting neutron stars *vs.* black holes) to be emitting primarily in different bands from UV to soft X-ray, hard X-ray, and γ -ray.

Line Profiles

Cataclysmic variable (see below) accretion disks have strong emission lines of hydrogen and helium. An individual line will be convolved into a complex curve by the dynamics of the system. Consider a single line that is emitted uniformly by a disk with some inclination to our line of sight. The rotation of the gas of this disk will cause some of the emission to be red-shifted (when gas is moving away from us) and some to be blue-shifted (when gas is moving toward us). Furthermore, because of the differential rotation of the gas, the fast moving gas near the center of the disk will be shifted more than will the slower moving gas in the outer disk. Now add in the fact that the entire disk is in orbit around another star, adding a background shift that moves from blue to red over the course of an orbital period. Finally, consider that it is unlikely that the disk actually *is* emitting uniformly; there is no reason *a priori* to assume that the disk is all the same temperature, for example. We may expect emission preferentially from

regions where dissipation occurs, such as shocks, for example from a tidal stream impact or spiral shocks. But we can say that generally a line from an accretion disk is expected to be “two horned” with a red-shifted and a blue-shifted peak. Over the course of a binary orbit, the background frequency shift due to the orbital motion will alternately make one peak stronger than the other.

Eclipse Mapping

If we are lucky enough to observe the system at a high enough inclination, we may observe eclipses of the disk emission by the primary. In this case, as the system enters eclipse, the blue-shifted peak is lost, as the disk gas moving toward us is obscured. As the system nears the end of eclipse, the red-shifted peak is temporarily lost, as the gas moving away from us is occulted. This leads directly to a technique known as *eclipse mapping*. This method is used to attempt to map out the continuum emission of the disk surface. The continuum emission of the disk will be a complex function of the detailed local physics of the disk, including dissipation, dynamics, radiative transfer within the disk, etc. For example, at high energies (shorter wavelength) the emission is expected to be sharply peaked near the accretor, while at lower energies (longer wavelengths) the emission is more uniform. There may be localized emission at some wavelengths due to a “hot spot” (stream impact). As the companion orbits it will eclipse different regions of the disk surface at different orbital phases. This allows us to infer the net emission from the region in shadow by what has been *subtracted* from the signal. These time dependent spectra may then be deconvolved to provide emission maps of the disk surface.

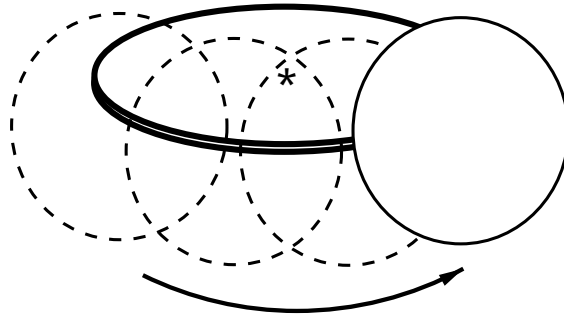


Figure 1.10: If the inclination is high enough for the donor to occult the disk, then we may use time dependent light curves and spectra to deconvolve the emission structure of the disk.

Trailed Spectrograms & Doppler Tomograms

Returning to line emission, we may make use of the fact that the line profiles change as a function of binary phase (and are typically different for different lines, since as we have discussed, emission is not expected to be uniform over the surface of the disk). Essentially, every parcel of gas in the disk will have some component of velocity along our line of sight, producing a frequency shift. The integral over the disk surface produces the double-peaked line profile we have already discussed. As the binary orbits, we are essentially viewing the disk from all azimuthal angles. Stacking of line profiles over time allows us to create a *trailed spectrogram* that shows the changes in the frequency shifted line as the binary orbits. Using the same idea of deconvolving our data given certain assumptions about the disk (namely inclination and the assumption that the disk is Keplerian or nearly so) we may produce velocity-space maps of the disk, known as *Doppler tomograms*.

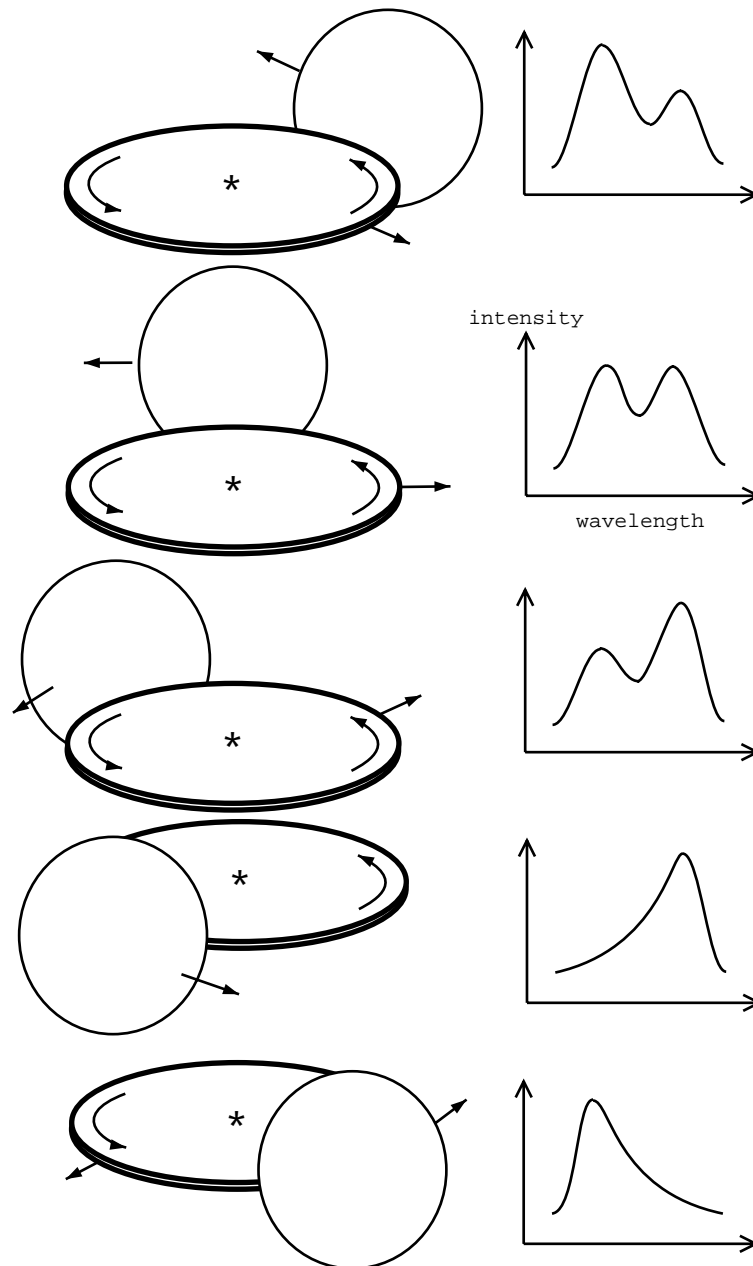


Figure 1.11: A single emission line within the disk will be smeared out into a line profile by a combination of factors including Doppler shifting due to the Keplerian rotation of the disk, Doppler shift due to orbital motion, and (perhaps) differential occultation of the disk. The signature of Keplerian flow is the “two horned” line profile. Orbital motion can shift the horns to either side, while occultation of one limb of the disk can cause the horns to alternately vanish.

1.4.4 Kinds of Accreting Close Binaries with Compact Objects

We now turn our attention to the three kinds of accreting close binaries that contain compact accretors: the X-ray binaries, including the high-mass and low-mass XRBs (HMXBs and LMXBs, respectively), and the so-called cataclysmic variables.

High Mass X-Ray Binaries

The HMXBs are composed of giant or super-giant stars accreting onto either neutron stars (LMC X-4) or black holes (Cyg X-1), either via wind accretion (Vela X-1), or disk accretion (Her X-1). Typically these systems have mass ratios $q > 1$, usually significantly greater than 1; for example the HMXB LMC X-4 has a donor to accretor mass ratio of 10.6. Generally these systems have extremely high hard X-ray luminosities ($10^{35} - 10^{38}$ erg s⁻¹) that are expected to be generated very close to the accretor's surface. Typically, ultraviolet flux from the disk is totally swamped by the luminosity of the companion giant, which is also of order 10^{38} erg s⁻¹ and is peaked in the UV. However we know that the *only* process capable of generating such X-ray luminosities is accretion onto a compact object, and it is reassuring that we can often identify an optical counterpart, the donor star (for example, the donor star to Her X-1 is HZ Her). Since the size of the donor star is large compared to the binary separation in these systems, they typically exhibit eclipses of the X-ray source. Because the companion star is generally luminous enough to be detected, we can often observe details of its stellar envelope, such as the presence of a stellar wind by shifted absorption and emission lines in the UV, for example P Cygni lines.

We may differentiate the wind accretors from the disk accretors in two ways. One, the disk fed HMXBs are typically more luminous than the wind fed HMXBs, and two, the rate of change of spin of the neutron star is typically higher in disk fed systems. If the emission from the surface of the neutron star is not axisymmetric about the axis of rotation, for example if matter is channeled along magnetic field lines to an off-axis “cap” where the X-rays are then preferentially emitted, then we will observe pulses in the neutron star’s emission as it rotates, *i.e.* an X-ray pulsar. Since material accreting from a disk is expected to carry some net angular momentum, we expect the neutron star to “spin up” over time. In a wind fed system gas from the companion’s stellar wind is focused head on and is expected to carry little net angular momentum; hence we expect little coherent long term change in the spin of a wind fed pulsar (although it may be possible to form transient accretion disks behind the bow shock of a wind fed accretor).

Low Mass X-Ray Binaries

The LMXBs are composed of an accreting neutron star in close binary orbit with a low mass main sequence companion, typically less than $1 M_{\odot}$. Typically the donor star is at most about the same size as the accretion disk, and may be significantly smaller; eclipses of the hard X-ray source are rare in these systems, since they have to be viewed almost edge-on to produce them. Typically emission from the accretor, the disk, and the companion all lie in different bands: X-ray, UV, and optical, respectively. However, the companion stars are typically so faint that they are rarely detected, and the disk emission is dominated by X-ray emission reprocessed by the disk, rather than intrinsic

emission from the disk itself.

In both classes of XRB our observational options are limited. With the exception of the spectrum of the companion stars in the HMXBs, we are typically restricted to measurement of the hard X-ray flux from the accretor, the reprocessed X-ray flux from the illuminated surface of the disk or companion, or X-rays emitted from a hot corona above the surface of the disk (an extended, rather than point X-ray source). These are still very useful tools, however; it is as if we are able to take an X-ray of the circumstellar gas of our binary star. Unfortunately, we are restricted to a single inclination angle for any one system. This gives rise to a number of distinct observational clades that depend upon inclination, as mentioned above (see Figure 1.9).

Cataclysmic Variables

This is actually a catch-all class that includes novae, dwarf novae, nova-like variable stars, intermediate polars, etc. We will not be discussing the manifold differences of these systems, but let us examine what they have in common. All of these system have a normal “quiescent” luminosity that is believed to be driven by accretion from a low mass main sequence binary companion onto a white dwarf, punctuated by periods of higher luminosity (outbursts) that are generally attributed to sudden changes in mass accretion rate.

Our observational options are much greater with the CVs than with the XRBs. Because of the lower compactness M/R of the accreting star, these systems are much less luminous than the XRBs, and their emission is not dominated by the central accretor; the emitted spectrum of the disk can also be measured. This makes the full breadth of

observational techniques available to us, including eclipse mapping, trailed spectrograms, and Doppler tomograms. Hence CVs are a valuable resource in investigating accretion disks in close binaries; cataclysmic variables have similar mass ratios to the LMXBs, and many observational qualities of CVs may be applicable to the XRBs. However, we cannot ignore the fact that CV sources are much less luminous, and there is no reason *a priori* to expect CV and XRB disks to have similar temperatures, ionization states, etc.

1.4.5 Observations

Let us turn now to actual observations that confirm the presence of some of the most important features that we expect to be present if our picture of accretion onto compact object in close binaries is accurate.

Wind Accretion and Roche Lobe Overflow

For a compact object to be accreting a companion's wind, we expect that companion to be of a proper spectral type to drive a strong wind, for example an OB giant or super-giant. Such stars are rare and hence generally very distant. Therefore we expect that if an accreting companion is to be detected, it must be bright; a neutron star or black hole, rather than a white dwarf. If the object is a spinning, magnetized neutron star, we may expect it to be an X-ray pulsar. From these objects we expect moderate X-ray luminosities, moderate pulsar pulse periods, and a lack of steady spin-up of the pulsar. A handful of objects fit this description, generally they are the high mass X-ray binaries, of which only a few are known, such as Vela X-1 and 4U 1700-37. Generally in these systems, the companion star is very luminous, and an optical counterpart can

be identified for the X-ray source. UV and optical spectroscopy allows us to confirm the presence of the donor's stellar wind and characteristics about it. Dupree et al. [1980] confirm the optical counterpart to Vela X-1 to be an early B-type super-giant driving a strong wind, and that the wind shows strong variability over the binary orbital period, due to the changing photoionization state of the circumstellar gas. Sako et al. [1999] and Schulz et al. [2002] show that the X-ray spectrum of Vela X-1 is consistent with the X-ray source being embedded in a hot, diffuse photoionized wind laced by cool, dense, optically thick clumps. Kaper et al. [1994] suggest the presence of a photoionization wake trailing in the donor wind to explain absorption at late phase and low velocity in Vela X-1. Vela X-1 is an X-ray pulsar with a relatively long pulse period of nearly five minutes, and a lack of consistent pulse period decrease.

Non-Circular Orbits

A class of hard X-ray transients exists where the X-ray source is observed to have an optical counterpart of a spectral type that drives a strong wind. These transients exhibit periodic X-ray flares. Some of these systems are believed to be accreting eccentric orbit X-ray binaries (some may be due to periodic changes in the donor star, though). Since the density of a diverging stellar wind drops as r^2 , it is reasonable to infer that a neutron star in eccentric orbit embedded in the donor's wind will experience periodic changes in mass accretion rate and X-ray luminosity. Parmar et al. [1989] list six Be X-ray binaries for which the X-ray flaring interval is consistent with the orbital period of the system. At least three systems exhibit X-ray flares occurring close to periastron passage: V 0332+53 [Stella et al., 1985], A 0538-66 [Mavromatakis and Haberl, 1993],

and GX 301-2 (Watson et al. [1982]; White and Swank [1984]; Sato et al. [1986]).

Accretion Disks

Accretion disks in close binaries can generally be found in the highest X-ray luminosity XRBs, where if they are accreting pulsars, they will generally tend to have short pulse periods and consistent pulsar spin-up rates (although if the neutron star is in spin equilibrium with the inner edge of the accretion disk, the latter condition may not hold). These systems will also generally have short binary orbital periods, since the accreting neutron star must orbit the donor quite closely for RLOF to take place. Such systems can be found among the the well studied HMXBs including LMC-X4 (Kelley et al. [1983]; Woo et al. [1996]), Cen X-3 [Tsunemi et al., 1996] and SMC X-1 [Kahabka and Li, 1999], and among the LMXBs, which are far more numerous; Liu et al. [2001] catalogs nearly 370 low mass XRBs.

Accretion disks are also likely the culprits in systems that show infrequent outburst activity, such as novae. These are of course the cataclysmic variables. Optical and UV spectra can be used to identify the presence of an accretion disk. Observations of accretion disks in CV systems are almost a dime a dozen (Ritter and Kolb [2003] lists 472 CVs). For example, Hoard et al. [2002] observe nova-like CVs with the Far Ultraviolet Spectroscopic Explorer, and demonstrate prominent disk signatures in the spectra of three (DW UMa, LS Peg, MV Lyr).

The Tidal Stream & Hot Spot

A feature that is of particular interest is the tidal stream. Richards et al. [1995] showed

the presence of a tidal stream using hydrogen α ($H\alpha$) line profiles from four Algol-type binaries (Algol binaries are mass transferring binaries in which the mass gaining star is not a compact object, but rather a normal main sequence star; hence some Algols will exhibit accretion disks if the accretor is small enough, but experience direct impact of the stream otherwise). Difference profiles were constructed by subtracting out the emission due to the stellar photospheres, leaving only the contribution due to circumstellar gas. Doppler tomograms were then constructed from the phase-dependent difference profiles clearly showing the presence of emitting material at velocity coordinates corresponding to those of a tidal stream in ballistic free fall.

Shahbaz et al. [2003] identify a late phase (~ 0.8) optical photometric dip with a disk bulge due to tidal stream impact in the high inclination soft X-ray transient XTE J2123-058. Baptista et al. [1998] use eclipse mapping techniques to produce spatially resolved spectra of the accretion disk and gas stream of UX UMa, and find that the gas stream overflows the surface of the disk rim down to a radius of $0.1 R_{L1}$.

Spiral Shocks

Observational evidence of spiral structure in close binary disks was woefully lacking for many years (almost to the point of embarrassment). However, beginning with IP Peg, an eclipsing dwarf nova CV, Doppler tomographic maps of hydrogen Balmer and helium emission lines during outburst have demonstrated the existence of two-armed spirals within the disk [Steeghs et al., 1997]. Recently eclipse mapping has also been used to image IP Peg's spiral shocks, showing that the gas flow in the shocks is sub-Keplerian, and that the two spiral arms account for a significant fraction of the emitted line flux, as

much as 30% [Baptista et al., 2000]. Finally, recent Doppler tomograms of the quiescent state of IP Peg also clearly indicated the presence of spiral shocks, along with more complicated structure. The emission lines demonstrate quasi-periodic oscillations of a period much shorter than the orbital period, but modulated by the orbital period. This likely arises from hot spot emission that varies with the time-dependent dynamics of the disk (hence the quasi-periodic oscillations) and periodic obscuration by the disk edge at particular orbital phase [Neustroev et al., 2002].

The flood gates have begun to open on detection of spiral structure in close binary accretion disks; Morales-Rueda and Marsh use spectra of 48 CV systems during outburst to identify 12 candidates (other than IP Peg) for the detection of spiral structure, of which SS Cyg, EX Dra, and U Gem have been shown to exhibit spiral shock signatures [Morales-Rueda and Marsh, 2002].

Although accretion disks in close binaries are too distant to be imaged directly, the physics involved scales directly to much larger systems. Clampin et al. [2003] used the Hubble Space Telescope Advanced Camera for Surveys to study the circumstellar disk around HD 141569A, and have directly imaged spiral structure due to a binary companion.

Tilted, Precessing Disks

By the early 1970s, Her X-1 was known to exhibit very long timescale periodic modulations of X-ray intensity (see for example Ulmer et al. [1972]), much longer than the orbital period (the period of the super-orbital modulations is 35 days compared to a 1.7 day orbital period). Her X-1 exhibits a main high flux state followed by a low state, a

shorter high state, and a final low state. Clearly these long term modulations represent some repeating dynamic process within the system, conjectured to be a tilted, precessing accretion disk [Katz, 1973]. Larwood [1998b] shows that tidal precession of a thin, tilted accretion disk adequately explains the super-orbital periodicities of not only Her X-1 but also SS 433 (164 days; Margon et al. [1979]), LMC X-4 (30.5 days; Lang et al. [1981]), and SMC X-1 (55 days; Gruber and Rothschild [1984]).

Quasi-periodic oscillations have also been identified in the time dependent X-ray flux of Her X-1 [O’Brien et al., 2001]. The frequency range of these QPOs corresponds to orbital frequencies in the disk interior, and may represent the stream striking the surface of the disk near its center rather than at the edge. This is easily understood in the context of the stream striking a disk tilted out of the binary orbital plane.

1.5 This Work

Our goal in this work is to use numerical hydrodynamics, also known as computational fluid dynamics (CFD), to better understand mass transfer and accretion in close binary stars with compact accretors such as neutron stars and black holes (although the results within Chapter 3 may be applicable to CV white dwarf accretors as well). We employ a numerical hydrodynamics code to simulate the gas flow within these types of systems under various physical approximations. In general, these simulations resolve the spatial domain of interest into some millions of zones, each carrying a local zone-average value of the bulk fluid quantities, density, pressure, and velocity, from which other quantities (temperature, angular momentum, etc.) may be derived. We evolve these quantities

under the equations of fluid dynamics, given source terms such as gravity and X-ray heating according to the physics of the model in question, using high performance computing resources such as the Cray Y-MP, T916, T3d & T3e, and the IBM SP2 & SP3, at facilities such as the North Carolina Super Computing Center (NCSC) and the NASA Goddard Space Flight Center (GSFC).

We describe our numerical methods in Chapter 2, including the hydrodynamics code, and areas of specific interest to our topic, including application to spherical coordinates and rotating frames of reference. We present two projects in chapters 3 & 4 that investigate two main areas within our subject of interest. Detailed numerical considerations pertaining to the physics of each individual project may be found with that project.

In chapter 3 we present studies of mass transfer in the HMXBs. Phenomenological models describing individual systems are often fits to observational data, without regard to any detailed calculation of the physics involved, such as the hydrodynamic response of a disk. One of the aims of this work is to validate phenomenological descriptions, created specifically to match observations, with the hydrodynamics of close binary stars. In Chapter 3 we undertake an analysis of mass transfer as a function of wind accretion versus Roche lobe overflow, simulations of tidal mass transfer in elliptical orbit X-ray binaries such as GX 301-2, and a detailed global simulation of the HMXB LMC X-4. These simulations all include detailed physical approximations such as the UV line-driven donor wind, X-ray heating, photoionization, and radiation pressure, as well as radiative cooling of the gas.

In chapter 4 we present high resolution 3D simulations of accretion disks in a tidal

potential. Much analytic and computational work has gone into the study of spiral shocks in accretion disks. Typically, however, the simplifying assumption is made that the accretion disk is not only thin, but so thin as to be effectively two dimensional; *i.e.* the vertical structure of accretion disks is ignored. 2D simulations of accretion disks in close binary stars show crisp, steady spiral shocks, capable of large accretion rates in the outer portion of the disk, that drop rapidly at small radii [Blondin, 2000]. What effect does the relaxation of the restriction to 2D have on the structure and dynamics of spiral shocks and transport within the disk? What, if any, are the observable effects of fully 3D disks? Previous 3D simulations of accretion disks in close binaries have suffered from poor resolution or highly dissipative techniques, such as smooth particle hydrodynamics (SPH), that cannot adequately resolve spiral shocks (Makita et al. [2001]; Belvedere and Lanzafame [2002]).

Our understanding of super-orbital periodicities in terms of tilted, precessing disks relies on models that attempt to fit the light curves of particular systems, and is often more phenomenological than physical. For example, Leahy tests models including reflection of soft X-rays from the companion, shadowing of the companion by the disk, and extended emission from the disk surface to model the extreme ultraviolet emission from Her X-1 during its low state [Leahy, 2003]. He tests four distinct system geometries of varying disk tilt, warp, and thickness, and finds the one that best fits the observational data. However, these geometric models are not based on the hydrodynamic response of the disk. Can we reproduce such phenomenological constructs using the hydrodynamics of a tilted, fluid disk in a tidal potential? We examine tilted fluid disks at the end of

Chapter 4.

Chapter 2

Computational Fluid Dynamics

2.1 The Equations of Fluid Dynamics

Many, if not most, of the observed properties of mass transfer and accretion are determined by the dynamics of the circumstellar and accreting gas within the system. The detailed shape and velocity of the tidal stream, the diameter and thickness of a disk, the existence of a tidal stream impact “hot spot”, the radial temperature and density profile of the disk, the structure of the spiral waves, all produce the particular light curves, eclipse maps, trailed spectrograms, and Doppler tomograms that we use to try to build a picture of these systems. Understanding the fluid dynamics within these systems is of paramount importance to the interpretation of observations. Perturbation theory and phenomenological models necessarily provide an incomplete understanding of the non-linear, time-dependent, multi-dimensional gas flow within these systems.

Therefore, we wish to solve the equations of fluid dynamics, *i.e.* relations for the conservation of mass, momentum, and energy, under various approximations relevant to our problem (for example, in a rotating binary potential). The conservation of mass is

guaranteed by the continuity equation:

$$\frac{\partial \rho}{\partial t} + \nabla \cdot (\rho \mathbf{u}) = 0,$$

where \mathbf{u} is the vector fluid velocity and ρ the gas density. The conservation of momentum may be written as the Navier-Stokes relation:

$$\rho \left[\frac{\partial}{\partial t} + (\mathbf{u} \cdot \nabla) \right] \mathbf{u} = \mathbf{f} = \mathbf{f}_{\text{external}} + \mathbf{f}_{\text{internal}},$$

where $\mathbf{f}_{\text{external}}$ represents the sum of the external force source terms such as gravity, radiation pressure, etc., and $\mathbf{f}_{\text{internal}}$ represents the sum of internal forces due to fluid stresses. The internal forces can be written as the divergence of the *stress tensor*, τ_{ij} :

$$\mathbf{f}_{\text{internal}} = \nabla \cdot \tau_{ij}.$$

The detailed form of τ_{ij} depends on the nature of the fluid; for a Newtonian fluid (*i.e.* a continuous, isotropic fluid, whose internal stresses are at most a linear function of the fluid shear), the stress tensor may be written:

$$\tau_{ij} = -p\delta_{ij} + \nu \left(\frac{\partial u_i}{\partial x_j} + \frac{\partial u_j}{\partial x_i} \right) + \delta_{ij}\lambda \nabla \cdot \mathbf{u},$$

where p is the thermodynamic gas pressure, ν is the shear viscosity, and λ is the coefficient of bulk viscosity. Hence we see that the internal forces will depend on the gas pressure, the shear and bulk viscosities, and the fluid divergence and shear. The detailed physics of the fluid would determine the nature and magnitude of the viscosity coefficients. For our purposes we will always take the fluid to be *inviscid*; $\nu = \lambda = 0$, hence the Navier-Stokes equation reduces to Euler's equation:

$$\rho \left[\frac{\partial}{\partial t} + (\mathbf{u} \cdot \nabla) \right] \mathbf{u} + \nabla p = \mathbf{f}_{\text{external}},$$

or, in conservative form:

$$\frac{\partial \rho \mathbf{u}}{\partial t} + \nabla \cdot (\rho \mathbf{u} \mathbf{u}) + \nabla p = \mathbf{f}_{\text{external}}.$$

Conservation of energy can be expressed in conservative fashion:

$$\frac{\partial \rho E}{\partial t} + \nabla \cdot [\rho(E + p)\mathbf{u}] = G + \rho \mathbf{u} \cdot \mathbf{f}_{\text{external}},$$

where $E = e + u^2/2$ is the total specific energy (where e is the gas internal energy), and G is an energy source or sink term, such as X-ray heating or radiative cooling. In general, $\mathbf{f}_{\text{external}}$ and G will depend on the detailed physics of the problem.

2.1.1 The Equation of State

Taken together these equations:

$$\partial_t \rho + \nabla \cdot (\rho \mathbf{u}) = 0, \quad (2.1)$$

$$\partial_t(\rho \mathbf{u}) + \nabla \cdot (\rho \mathbf{u} \mathbf{u}) + \nabla p = \mathbf{f}_{\text{ext}}, \quad (2.2)$$

$$\partial_t(\rho E) + \nabla \cdot [\rho(E + p)\mathbf{u}] = G + \rho \mathbf{u} \cdot \mathbf{f}_{\text{ext}}, \quad (2.3)$$

comprise *five* equations for *six* unknowns: ρ , u_x , u_y , u_z , p , and e . We need a final equation describing the relationship between these six quantities. This is called the *equation of state*, and will depend on the detailed physics of the fluid. Typically, we take the equation of state to be that of an adiabatic gas:

$$e = \frac{1}{\gamma - 1} \frac{p}{\rho}, \quad (2.4)$$

where γ is the *ratio of specific heats*, and determines how the gas pressure and internal energy change with temperature. Typically, $1 \leq \gamma \leq 1.7$. For example, for a monatomic

adiabatic gas $\gamma = 5/3$, while for an isothermal gas $\gamma = 1$ (although strictly speaking an isothermal gas is not simply an adiabatic gas with $\gamma = 1$, as inspection of Equation 2.4 makes clear).

Speaking of temperature, we further assume the gas to be *ideal* so that we may define the gas temperature T :

$$T = \frac{m p}{k \rho},$$

where m is the mass of a gas particle, and k is Boltzmann's constant. Finally, it is convenient to define c_s , the sound speed within the gas:

$$c_s^2 = \gamma \frac{p}{\rho}.$$

2.1.2 Eulerian vs. Lagrangian Coordinates

Equations 2.1–2.3 are constructed in *Eulerian coordinates*, *i.e.* they describe the change in density, momentum, and energy for a fixed point in space. We may re-write them in *Lagrangian*, or mass, coordinates for reasons that we shall see shortly. Such equations would describe the evolution of the volume, velocity, pressure, and total energy of a fixed fluid element. For example, in one dimension without source terms, we would write:

$$\partial_t V - \partial_m u = 0,$$

$$\partial_t u + \partial_m p = 0,$$

$$\partial_t E + \partial_m p = 0,$$

$$\rho = 1/V, \quad e = E = \frac{1}{2}u^2, \quad p = (\gamma - 1)\rho e.$$

We see now why we chose to express our problem in Lagrangian coordinates, rather than leaving it in the Eulerian coordinates; this is clearly a much simpler set of equations to solve! Of course, we have the added complexity that the coordinates *move* with the fluid flow, which we will have to contend with.

2.2 Numerical Methods

The codes used to conduct the research within this thesis vary by the particular project, but all are based on Virginia Hydrodynamics 1 (VH-1), developed by the numerical astrophysics group at the University of Virginia between 1990 and 1991, based upon the PPMLR algorithm (Woodward and Colella [1984]; Colella and Woodward [1984]). The original code was developed by John Hawley, John Blondin, Greg Lindahl, Eric Lufkin, and Kazik Borkowski. The particular codes used within these studies have been modified by the author and Dr. John Blondin, and in the case of the GX 301-2 project, Jeff Layton.

2.2.1 Finite Differences

The equations of fluid dynamics, no matter how they are expressed, are a set of coupled, non-linear, time-dependent partial differential equations which do not, except in special cases, lend themselves to analytic solutions. Hence we must solve them numerically. Various methods exist for tackling these equations. We choose *finite differencing*, wherein the derivatives are re-written as small, but finite, differences over a grid of zones:

$$x_{i+1/2}^{n+1} = x_{i+1/2}^n + \Delta t \bar{u}_{i+1/2},$$

$$u_i^{n+1} = u_i^n + \frac{\Delta t}{\Delta m_i} (\bar{p}_{i-1/2} - \bar{p}_{i+1/2}),$$

$$E_i^{n+1} = E_i^n + \frac{\Delta t}{\Delta m_i} (\bar{u}_{i-1/2} \bar{p}_{i-1/2} - \bar{u}_{i+1/2} \bar{p}_{i+1/2}),$$

where the subscript i indicates zone-averaged quantities of the hydrodynamic variables, and the barred variables with $i \pm 1/2$ subscripts indicate the values at the zone interfaces, averaged over the time step Δt , with the superscript denoting the current (n) or next ($n + 1$) time step. Note that the coordinates x_i of the fluid elements change with time. Our task, then, becomes two-fold: find accurate, stable expressions for the hydrodynamic quantities at the zone interfaces, averaged over the time step Δt , and correct for the changing spatial coordinates of the Lagrangian frame. We use the Piecewise Parabolic Method/Lagrangian Remap (PPMLR) formulation of Colella & Woodward to accomplish this.

2.2.2 The Riemann Problem

The Godunov approach to determining the time-averaged zone interface quantities is to treat each zone interface as a one dimensional shock between the fluid on the left of the interface and the fluid on the right. Finding the appropriate relations between these fluid quantities is known as the Riemann problem. The Riemann problem may then be solved iteratively, or in some instances, such as the case of isothermal flow, exactly. The original Godunov method used the zone-averaged quantities of neighboring zones as the left and right input states to the Riemann problem.

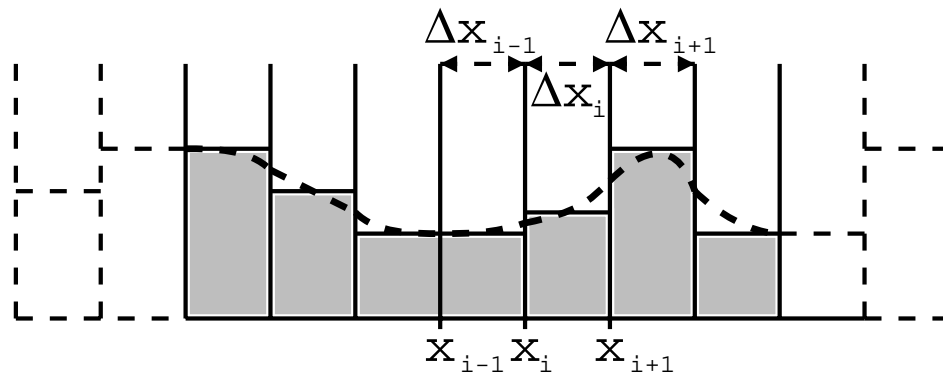


Figure 2.1: Quadratic interpolation based on a five zone stencil centered on the current zone is used to reconstruct the fluid variables as parabolae within each zone.

2.2.3 The Piecewise-Parabolic Method

The PPM algorithm replaces the zone averaged states with a parabolic function within each zone (so that the fluid variables are piecewise-parabolic, hence the name), describing the fluid variables using quadratic interpolations from the neighboring zones. The parabolae on either side of a zone interface are then integrated under to determine the left and right input states to the Riemann problem. The integration is taken to a distance such that an acoustic wave from that distance could just reach the interface in time Δt . This is called the characteristic domain of dependence. This method provides more accurate estimates for the input states; this in turn allows the fluid variables to be more accurately described with fewer zones and less numerical dissipation (error).

2.2.4 Lagrangian Remap

The movement of the coordinates (*i.e.* the zone interfaces) is compensated for using an instantaneous remap from the Lagrangian frame back to the Eulerian frame. In other

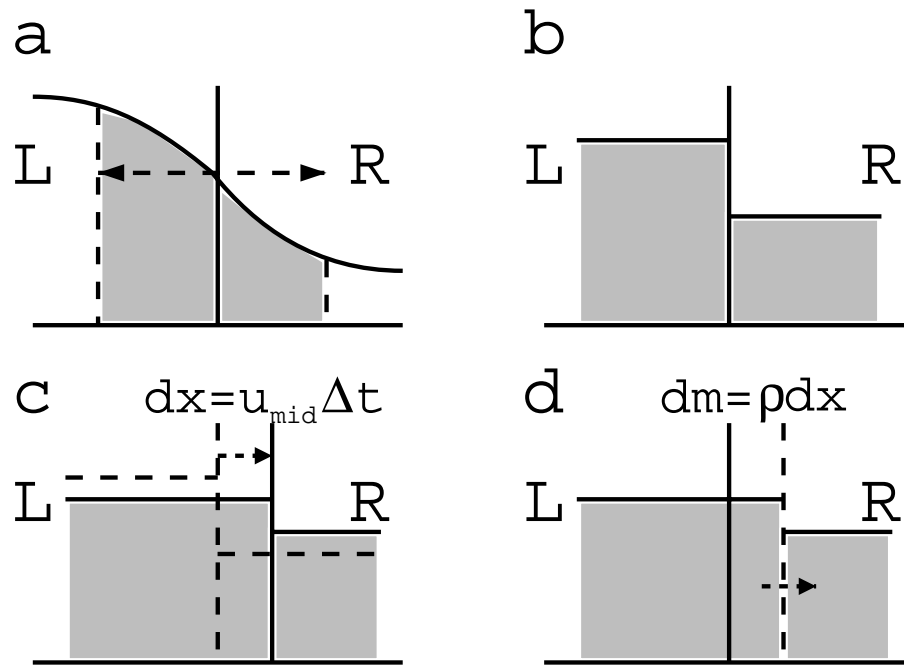


Figure 2.2: The reconstructed parabolae are integrated under on either side of a zone interface (a) to determine the left and right input states to the Riemann problem (b). The Riemann solver returns u_{mid} , the velocity with which the zone interface moves over the time step Δt (c). The conserved quantities (mass, momentum, energy) are then moved via zero-sum fluxes back to the original Eulerian grid (d).

words, the zone averaged values of the fluid quantities are known for a given Eulerian grid, the grid interfaces are allowed to move over a single Lagrangian time step, and then the resulting fluid variables are shuffled via zero-sum conservative fluxes back onto the original Eulerian grid.

2.2.5 Initial & Boundary Conditions

For the solution of partial differential equations we need more information than the equations governing the physics. We need to know the original configuration of the fluid before we evolve it. We cannot simulate all of space, so we must also know what

happens to the fluid at the boundaries of our simulation. These conditions are known as initial conditions and boundary conditions, respectively. In general, these conditions will depend on the particular problem to be solved. The boundary conditions may be different on different faces of the simulation domain. They may be fixed inflow, as in the case of a stellar wind, or fixed outflow, in a case where we do not wish material to propagate back onto the grid. They may be reflective, as though the gas flow were constrained by a brick wall. They may be periodic, as in polar coordinates, where gas leaves one edge of the grid and re-enters the opposite side.

Within VH-1, the initial condition is provided by simply initializing the hydro grid with the fluid variables, ρ, p, \mathbf{u} according to the current problem. The boundary conditions are set within “ghost zones” at the grid boundary that allow the fluid to evolve onto or off of the grid proper. These ghost zones are set either once or twice during each hydro evolutionary step, depending on the version of VH-1. The versions that set the boundaries twice do so once for the Lagrangian hydro and once for the remap. The versions that set the boundaries only once use more ghost zones in order to avoid resetting the boundaries for the remap.

2.3 Grid Forces and Fictitious Forces

For this study it will be convenient to examine two special cases: curvilinear coordinates, and accelerated frames.

2.3.1 Curvilinear Coordinates

Equations 2.1–2.3 hold for any coordinate system. Our problems uniformly lend themselves to spherical coordinates, which are a set of curvilinear orthogonal coordinates. In general, the unit vectors \hat{q}_1 , \hat{q}_2 , \hat{q}_3 of a curvilinear coordinate system are dependent upon the position (q_1, q_2, q_3) . For example, in spherical polar coordinates r, θ, ϕ :

$$\hat{r} = \sin \theta \cos \phi \hat{x} + \sin \theta \sin \phi \hat{y} + \cos \theta \hat{z},$$

$$\hat{\theta} = \cos \theta \cos \phi \hat{x} + \cos \theta \sin \phi \hat{y} - \sin \theta \hat{z},$$

$$\hat{\phi} = -\sin \phi \hat{x} + \cos \phi \hat{y}.$$

Let us examine Equation 2.2. The first term is $\partial_t(\rho \mathbf{u})$. Expanding in terms of spherical polar coordinates we find:

$$\frac{\partial}{\partial t}(\rho \mathbf{u}) = \frac{\partial}{\partial t}[\rho(u_r \hat{r} + u_\theta \hat{\theta} + u_\phi \hat{\phi})],$$

where the unit vectors $\hat{r}, \hat{\theta}, \hat{\phi}$ are subject to the derivative. With much toil, we arrive at:

$$\begin{aligned} \partial_t(\rho \mathbf{u}) &= [\partial_t(\rho u_r) - \frac{\rho}{r}(u_\theta^2 + u_\phi^2)]\hat{r} \\ &+ [\partial_t(\rho u_\theta) + \frac{\rho}{r}(u_r u_\theta - u_\phi^2 \cot \theta)]\hat{\theta} \\ &+ [\partial_t(\rho u_\phi) + \frac{\rho}{r}(u_r u_\phi + u_\theta u_\phi \cot \theta)]\hat{\phi}. \end{aligned} \tag{2.5}$$

The significance of this expression is not obvious. What it states is that we may advect the instantaneous linear momenta $\rho u_r, \rho u_\theta, \rho u_\phi$ along our curvilinear coordinate system, as long as we include the corrective terms arising due to the changing unit vectors. Consider a fluid parcel at a distance R from the coordinate origin and moving tangent to it at a speed u . The instantaneous velocity in spherical polar coordinates is

($u_r = 0, u_\theta = 0, u_\phi = u$). If we allow our particle to only advect in the ϕ direction, it will move in a circle at speed u , *i.e.* it would experience a centrifugal acceleration $-u^2/R\hat{r}$. Adding in the corrective terms insures that inertial flow stays inertial.

This is exactly the way that VH-1 is built to handle orthogonal, curvilinear coordinates. The instantaneous linear momenta along the curvilinear coordinates are the advected conserved quantities, rather than Cartesian linear momenta. Corrective forces, called *grid forces*, ensure that inertial flow remains unaccelerated, regardless of the coordinate system. A consequence of this is that in curvilinear coordinates, momentum may not be conserved exactly. In the absence of forces, the conserved quantities such as mass, momentum, and energy are moved from zone to zone via zero-sum fluxes, and are thus conserved to machine round off error. Forces, however, are calculated using zone-averaged quantities, and are hence in-exact, and the fluid will not behave exactly conservatively. This is crucial in the simulation of accretion disks, where we are extremely interested in the transport of angular momentum.

The core of VH-1 is actually a *one dimensional* hydro solver! It accomplishes the solution of multi-dimensional hydrodynamics problems via a method called *operator splitting* [Strang, 1968]. Essentially, the problem is solved one coordinate dimension at a time. In Cartesian coordinates, a “sweep” is made first in the x , then the y , then the z direction. To avoid a coordinate bias, the sweep is then repeated in the reverse order z, y, x . In the solution of the 1D hydro problem, the transverse momenta do not affect the hydrodynamic solution, they are simply conserved quantities that are advected with the mass. This allows for a clever solution to our problem with the conservation of angular

momentum.

The radial momentum ρu_r , passing through the coordinate origin, carries no angular momentum. Generally in our simulations of accretion disks, $u_\theta/u_\phi \ll 1$, and the disk will be confined to a region near $\theta = \pi/2$ (where $\cot \theta \approx 0$). The dynamics of the disk are dominated by the ϕ angular momentum, while the grid forces depending on u_θ and $\cot \theta$ remain small. Hence we are really only worried about the conservation of ϕ angular momentum when it is advected in the radial direction. Since this is a transverse momentum in this direction, it does not affect the hydrodynamic solution. So we choose to advect the quantity $\rho u_\phi r$ rather than ρu_ϕ (the factor of $\sin \theta$ remains constant along any particular radial, and hence divides out). This conserves the ϕ angular momentum exactly (or at least to within machine round-off error), and alleviates the need for one of the grid force terms in Equation 2.5.

2.3.2 Rotating Frames

In all of our problems it will be convenient to work within a *rotating frame of reference*, one that rotates with the binary orbit. This creates similar problems to those presented by curvilinear coordinates. Consider a fluid stationary in an inertial frame. In the rotating frame, this fluid must advect coherently in rigid-body motion. In the binary frame rotating with angular velocity ω about the system center of mass, the acceleration of a particle within that frame is given by:

$$\mathbf{a} = -2\boldsymbol{\omega} \times \mathbf{u} - \boldsymbol{\omega} \times \boldsymbol{\omega} \times \mathbf{r}_{cm},$$

where \mathbf{r}_c is the position of the particle from the center of mass. The first term is the *Coriolis force*, while the second is the *centrifugal force*. The centrifugal force can be written as the gradient of a scalar potential $\frac{1}{2}(\boldsymbol{\omega} \times \mathbf{r}_{cm})^2$ as in Chapter 1, and included in the total effective potential of the system.

Within VH-1, we account for both the curvilinear coordinates and the rotating frame by the inclusion of the grid forces and the so-called *fictitious forces* as source terms on the right hand side of Equations 2.2 and 2.3, within $\mathbf{f}_{\text{external}}$.

2.4 Parallel Decomposition Using MPI

For Chapter 4, our simulations were undertaken on the IBM SP3 at the North Carolina Supercomputing Center. This is a parallel supercomputer, meaning that many computational processors were employed simultaneously, with the work divided across them. This was done using a version of VH-1 utilizing MPI, or Message Passing Interface, developed by Dr. John Blondin. These simulations take place on a grid of 127 azimuthal \times 127 polar \times 256 radial zones. The computational domain was decomposed into 127 radial-polar planes, one for each azimuthal coordinate, and allocated to 127 different processors on the SP3. Each simulation step then involved a 5 step process: 1) a 2D $r - \theta$ radial-polar hydro evolution step, 2) global transposition of the simulation data from $r - \theta$ planes to $r - \phi$ planes to allow 3) a 1D $\phi - \phi$ double azimuthal hydro evolution step, 4) global transposition back to the original $r - \theta$ decomposition for 5) a 2D $\theta - r$ polar-radial hydro evolution step. This allows operator splitting without coordinate bias, and alleviates the inter-processor boundary condition communication

that would be required with a block domain decomposition; all interprocessor communications are restricted to the data transpositions (for which extremely fast low-level subroutines exist), and a few global all-to-all reductions to find and distribute the global minimum time step (VH-1 calculates the time step adequate for a particular zone on the fly according to quantities such as fluid velocity, sound speed, and zone size; since the entire simulation must use the same time step, the global minimum time step is used).

Chapter 3

Mass Transfer in High Mass X-ray Binaries

High mass X-ray binaries consist of a binary system with a giant or super-giant primary star in close orbit with a collapsed companion, either a black hole or a neutron star. The intense X-ray luminosity of these systems is powered by mass accretion onto the collapsed companion, which in turn is fueled by mass transfer from the primary star. Two possible explanations for the mass transfer are (1) Roche lobe overflow, and (2) gravitational capture of a stellar wind. Most X-ray binaries are found to be in circular orbits due to loss of binary orbital angular momentum in a stellar wind, tidal forces, etc. Yet binary X-ray transients are known where the periodic increase in X-ray activity corresponds with the period of the eccentric binary orbit.

3.0.1 Wind Accretion and Roche Lobe Overflow (RLOF)

This work was presented at the International Astronomical Union conference 163, on Accretion Phenomena and Associated Outflows [Blondin and Owen, 1997].

Perhaps the best discriminant between wind accretion and RLOF is the evolution of

the spin period in X-ray pulsars. Although there is still much to be learned about the accretion of angular momentum in X-ray binaries, the observation of continued spin up in some HMXBs such as SMC X-1 and Cen X-3 is strong evidence for disk accretion and hence RLOF, while the observation of a random walk in spin period in HMXBs such as Vela X-1 argues against the presence of an accretion disk, and hence for wind accretion. This classification is supported by the fact that systems with an observed continuous spin up also exhibit short pulse periods (if they have been spinning up continuously they must now be spinning fast), short orbital periods (the orbit must be close in order for the primary to contact the Roche lobe), and high X-ray luminosity. For example, Centaurus X-3 has a short orbital period (2.1 days), a rapid pulse period (4.8 sec), a high X-ray luminosity (8×10^{37} erg sec⁻¹), and a high, consistent pulsar spin-up rate ($\dot{\nu} = 65.7 \times 10^{-13}$ Hz sec⁻¹), while Vela X-1 has a long orbital period (9 days), a long pulse period (nearly five minutes), a lower luminosity (6×10^{36} erg sec⁻¹), and a low, inconsistent spin-up rate ($1.2 \pm 1 \times 10^{-13}$ Hz sec⁻¹). See Table 3.2 for a representative sampling of galactic and near-galactic HMXBs.

Rather than being considered two separate classes, wind accretion and RLOF should be thought of as two extremes of a continuum of possibilities. Wind-accretion systems may have some tidal focusing of the wind even though the primary star does not fill its Roche lobe, and RLOF systems may still possess a strong stellar wind that may affect the accretion dynamics. Furthermore, the continuum can be thought of as a possible evolutionary sequence. In order for a wind-fed system to be detected, the compact companion must be in a relatively close orbit. If this is the case, further evolution of

	Disk Fed	Wind Fed
P_{orb}	short	long
P_{pulse}	short	long
\dot{P}_{pulse}	steady	random
L_x	high	low

Table 3.1: Distinguishing characteristics of wind fed and disk fed HMXBs. *In general*, HMXBs fall into two distinct categories: (A) the higher luminosity, shorter orbital period, faster pulsed disk accretors that show continuous steady spin up, and (B) the lower luminosity, longer orbital period, slower pulsed wind accretors, which show a random walk in pulse period derivative.

the system will likely bring the primary star into contact with its Roche lobe, driving the system into RLOF. Ultimately this evolution in mass transfer is expected to lead to a common envelope system [Taam and Sandquist, 2000].

One goal of the work described in this chapter is to investigate the properties of mass transfer in HMXBs as a function of the size of the primary star. Our approach is to use a series of two dimensional hydrodynamic simulations varying the size of the primary with respect to its Roche lobe. The 2D model computes the gas flow within the orbital plane, and includes the full potential of the rotating binary system and the radiation force of the primary star modeled in the Sobolev approximation. The influence of the X-rays in the model includes X-ray heating, photoionization (disrupting the Sobolev force), and radiation pressure.

Object	P_{orb} (days)	P_{pulse} (sec)	$\dot{\nu}$ (10^{-13} Hz sec $^{-1}$)	L_x (erg sec $^{-1}$)	Type
LMC X-4	1.4	13.5	—	4×10^{38}	Disk
Cen X-3	2.1	4.8	65.7	8×10^{37}	Disk
SMC X-1	3.9	0.7	233	3×10^{38}	Disk
OA0 1657-415	10.4	37.7	55.8	3×10^{36}	Wind
Vela X-1	9.0	283	1.2	6×10^{36}	Wind

Table 3.2: A representative sample of observed high mass X-ray binaries and their classification as disk or wind fed. Note that the accreting pulsar in LMC X-4 is believed to be in spin equilibrium with the inner edge of its accretion disk, and hence exhibits no continuous net spin up.

3.0.2 Elliptical Orbit XRBs

This work was performed in conjunction with Jeffrey T. Layton, John M. Blondin, and Ian R. Stevens, and published under the title “Tidal mass transfer in elliptical-orbit binary stars,” Layton et al. [1997].

X-ray pulsar binary systems provide a valuable setting for the study of mass transfer in binary stars. The observed X-ray luminosity provides a measure of the mass accretion rate onto the compact object while the changes in pulse period reflect the accretion of angular momentum. Furthermore, the attenuation of the X-rays as inferred from the X-ray spectrum provides a measure of the distribution of circumbinary gas. Such systems are even more valuable when they possess non-circular orbits, for then we have the opportunity to study the mass transfer process under a well-defined experiment: a gradual change in the binary separation.

A number of X-ray binary systems, most of them Be X-ray binaries, are characterized by rather large orbital eccentricities. Many of these systems are X-ray transients, exhibiting distinct episodes of increased X-ray flux. These hard X-ray transients appear to exhibit at least two different types of temporal behavior. In one group are systems like X0115 + 63 [Mendelson and Mazeh, 1991] which sometimes show an optical brightening preceding a relatively long X-ray outburst with approximately linear decline. This association with optical transients suggests that the X-ray outburst is associated with some type of event occurring on the primary (Be) star. In another case, X-ray flares are separated by a relatively constant time interval consistent with the inferred orbital period of the binary system, suggesting instead that the X-ray flares are related to the orbital dynamics of the neutron star. In at least one system, A 1907+09 [Marshall and Ricketts, 1980], an orbital modulation can be seen on top of the long linear rise and fall of an extended outburst lasting several orbital periods. Parmar et al. [1989] list six Be X-ray binaries for which the X-ray flaring interval is at least consistent with the orbital period of the system. At least three systems exhibit X-ray flares occurring close to periastron passage: V 0332+53 [Stella et al., 1985], A 0538-66 [Mavromatakis and Haberl, 1993], and GX 301-2 (Watson et al. [1982]; White and Swank [1984]; Sato et al. [1986]).

Perhaps the best studied elliptical-orbit X-ray pulsar is GX 301-2. The orbit of this system has a period of 41.5 days and an eccentricity of $e = 0.47$ [Sato et al., 1986]. The X-ray flux exhibits periodic flares associated with periastron passage, although the flares occur about 1.4 days before periastron (Watson et al. [1982]; Sato et al. [1986]).

At a distance of 1.8 kpc, the peak X-ray luminosity is $\sim 10^{37}$ erg sec $^{-1}$, compared to a quiescent flux roughly 10 times smaller. There is another periodic flare near apastron seen in BATSE data folded at the orbital period (Pravdo et al. [1995]; Koh et al. [1997]). The peak flux of the apastron flare is of order 4 times smaller than that of the periastron flare. One also sees two flares per orbit in A 1907+09 (Marshall and Ricketts [1980]; Makishima et al. [1984]).

The X-ray pulse period of GX 301-2 also shows some unusual behavior, with an extended epoch of essentially no net change in period from 1975 to 1985 followed by an epoch with fairly steady spin up [Pravdo et al., 1995]. Recent analysis of BATSE data has shown that the long-term spin up trend may be explained by individual episodes of spin up lasting roughly half an orbital period, but occurring only once every one or two years [Koh et al., 1997].

Early optical observations [Parkes et al., 1980] identified the primary star, Wray 977, as a B2 Iae super-giant of radius $R_p = 43R_\odot$, mass $M = 25 - 35M_\odot$ (assuming that the mass of the neutron star $M_{\text{ns}} = 1.4M_\odot$), and a distance $d = 1.8$ kpc. With these parameters, they concluded that the primary is unlikely to fill its Roche lobe at any orbital phase and that GX 301-2 is a wind-fed system.

This conclusion naturally led to the suggestion that the X-ray flares observed in GX 301-2 could be explained by the eccentric binary orbit model of Avni and Goldman [1980]. In this model the X-ray luminosity is modulated by the changing wind conditions as the accreting neutron star moves through its eccentric orbit. Near periastron the stellar wind is slower and denser, leading to a higher mass accretion rate and hence higher

X-ray luminosity compared to apastron. This model provided reasonably good fits to the X-ray light curve, although it could not reproduce a peak luminosity occurring ~ 1.4 days before periastron (Watson et al. [1982]; White and Swank [1984]).

More recent attempts to model the X-ray light curve have resorted to the inclusion of a gas stream both to augment the wind accretion and to provide the observed dependence of column density on orbital phase (Leahy [1991]; Haberl [1991]). The results of this modeling thus suggest that tidal stripping from the surface of the primary star may play a role in the mass transfer process. The possibility that mass transfer is at least augmented by tidal stripping near periastron is also supported by new optical observations of Wray 977. Recently, Kaper et al. [1995] have shown that the optical spectrum of Wray 977 is similar to that of ζ_1 Sco, a B1.5 Ia + “hyper-giant.” Based on this comparison, they suggested a reclassification of Wray 977 to B1 Ia +, and a corresponding change in parameters to $M_p = 50M_\odot$, $R_p = 70R_\odot$, and $d = 5.3$ kpc. These parameters suggest that the volume of the star may be larger than its tidal lobe near periastron, allowing for the possibility of mass transfer via tidal lobe overflow.

Tidal stripping near periastron has also been suggested for A 0538-66 [Skinner et al., 1982], another X-ray binary with a relatively large eccentricity ($e = 0.7$). Stevens [1988] modeled the X-ray light curve of A 0538-66 in terms of accretion from a tidally enhanced stellar wind; the tidal effects of the neutron star near periastron lead to a stronger, slower wind and hence a larger accretion-driven X-ray flux. Mavromatakis and Haberl [1993] argue that the stream model of Haberl [1991] fits the light curve of the two outbursts observed from A 0538-66 by ROSAT in late 1990.

While the modeling of Leahy [1991] and Haberl [1991] suggests the presence of a gas stream in GX 301-2, the existence of a tidally produced stream and its properties require multidimensional hydrodynamic simulations. Along these lines, Boyle and Walker [1986] computed the trajectories of test particles (with some crude modifications to account for hydrodynamic interaction) from the surface of a primary star in a eccentric orbit. They found that the tidally stripped gas can accrete onto the compact companion provided that the primary star rotates with an angular velocity comparable to the orbital velocity near periastron, a requirement previously pointed out by Petterson [1978].

Hence the second goal of this chapter is to determine whether the observed X-ray flares in elliptical-orbit X-ray binaries can be interpreted in terms of wind accretion augmented by tidal lobe overflow at periastron. As a specific example, we base our hydrodynamical model on the parameters for GX 301-2.

3.0.3 3D Global Hydrodynamic Modeling of LMC X-4

This work was first presented at IAU 163 [Owen and Blondin, 1997], and was later published under the title “Testing Hydrodynamic Models of LMC-X4 using Ultraviolet and X-ray Spectra,” [Boroson et al., 2001].

Mass transfer in HMXBs has proved difficult to understand, despite the simplicity of the first analytic descriptions of accretion from a wind [Bondi and Hoyle, 1944]. Problems arise in the theory, for example, when X-ray feedback on the dynamics is considered (MacGregor and Vitello [1982]; Ho and Arons [1987]). The feedback between the X-ray source and a stellar wind can be severe, as the mass accretion rate of a stellar

wind depends strongly on the wind velocity, and the acceleration of the wind can be greatly reduced by X-ray photoionization by the accretor.

Even isolated stellar winds are complex. The line-scattering force accelerating the wind depends on the wind velocity gradient, and is unstable to perturbations in the flow field, leading to shocks (MacGregor et al. [1979]; Abbott [1980]; Lucy and White [1980]; Owocki and Rybicki [1984]) and other nonlinearities that are difficult to model numerically [Owocki et al., 1988].

Near orbital phase 0.8, many XRBs show pre-eclipse dips in X-ray flux that may be caused by the tidal stream crossing the line of sight. Even systems such as 4U 1700–37, thought to accrete via gravitational wind capture rather than RLOF, show increased X-ray absorption at late phase (Haberl et al. [1989]; Heap and Corcoran [1992]), possibly resulting from an accretion wake trailing a bow shock in the wind.

4U 1700–37 and Vela X-1 both exhibit increased optical line absorption at late phase. An accretion wake is not expected to be large enough to explain this absorption. Rather, interaction between the wind and the X-ray flux from the accretor, in the form of a photoionization wake [Fransson and Fabian, 1980], may produce the absorption [Kaper et al., 1994]. The photoionization wake might also explain the asymmetric X-ray eclipse in Vela X-1 [Feldmeier et al., 1996]. Photoionization wakes are seen in 2D hydrodynamic simulations (Blondin et al. [1991]; Blondin [1994]) such as those in the first section of this chapter. The wake results when fast moving stellar wind collides with slower moving wind that has been stalled by X-ray photoionization. Near the eclipse ingress line, the X-ray shadow of the donor allows the fast moving wind to continue to accelerate into

the stalled wind.

Observations of X-ray dips and eclipses have not provided us with information about the velocity field of the wind. Rather, UV P Cygni line profiles, formed by resonant scattering in the wind, are used. P Cygni lines occur in a diverging wind accelerated by line transitions; lines from the far side of the star are from gas that is moving away from us, and are red-shifted emission lines, while lines from the near side of the star are from gas that is in front of the star and moving toward us, hence they should be blue-shifted absorption lines. P Cygni lines in an HMXB are expected to vary over the binary orbit in a predictable way, referred to as the Hatchett-McCray effect [Hatchett and McCray, 1977], such that the ions responsible for the line are photoionized near the X-ray source; near phase 0.0 the blue-shifted absorption is diminished, while near phase 0.5 the red-shifted absorption is diminished. Thus certain features of the line profile will shift throughout the orbit in a way depending on the velocity field of the wind. McCray et al. [1984] used this method to infer the mass-loss rate and terminal wind velocity of Vela X-1. Kaper et al. [1993] showed that the P Cygni line variation in Vela X-1 suggests that the wind velocity does not increase monotonically with radius, while analysis by Boroson et al. [1999] attempted to infer the radial velocity law of LMC X-4 using this technique.

We attempt in this section to model the detailed three dimensional circumstellar gas dynamics of a high mass X-ray binary, with the inclusion of as many detailed physical processes as possible. All of these processes are modeled under certain limiting assumptions to make the problem tractable. We wish to understand the main features of such

systems, and compare our results to observations including pre-eclipse dips and P Cygni profiles.

The parameters of this model were chosen in accordance with the observed parameters of LMC X-4 because it is a clear disk accretion candidate; the high X-ray luminosity of LMC X-4 is difficult to reconcile with wind accretion alone, and the presence of a 30 day period in the X-ray light curve [Lang et al., 1981] and in the optical light curve [Heemskerk and van Paradijs, 1989] suggests a precessing accretion disk fed by Roche lobe overflow. LMC X-4's short orbital period of 1.41 days implies that the X-ray source orbits quite close to the surface of the donor star, making it likely that the donor fills its Roche lobe.

Our final goal within this chapter then is to quantify the dynamics of our full 3D model, using all of the physics included (stellar wind, X-ray heating, photoionization, radiation pressure, and attenuation due to circumstellar gas, and tidal forces), in order to better understand observations of these systems.

3.1 Numerical Model

We employ the basic numerical model of Blondin et al. [1990] and Blondin et al. [1991]. We employ a 2D spherical coordinate simulation of the gas dynamics in the orbital plane. The numerical grid is centered on the center of mass of the binary. The mass ratio $q = 10$ was chosen to be large for two reasons: 1) to keep the center of mass near the center of the donor star, such that the inner edge of the numerical grid could be entirely contained within the donor's surface, and 2) to simulate the large mass ratios

typical for binaries containing early-type donors that may be driving a strong stellar wind.

The donor star is assumed to be in synchronous rotation with the binary orbit, which is assumed to be circular. The surface of the donor is chosen to be an equipotential surface of the effective potential in the binary orbit:

$$\Phi_{\text{eff}} = -\frac{GM_1}{r_1} - \frac{GM_2}{r_2} - \frac{1}{2}(\boldsymbol{\Omega} \times \mathbf{r}_{\text{cm}})^2,$$

where Ω is the binary orbital velocity.

We define the *Roche overflow parameter* to be the ratio of the donor surface potential to the critical potential:

$$\lambda = \frac{\Phi_{\text{surf}}}{\Phi_{\text{crit}}},$$

where the critical potential is the potential at the inner Lagrange point, or L1, and hence defines the surface of the Roche lobes. Because Φ is always negative and decreases within the Roche lobe with decreasing distance from the donor's center of mass, increasing values of λ represent smaller and smaller surfaces within the critical surface. A $\lambda = 1.2$ fills a smaller fraction of its Roche lobe than does a $\lambda = 1.1$, where a $\lambda = 1$ star completely fills its Roche lobe.

The atmosphere of the donor star is assumed to be in thermal equilibrium at temperature T , and is hence supported hydrostatically:

$$-\frac{GM\rho}{r^2} = \frac{dp}{dr} = \frac{kT}{\bar{m}} \frac{d\rho}{dr},$$

where k is Boltzmann's constant, and \bar{m} is the average mass of a gas particle. Integrating

yields an exponential atmosphere for the donor:

$$\rho(r) = \rho_0 e^{-r/r_0}, \quad (3.1)$$

where $r_0 = GM\bar{m}/kT$ is the atmospheric scale height. Note the approximation that the force felt in the atmosphere of the donor is due entirely to the donor's mass. In reality, the force is determined by the gradient of the effective potential; the atmosphere is still exponential, but the scale height may vary for different regions of the surface. For a Roche filling star, we expect the scale height to become large at the L1 point, where the gradient of the effective potential vanishes.

The grid is initialized with a fiducial density $\rho_0 = 5.0 \times 10^{-9} \text{g cm}^{-3}$ at the critical potential; several zones *within* the critical surface are set according to the prescription of Equation 3.1 and act as the inner radial boundary condition. These zones are reset following every time step assuming the donor star's atmosphere to be static.

The grid is initialized outside of the donor surface with a Castor-Abbot-Klein (CAK) stellar wind [Castor et al., 1975]. This wind is driven via radiation pressure from the donor's photosphere due to scattering from bound-bound absorption in the circumstellar gas. We assume a surface temperature of 40,000 K for the donor; the wind is driven by UV line transitions within the gas. The radiation pressure felt by the wind particles can be written in the Sobolev approximation:

$$F_{\text{rad}} = \frac{\sigma_e L_\star}{4\pi cr^2} \kappa K \left(\frac{1}{\sigma_e \rho v_{\text{th}}} \frac{dv_r}{dr} \right)^\alpha.$$

L_\star is the luminosity of the donor, σ_e is the electron scattering cross section, $v_{\text{th}} = \sqrt{3kT/\bar{m}}$ is the thermal velocity of the gas, κ and α are constants representing the

number and strength of the UV absorption lines in the gas, and K is a correction factor to produce a shallower velocity law and higher terminal velocity, in agreement with observations [Friend and Abbott, 1986]. This approximation is valid only with the assumption that the scale of the flow velocity gradient exceeds the scale of the ion distribution in the wind. In fact the radiation pressure mechanism is unstable to velocity field perturbations, but since the growth of these instabilities does not seem to affect the average wind properties [Owocki et al., 1988], and we are interested in the accretion dynamics rather than the wind dynamics *per se*, we choose to restrict our problem with this simplification.

The surface density ρ_0 was determined empirically to produce a stable stellar wind with CAK parameters $\alpha = 0.53$, $\kappa = 0.12$, which were themselves chosen based on the spectral type of LMC X-4's donor. In the absence of a companion, this model would drive a spherical stellar wind with a mass loss rate of $\dot{M}_w \approx 2 \times 10^{-7} M_\odot \text{yr}^{-1}$ and a terminal wind velocity of $v_\infty \approx 2000 \text{ km sec}^{-1}$.

Because the intense X-ray flux may fully ionize the circumstellar gas, stripping the atoms of the electrons that create UV line transitions, the radiation pressure felt by the wind is terminated by strong X-ray flux. The exact process is complicated, due to the large numbers of ions and transitions, but an approximation can be made wherein the radiation force is set to zero when the X-ray flux exceeds some critical value determined by assuming the flow to be in ionization equilibrium (a reasonable assumption given that the ionization and recombination time scales are smaller than the flow time scale; Blondin et al. [1990]); the ionization state depends only on the X-ray spectrum and the

local ionization parameter $\xi \equiv 4\pi\bar{m}F_x/\rho$, *i.e.* the ratio of the X-ray flux to the number density of the gas. If ξ exceeds some critical value ξ_{crit} , the UV radiative pressure force is set to zero; below the critical value, the wind is unaffected. Following Blondin et al. [1990] we choose $\xi_{\text{crit}} = 10^{2.5}$ erg cm sec⁻¹, which should be valid for optically thin gas. For optically thick gas, we expect the X-rays to be shadowed anyway.

The X-ray flux is attenuated as it passes through the circumstellar gas; we calculate the local X-ray flux and ionization parameter by integrating the optical depth τ from the accreting X-ray source to each fluid zone within the hydrodynamics grid:

$$\tau = \int_X d\tau,$$

where $d\tau = \rho\sigma_x dr/\bar{m}$. σ_x is the opacity. The flux at any zone is then:

$$\phi_x = \frac{L_x}{4\pi r^2} e^{-\tau}.$$

We use this to calculate the photoionization parameter ξ , the X-ray heating of the gas, and the X-ray radiation pressure.

The opacity data were obtained from Krolik and Kallman [1984], and are roughly fit by the function

$$\log(\sigma) = -21.8 - \frac{3}{4}[\log(T_4)]^2,$$

where T_4 is in units of 10^4 Kelvin and σ is in units of cm². Behavior of this opacity outside of the range 10^4 – 10^6 K may be unphysical; however since the system is constrained to a minimum temperature in thermal equilibrium with the donor (4×10^4 K) to avoid adiabatic cooling as the wind diverges, and gas above 10^6 K is essentially transparent over the size of the system, we feel this form is adequate.

X-ray heating occurs when the X-ray photons ionize the gas. Radiative cooling acts to lower the gas temperature. For higher ionization parameters, Compton scattering dominates, and the X-rays may either heat or cool the gas depending on whether the gas is hotter or cooler than the Compton temperature. We assume that where the critical ionization parameter is exceeded, Compton scattering dominates. Therefore at each time step we calculate the X-ray heating rate and X-ray and normal radiative cooling rates for each hydrodynamic zone; these become source and sink terms in the energy equation (Equation 2.3). We restrict the cooling of the gas such that the minimum gas temperature is the surface temperature of the mass donor (40,000 K).

The force due to the X-ray radiative pressure is assumed to be:

$$f_x = \frac{\phi_x \sigma_T}{c}.$$

The X-ray luminosity $L_x(t)$ of the accreting neutron star is calculated from the time dependent accretion rate. For the 2D simulations we must make some assumptions about the vertical accretion scale. We chose a scale appropriate for disk accretion for all models, in order to make comparisons between models. However, this leads to unusually low accretion rates for the wind accretion models, since gravitational focusing in the third dimension is important.

The mass accretion rate is determined by evacuating the zone containing the compact star at each time step, and converting the mass removed into an accretion luminosity appropriate for an accreting neutron star:

$$L_x(t) = \eta \dot{M} c^2 = \eta c^2 \frac{\rho A h}{\Delta t},$$

where ρ is the gas density removed from the accretion zone, A is the area of the accretion zone, h is the assumed vertical scale factor, and η is the accretion efficiency, here assumed to be 0.1. The X-rays are assumed to travel with infinite speed throughout the system; this is justified since the time step of the simulation is larger than the light crossing time for the system.

The two dimensional numerical grid consisted of a spherical polar grid with 251 angular zones and 400 radial zones, in a reference frame centered on the center of mass of the system and corotating with the neutron star. The first 100 radial zones are equally spaced, while the last 300 grow consecutively larger, with each being 1.006 times the size of the previous zone. The azimuthal angular width of the zones starts at 2.8×10^{-3} radians at the location of the neutron star, and is similarly zoomed by a factor of 1.028. This grid provides high resolution at the surface of the primary in order to resolve the tidally distorted atmosphere, as well as in the vicinity of the accreting neutron star.

For the 2D and 3D non-elliptical models, a donor mass of $14.8M_{\odot}$ and a neutron star mass of $1.4M_{\odot}$ were used, with an orbital period $P_{\text{orb}} = 1.41$ days. The surface temperature of the donor was assumed to be $T_{\star} = 40,000$ K. These are the inferred parameters of LMC X-4.

3.1.1 Modifications for Elliptical Orbits

For the 2D elliptical orbit simulations, the flow was computed in a non-inertial frame in instantaneous corotation with the orbital system such that the neutron star remains at a fixed angular coordinate on the numerical grid, but changes position in the radial

coordinate.

We assume that the surface of the donor is an equipotential surface whose volume is conserved throughout the orbit, and that the donor's axis of rotation is aligned with the axis of orbital rotation of the system. This first assumption requires that the donor star can respond instantaneously to the changing binary potential. Koh et al. [1997] argue that is a reasonable assumption for Wray 977 based on the analysis of tidal excitations by Kumar et al. [1995]. For the purposes of this project we have assumed that the donor's volume is equal to the volume of the critical lobe at periastron. Thus the primary is marginally overflowing its tidal lobe at periastron, but is under-filling at all other orbital phases. In a system with the center of mass at the origin, the neutron star at \mathbf{r}_1 and the donor at \mathbf{r}_2 , the effective potential for a parcel of gas rotating with the donor at a position \mathbf{r} with respect to the center of mass of the system is given by:

$$\Phi_{\text{eff}} = -\frac{GM_1}{|\mathbf{r} - \mathbf{r}_1|} - \frac{GM_2}{|\mathbf{r} - \mathbf{r}_2|} - \frac{1}{2}\omega^2 r^2 - \frac{1}{2}(\omega_d^2 - \omega^2)r_2^2,$$

where ω is the instantaneous angular velocity of the system and ω_d is the rotational angular velocity of the donor.

In practice these assumptions required us to first find the volume of the equipotential surface of the critical lobe at periastron, and fix this as the volume of the star. Once this volume was calculated, a root finding method was employed to find the effective potential of an equipotential surface with this same volume for 200 equally spaced values of the binary separation between periastron and apastron. These data were then stored in a table for use by the hydrodynamic code, which computed the boundary of the primary star in the orbital plane based on the tabulated value of the surface potential.

The change in the angular velocity of the rotating frame ω necessitates the inclusion of new fictitious forces. Specifically, the acceleration felt by a parcel of gas in a frame rotating with non-constant angular velocity becomes:

$$\mathbf{a} = -2\boldsymbol{\omega} \times \mathbf{u} - \boldsymbol{\omega} \times \boldsymbol{\omega} \times \mathbf{r}_{cm} - \dot{\boldsymbol{\omega}} \times \mathbf{r},$$

where $\dot{\boldsymbol{\omega}}$ is determined by the orbit of the neutron star. The $-\dot{\boldsymbol{\omega}} \times \mathbf{r}$ term becomes a new source term in Equations 2.2 and 2.3.

Finally, system orbital parameters appropriate to GX 301-2 were used: $P_{\text{orb}} = 41.5$ days, $e = 0.47$, $M_2 = 52M_{\odot}$ ($q = 37.14$), $T_{\star} = 22,000$ K. The CAK wind parameters appropriate for Wray 977 (based on estimates from Pauldrach et al. [1986]), yield a wind mass loss rate (in the absence of a companion) of $\dot{M}_w \approx 10^{-6}M_{\odot} \text{ yr}^{-1}$, and a terminal wind velocity of $\sim 1000 \text{ km sec}^{-1}$. An accretion efficiency of $\eta = 0.05$ was used for these simulations.

3.1.2 Modifications for 3D Simulations

In order to keep the problem computationally tractable, our numerical resolution in 3D was lowered to 188 radial by 63 polar by 201 azimuthal zones. The grid was structured to provide the highest spatial resolution near the surface of the distorted donor and near the accreting compact object.

The numerical simulation was initialized with the surface of the primary star just inside the critical potential surface, such that the effective potential at the stellar surface was greater than the critical potential by one part in 10^5 , or $\log(\lambda - 1) = -5$. At the stellar surface temperature of 4×10^4 K, the scale height in this atmosphere is $\sim 10^9$ cm.

From numerical experiments we found that VH-1 could simulate a stable atmosphere with zone spacing as large as twice the scale height; this is the value used in the present model. Hence our loss of numerical resolution did not adversely affect our results. The exception is on two limbs of the donor's surface, where the equipotential surface passes at a steep angle through the numerical grid; in these areas the CAK wind failed to form. However, these regions are relatively narrow, are confined to the far side of the donor from the accretor, do not contribute to the accretion column, and do not contribute significantly to the integrated column density along lines of sight that intersect them.

The model is evolved only in one hemisphere, assuming reflection symmetry about the equatorial plane. In addition, a cone about the polar axis is removed from the simulation to reduce the number of time steps needed in the simulation. The use of an explicit hydrodynamics code restricts the time step to the smallest value of $\Delta x/v$ on the grid, where Δx is the width of a numerical zone, and v is a characteristic velocity (the higher of either the gas velocity or the sound speed). On a spherical grid Δx in the ϕ direction is given by $r \sin \theta \Delta \phi$. Therefore, as $\theta \rightarrow 0$, the zone width $\Delta x \rightarrow 0$ and $\Delta t \rightarrow 0$. Thus, to keep a reasonable value of Δt , we limited the simulation domain to $\theta > 0.3\pi$.

The mass accretion rate and X-ray luminosity now contain no assumptions about the vertical dimension; the X-ray luminosity is simply given by

$$L_x(t) = \eta \frac{\rho V}{\Delta t},$$

where V is the volume of the accretion zone containing the neutron star.

Note that the assumption of reflection symmetry restricts the flow of the accretion

disk to the orbital plane; the disk cannot become tilted (although the physics required to tilt the disk are not present in this model in any case). Thus we cannot model the 30 day super-orbital periodicity in LMC X-4 that is believed to arise due to a tilted, precessing accretion disk.

3.2 Results

3.2.1 Wind Accretion and RLOF

For values of $\log(\lambda - 1) \gtrsim -1.8$ we find steady wind accretion of order $\lesssim 10^{34}$ erg sec⁻¹, and the formation of a photoionized region of stalled donor wind, while for $\log(\lambda - 1) \lesssim -2.2$ we find the formation of a steady accretion disk and accretion luminosities exceeding 2×10^{35} erg sec⁻¹, all the way up to the Eddington luminosity, about 1.7×10^{38} erg sec⁻¹.

The transition from wind accretion to RLOF is illustrated in Figure 3.1, where we plot the mass accretion rate onto the compact companion as a function of the RLOF parameter. At small values of $\lambda - 1$ the primary is asymptotically approaching full RLOF, and the data points from the models are well fit by an exponential. Given that the surface of the primary is modeled as an isothermal (exponential) atmosphere, this result is simply stating that the mass loss rate from the primary (now dominated by the tidal stream) is proportional to the gas density at the inner Lagrangian point; had the simulations been allowed to run long enough to raise the disk density high enough, all of the disk systems would accrete at the Eddington rate. At the other extreme, pure

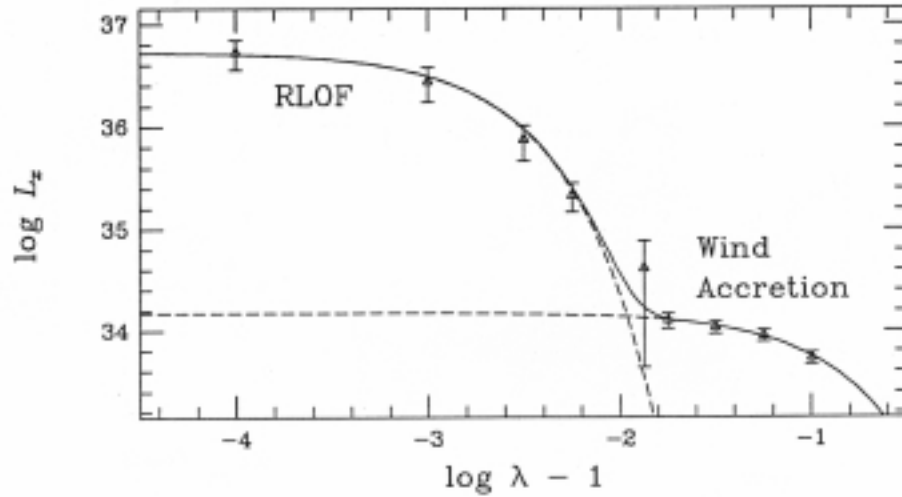


Figure 3.1: Accretion driven X-ray luminosity as a function of the RLOF parameter λ , defined in the text. The solid line is a fit using two exponential curves (dashed lines) corresponding to pure RLOF or wind accretion. The error bars on each model data point represent the typical variation in L_x .

wind accretion, the mass loss rate from the primary has a shallow power law dependence, originating from the dependence of a classical CAK wind on stellar radius. The resulting mass accretion rate is then fit reasonably well by a weak exponential, as shown in Figure 3.1.

The relatively sharp transition from wind-fed to RLOF in HMXBs is due to the small scale height in the atmosphere of the primary compared with the radius of the star. Once the upper atmosphere of the star comes in contact with the Roche surface, small changes in the stellar radius produce exponentially large changes in the mass transfer through the inner Lagrange point.

Another interesting feature of these simulations is the nature of the transitional case,

where the mass loss rate from the primary is still dominated by the wind, but there is substantial focusing of this wind into a weak tidal stream. While the mass loss rate is nearly that of an isolated stellar wind, the mass accretion rate is significantly higher than in the wind accretion case. The large error bars in Figure 3.1 for this model signify extreme variations in the mass accretion rate (see Figure 3.2) resulting from the dynamical interaction between the wind accretion bow shock and the weak tidal stream.

The temporal behavior of the accretion is significantly different, both between wind-fed and RLOF systems, but also compared to the transitional case. Figure 3.2 shows the X-ray light curve for wind-fed, RLOF, and transitional models. Again, to compute a mass accretion rate from a 2D model one must assume something about the neglected third dimension, and in particular what one assumes for wind-fed accretion is likely to be very different from disk accretion. We have opted to choose a height characteristic of disk accretion for all models, and for that reason the wind-fed models have a relatively low accretion driven luminosity. Furthermore, the wind accretion case has relatively poor numerical resolution.

Despite these caveats, Figure 3.2 illustrates what we believe to be real differences between these cases. For example, the disk case has significantly more power on long time scales (hours) than the wind case. The power spectrum from the disk model exhibits a roughly ν^{-1} power law frequency dependence with an additional broad peak at $\nu \sim 2 \times 10^{-3}$ Hz, a frequency this characteristic of epicyclic motions within the disk interior. In contrast, the power spectrum from the wind model is almost flat at low frequencies. We can see major differences in the time variability of the transitional case

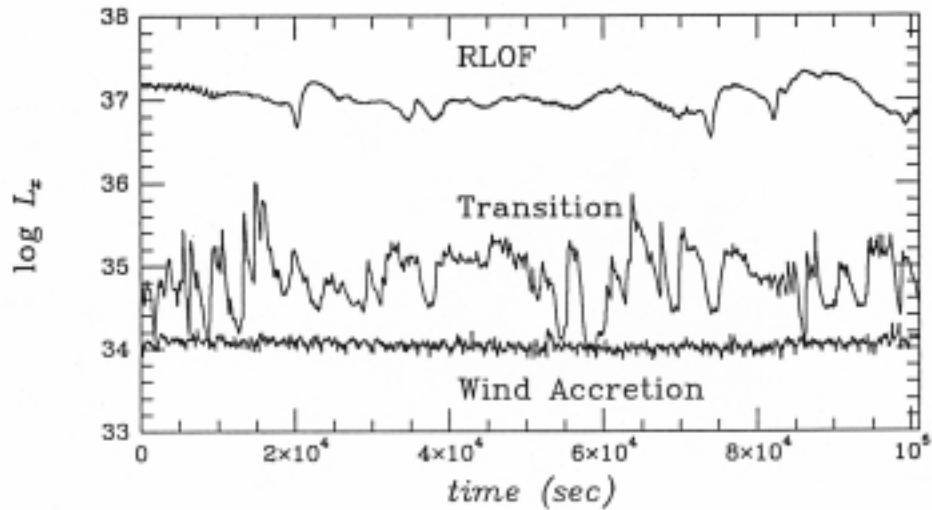


Figure 3.2: Accretion driven X-ray light curves from three different models corresponding to wind accretion, RLOF, and a transitional case.

vs either the pure wind accretion or pure disk case. This might allow use to distinguish wind accreting systems on the verge of becoming disk fed systems. One can interpret the violent variability in the context that gravitational focusing is *trying* to form a disk behind the accretion bow shock, but the disk is disrupted by the wind. We may expect violent variability and some net accumulation of angular momentum in such a system (again due to tidal focusing), with relatively low X-ray luminosity and spin up rate.

The results described above are useful for interpreting individual HMXBs and for understanding the evolution of these systems, but they are necessarily incomplete because mass transfer in binary systems is inherently three dimensional. The amplitude of the RLOF and wind accretion curves in Figure 3.1, and hence the location of the transition from RLOF to wind accretion, will undoubtedly differ in three dimensions,

but the essential conclusions should remain; the transition from wind accretion to RLOF in HMXBs is sharp, and on time scales of minutes to hours the temporal behavior of wind accretion, RLOF, and the transitional case are qualitatively different.

3.2.2 Elliptical-Orbit Binary Stars

We ran two simulations for GX 301-2, each with a different rotation rate for the primary. Observational evidence favors a slow rotation with a period comparable to the orbital period [Parkes et al., 1980], so for our first model we chose a slow rotation rate. Since Boyle and Walker [1986] argue the need for a fast rotation rate, we ran a second (fast) model with a rotational velocity equal to the orbital velocity at periastron. The other parameters used in the model are based on the parameters for GX 301-2 derived by Kaper et al. [1995], which are more consistent with the tidal overflow model being investigated here.

Case I: Slow Rotator

In the first model, the rotation period of the primary was set to the orbital period of 41.5 days. At this value the rotation of the primary star lags far behind the orbiting neutron star during periastron passage. Petterson [1978] pointed out that in such circumstances tidally stripped gas will have insufficient specific angular momentum to reach the neutron star. The sequence shown in Figure 3.3 confirms this; mass transfer remains in the wind accretion mode throughout the orbit. A small tidal stream briefly forms during the periastron passage, but most of this mass falls back to the surface of the primary as the neutron star recedes from it.

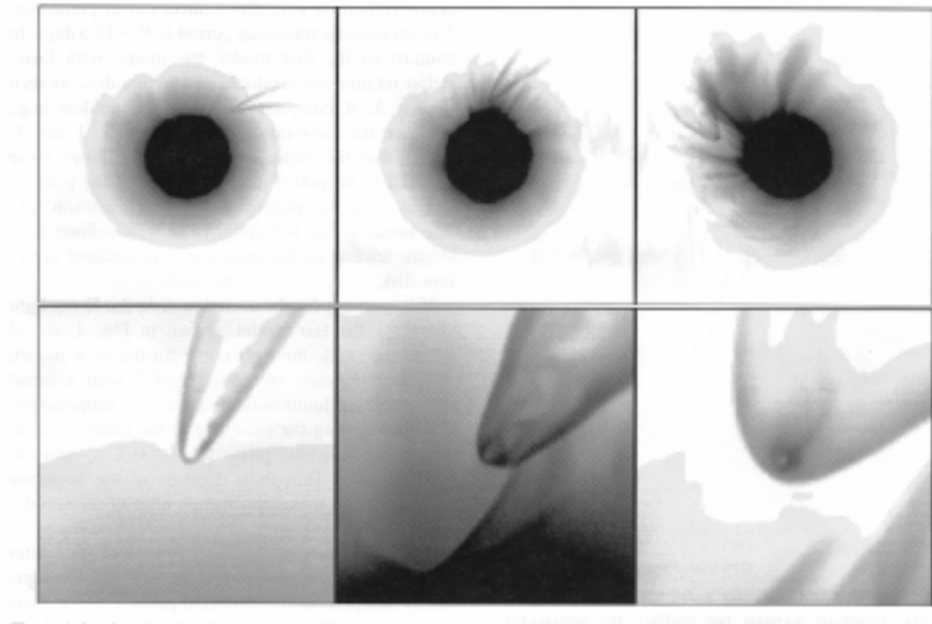


Figure 3.3: Time series of the slow rotator model showing the entire orbital system (top) and a close up of the accreting neutron star (bottom). The gray-scale represents circumstellar gas density, increasing from light to dark. The close up images are views in a rotating frame such that the donor star is always below the frame, while the global images are shown in an inertial frame, with the system's orbital motion shown.

The X-ray light curve, shown in Figure 3.4, exhibits a broad peak in L_x from slightly before periastron to phase 0.12. The peak luminosity reaches $L_x \approx 10^{35}$ erg sec⁻¹, compared to $L_x \approx 5.0 \times 10^{33}$ erg sec⁻¹ far from periastron. This increase is the result of the strong enhancement of wind accretion near and after periastron. The stellar wind originating from the line of centers during periastron passage has a substantially lower velocity and higher mass loss rate than the undisturbed stellar wind, resulting in a larger wind accretion rate. In fact our numerical model underestimates this increase in wind accretion because of our assumptions about the third dimension. The slower wind velocity results in a larger accretion radius than was assumed in the numerical model, with the result that the X-ray luminosity output by the model is a few times too low. Given this restriction, the height of the periastron peak (one order of magnitude) is uncertain, but the duration in orbital phase is expected to be reasonably accurate.

The angular momentum accretion rate, \dot{J} , remains low throughout the simulation. Away from periastron the sign of \dot{J} is uniformly positive, although we note that the hydrodynamics of the wind accretion are poorly resolved during this part of the orbit. In the vicinity of periastron \dot{J} shows clear oscillations in sign, with the result that there is virtually no net angular momentum accreted during periastron passage, as shown in the plot of accumulated angular momentum, J , in Figure 3.4. During this part of the orbit the wind velocity is lower, the accretion radius is higher, and the grid spacing is finer, such that the hydrodynamics of the wind accretion are adequately resolved. Given sufficient numerical resolution, we might expect the time-averaged value of \dot{J} to remain approximately zero throughout the orbit, and not just during periastron passage.

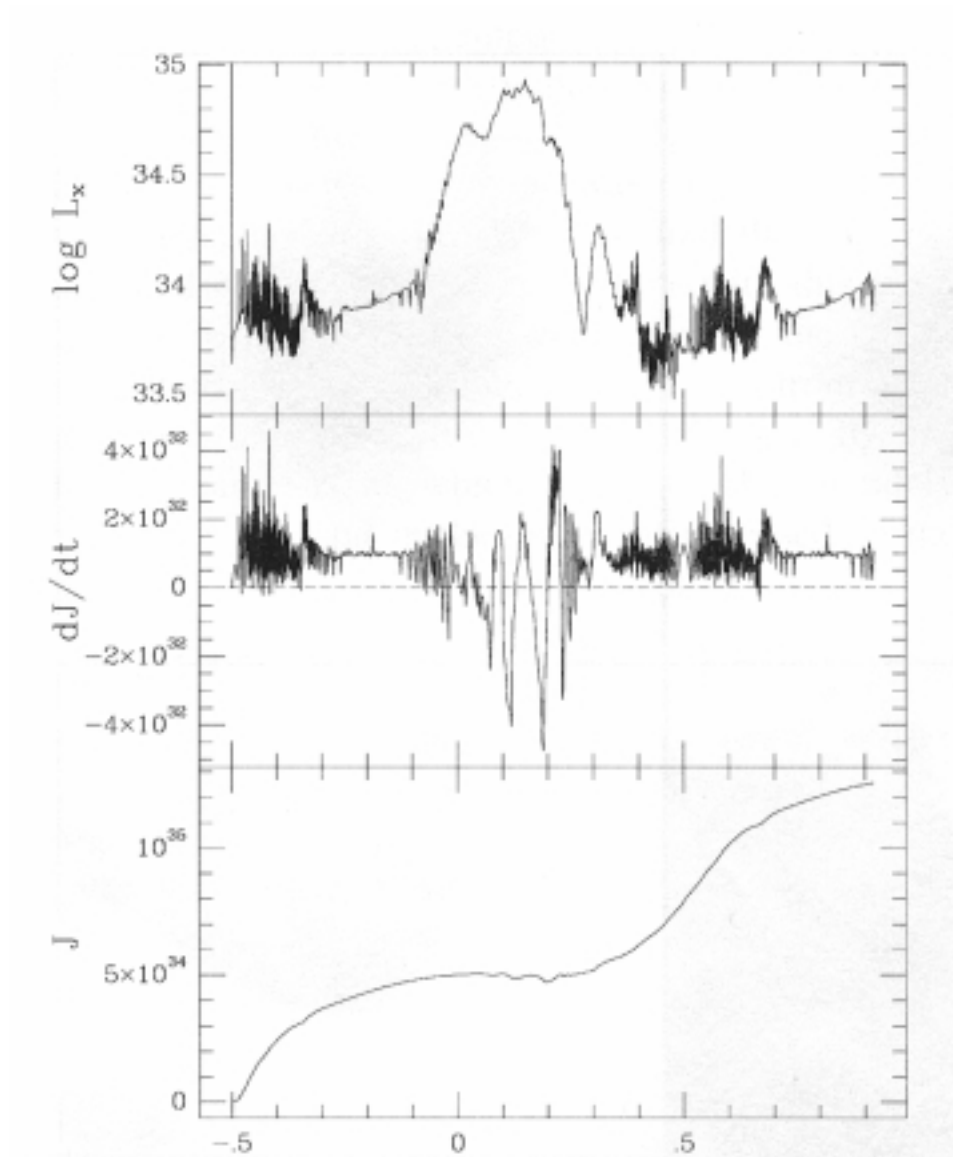


Figure 3.4: Evolution of the accretion driven X-ray luminosity (top), angular momentum accretion rate (middle), and accumulated angular momentum of the neutron star (bottom) for the slow rotator model.

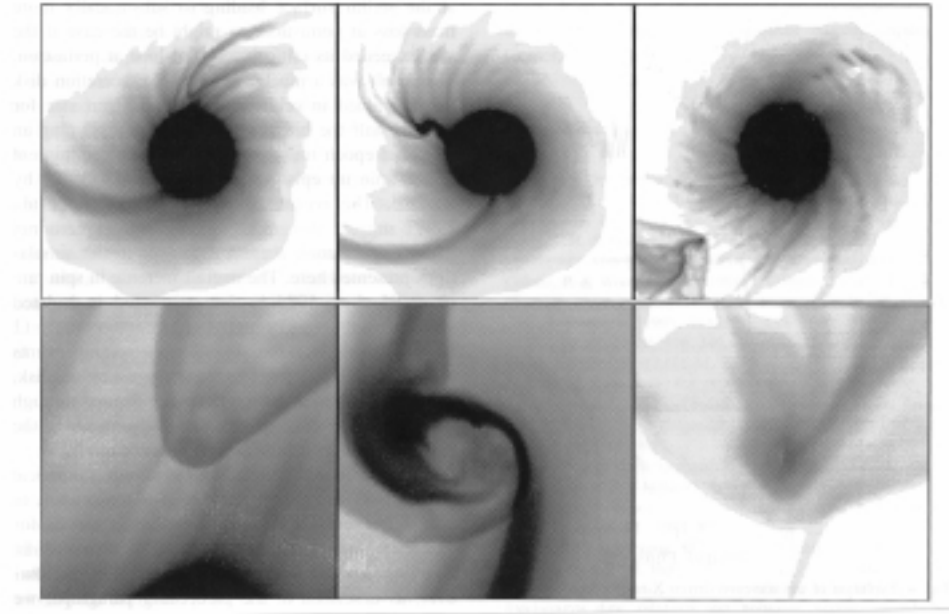


Figure 3.5: Time sequence of the fast rotator model, as in Figure 3.3.

Case II: Fast Rotator

In the second model the rotation of the primary star was adjusted such that the star was in instantaneous corotation with the neutron star at periastron. The appropriate rotational period is $P = 12.5$ days. In contrast to the first model, the model with fast stellar rotation did produce an accretion disk, as seen in Figure 3.5. A comparison of the two models (*e.g.*, compare the close-up sequences in Figures 3.3 and 3.5) shows that the faster stellar rotation allows more material to be pulled off the surface of the primary and more of this material to reach the neutron star. The result is the formation of a well defined tidal stream leading to the presence of a transient accretion disk.

If it were not for the accretion disk, the X-ray light curve for the fast model, shown in Figure 3.6, would closely resemble the light curve for the slow model: a base luminosity

of $\sim 10^{34}$ erg sec $^{-1}$ with a broad peak reaching luminosities roughly ten times larger. However, during the existence of the accretion disk, roughly from orbital phase 0.13 to 0.3, L_x soars to $\sim 10^{36}$ erg sec $^{-1}$. This short duration of the accretion disk appears consistently in each orbit of the simulation.

The accretion disk does not form until well after periastron because of the time necessary for the gas tidally stripped during periastron passage to reach the neutron star. The densest material pulled off the surface is moving with a radial velocity of only slightly more than 100 km sec $^{-1}$ and hence requires at least a day to reach the neutron star. Even then it takes a significant amount of time for the gas to encircle the neutron star and begin accreting. Shortly after the disk forms, however, an interesting phenomenon occurs. The angular momentum accretion rate, although starting off positive when the disk forms, rapidly drops to negative values of comparable magnitude to the positive disk accretion rate. This sudden switching of the sign of \dot{J} is shown in Figure 3.6, where we also plot the accumulated angular momentum, J . From this latter plot one can see that the total amount of angular momentum accreted with opposite rotation is comparable to, and indeed for the first orbit larger than, the total angular momentum accreted with positive rotation. This switch in the direction of rotation of the accreting material coincides with the peak in the mass accretion rate.

The antirotation of the accreting material appears to be driven by the passage of tidally enhanced wind as the motion of the neutron star slows down with respect to the rotation of the primary star. In a circular orbit system the gas flowing through the inner Lagrangian point has insufficient angular momentum to accrete directly onto

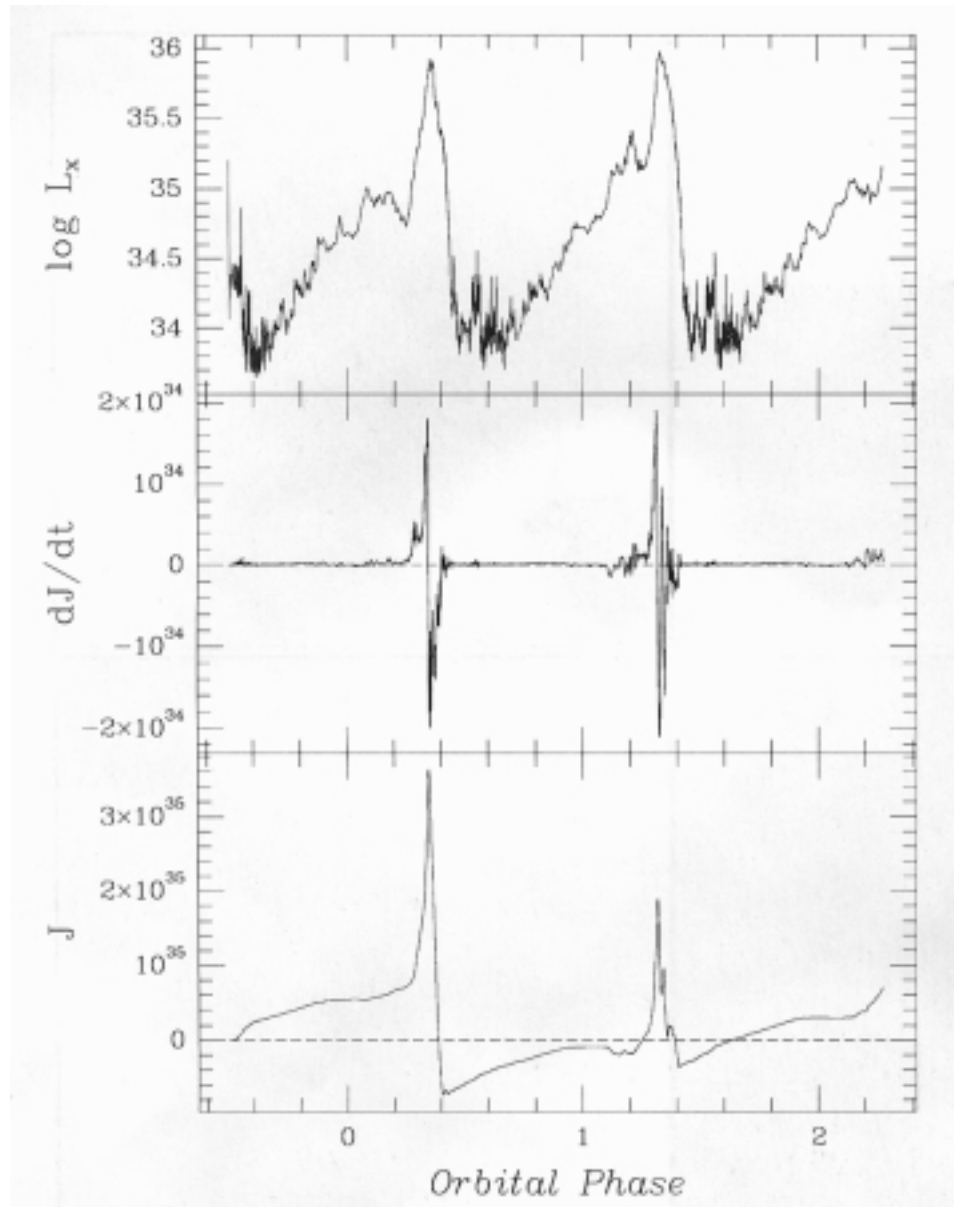


Figure 3.6: Evolution of the accretion driven X-ray luminosity (top), angular momentum accretion rate (middle), and accumulated angular momentum of the neutron star (bottom) for the fast rotator model.

the compact companion. Instead, the tidal stream approaches the accretor from behind (in the sense of orbital motion), as seen in the sequence in Figure 3.5 near periastron. This in turn leads to accretion with positive values of \dot{J} (i.e., in the same sense as the orbital angular momentum). In our fast rotator model, however, the wind can have comparable, or even more, angular velocity than the accretor during orbital phases other than periastron. As the tidally enhanced wind fades away following periastron, it also advances ahead of the neutron star, such that the net angular momentum approaching the neutron star changes sign. This process has the effect of “flushing” the material in the disk, producing a short phase of high L_x as the bulk of the gas in the transient disk is accreted on a short timescale, followed by low- L_x wind accretion.

These simulations show that tidal stripping in eccentric-orbit X-ray binaries can produce periodic X-ray flares. Such flares are characterized by a large increase in X-ray luminosity occurring substantially after periastron passage by the accreting companion star. We have confirmed the result of Boyle and Walker [1986], who found that mass tidally stripped from a star in an elliptical orbit cannot accrete onto the compact companion star unless the primary star is close to corotation at periastron. Moreover, we have demonstrated that a tidally produced gas stream from a star filling its critical lobe, in corotation at periastron, is found only after periastron passage. The assumptions of Haberl [1991] and Leahy [1991] are therefore not consistent with a tidally produced stream from the primary star.

Note that we do not consider non-equilibrium tides nor stars exceeding their critical potential lobe at periastron, both of which may modify our results. For example, one

of our first attempts at simulating this system used inappropriate boundary conditions at the stellar surface leading to substantially more mass loss at periastron, as might be the case if the star exceeded its critical potential lobe at periastron. The result was a much more massive accretion disk that remained in orbit around the neutron star for roughly half the binary orbital period, producing an extended epoch (many days) of spin up reminiscent of the spin up episodes observed in GX 301-2 by BATSE. BATSE results [Koh et al., 1997] suggest that most orbits result in zero net angular momentum accretion, as seen in our simulations presented here. The overall increase in spin rate observed since 1984 is then attributed to isolated spin-up events that occur relatively infrequently (1 out of 10 to 20 orbits). These rapid spin-up events are likely the result of a temporary accretion disk, but whether these transient disks are formed through wind accretion or through tidal stripping as in the simulations shown here is not clear.

The referee of the paper where these results were originally published has pointed out that our numerical result of no net accretion of angular momentum in tidal mass transfer has important consequences for the very fast rotation ($P = 0.069s$) observed in A 0538-66 [Mavromatakis and Haberl, 1993]. However, as described in the preceding paragraph, we believe this result is closely tied to our model assumptions. Relaxing these assumptions, *e.g.*, a primary exceeding its critical potential lobe at periastron, could conceivably lead to a net accretion of angular momentum and hence a fast rotator as in A 0538-66.

Overall, our simulations of tidal stripping do not provide an accurate quantitative match to the observed X-ray properties of GX 301-2. In particular, the tidally induced

flares seen in our numerical models are characterized by an orbital phase near 0.2, well after periastron. In contrast, the X-ray flares of GX 301-2 occur significantly before periastron with a smaller flare occurring near apastron. We see no evidence in our simulations that tidal stripping could lead to enhanced gas density in the wind that might affect accretion rates near apastron. Finally, measurements of line widths from Wray 977 suggest a rotation rate considerably slower than periastron corotation [Parkes et al., 1980], yet our results suggest that a tidally produced X-ray flare can occur only if the mass-losing star is rotating close to corotation at periastron. Our work thus suggests that a model for the X-ray flares in GX 301-2 based on enhanced wind accretion, perhaps from an equatorial disk (Pravdo et al. [1995]; Koh et al. [1997]), is more likely than one based on tidal stripping at periastron.

Although we have attempted to include a substantial amount of physics in our simulations, they remain highly idealized. Perhaps the most drastic restriction has been that of only computing flow in the orbital plane. This severely limits our ability to compute the accretion-driven X-ray luminosity, and hence the effects of this X-ray flux on the dynamics of the wind accretion process. A related limitation of our models is the relatively poor spatial resolution in the vicinity of the accretion neutron star, particularly away from periastron. These problems conspire to limit our ability to accurately model wind accretion, although this was not the focus of our investigation. Note, however, that this means this model was not adequate to address the hypothesis of Chichkov et al. [1995], who suggested that the influence of the wind-accretion driven X-rays can modify the accretion process to produce the observed X-ray light curve. Nonetheless, we believe our

primary conclusions are independent of the limitations of our model: a tidally produced X-ray flare can occur only if the mass-losing star is rotating nearly synchronously at periastron, and such a flare will occur substantially after periastron.

3.2.3 Hydrodynamic Modeling of LMC X-4

Our 3D model of LMC X-4 was initialized without an accretion disk, and the simulation was then evolved for approximately one binary orbital period. This was sufficient time for the accretion disk to circularize and for the circumstellar gas to reach a state of quasi-equilibrium. By the end of the simulation there were five key features of the circumstellar gas: a radiatively driven wind from the shadowed surface of the primary star, a wind-compressed disk created by the rapid rotation of the primary star, a tidal stream emanating from the inner Lagrange point (L1), a Keplerian accretion disk around the compact object, and an X-ray irradiation driven wind emanating from the inner regions of the accretion disk.

The radiatively driven O-star wind fills a large fraction of the binary system due to the strong shadowing effects of the accretion disk. This normal stellar wind is marked by the presence of a wind-compressed disk [Bjorkman and Cassinelli, 1993]. The density of the wind in the equatorial plane is a factor of ~ 20 higher than at other latitudes. This effect is a direct result of assuming co-rotation between the primary star and the binary system; A slower stellar rotation would diminish or remove the wind-compressed disk.

The tidal stream is described remarkably well by the analysis of Lubow and Shu

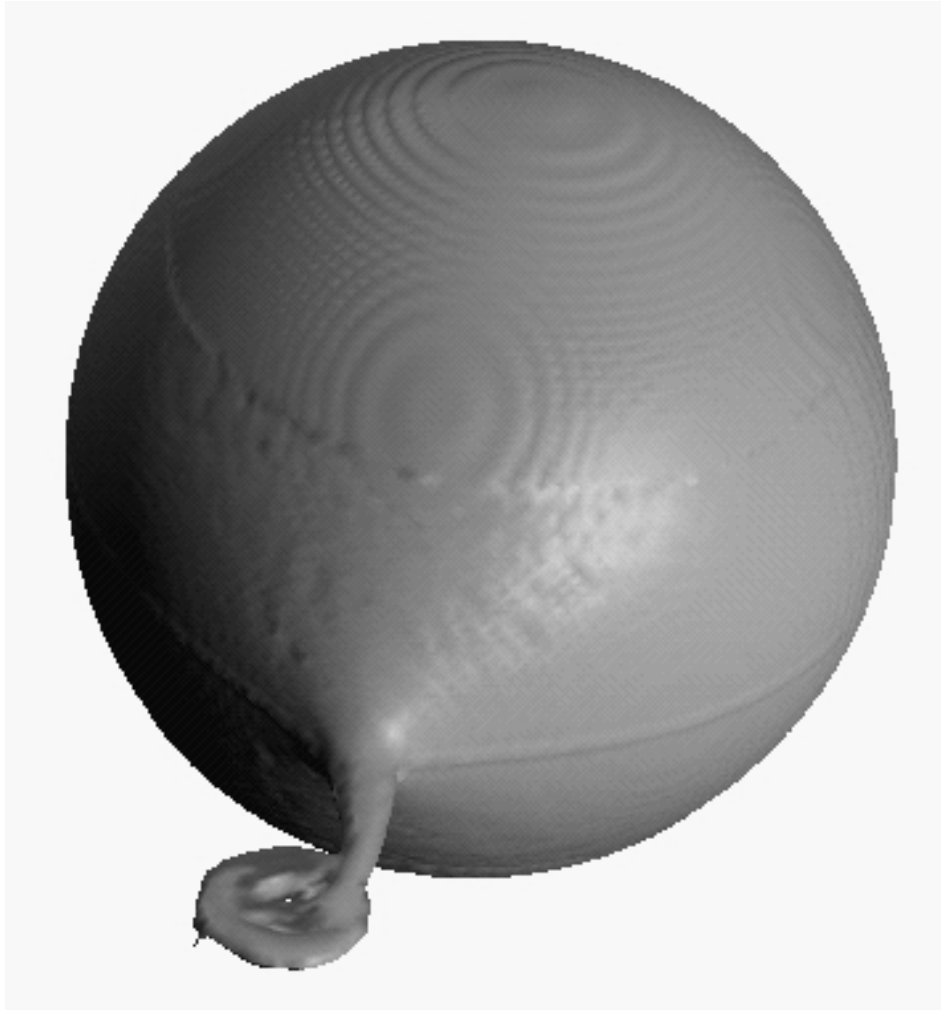


Figure 3.7: An isodensity surface of the hydrodynamic model at the end of the numerical simulation, illustrating the relative scales of the accretion disk, tidal stream and primary star.

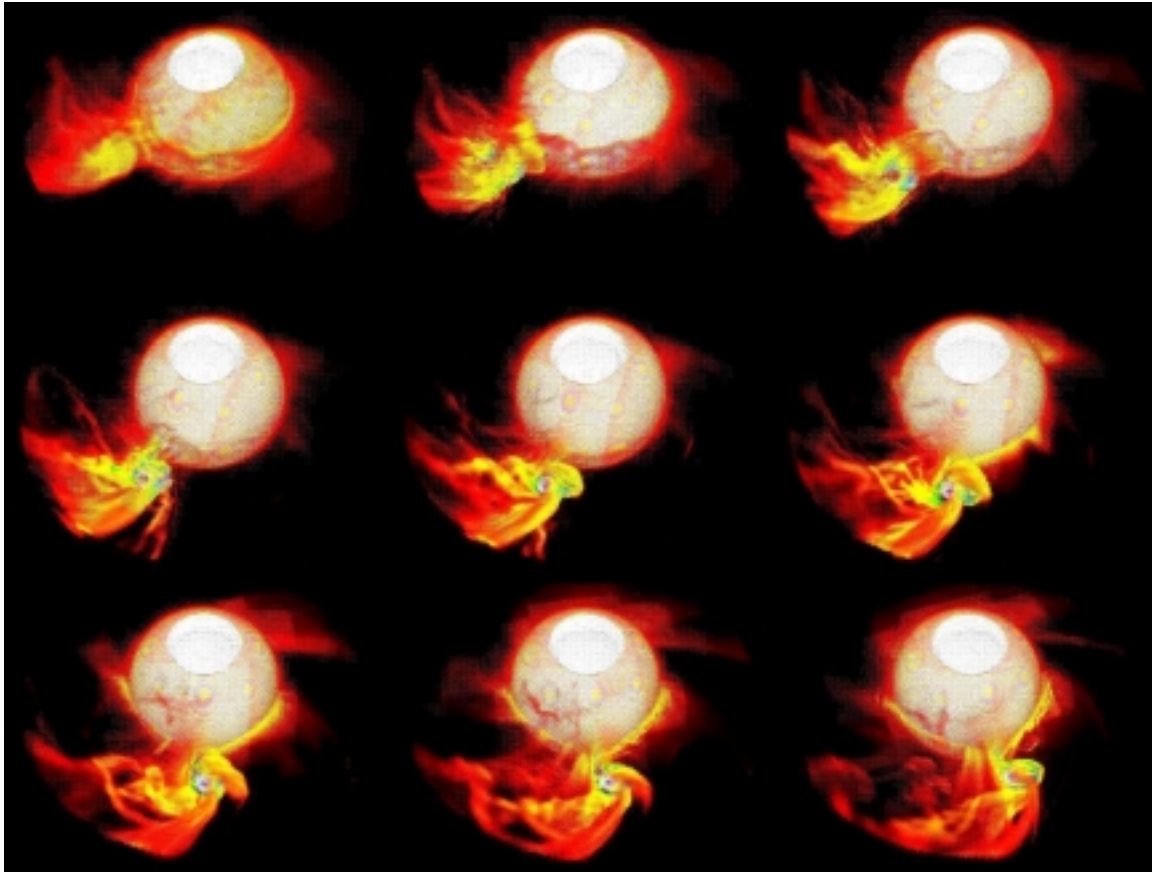


Figure 3.8: Time sequence showing the evolution of the circumstellar gas. Several features are visible, including the donor's equatorial compressed wind disk, a wake of material ablated from the accretion disk by the donor wind, and the X-ray illumination of the donor and suppression of the wind.

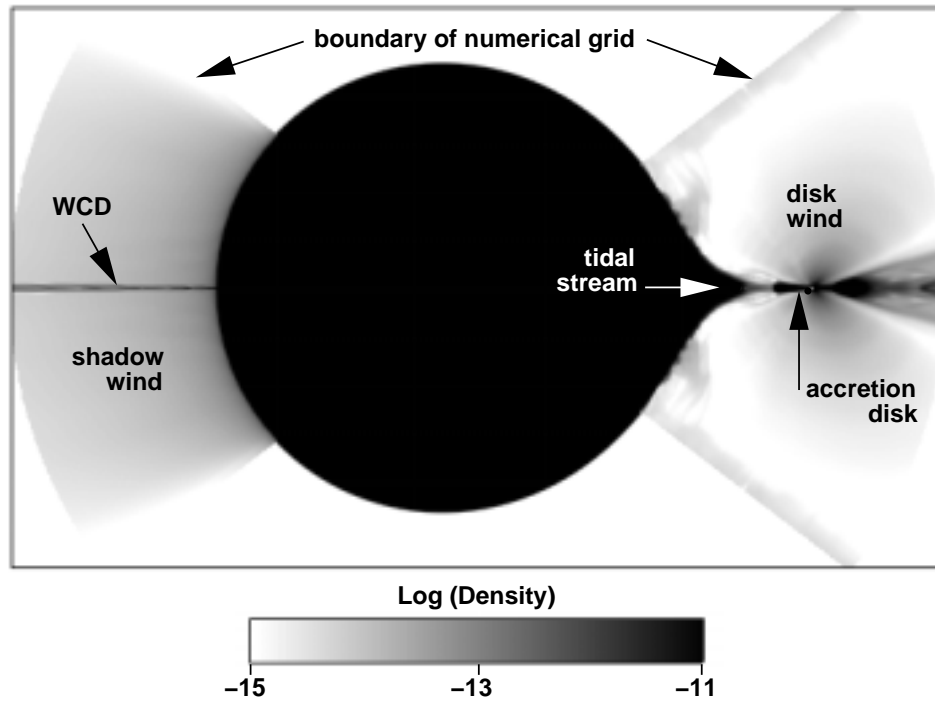


Figure 3.9: A two-dimensional slice along the line of centers of the binary system illustrating the five key components of the circumstellar gas.

[1975]. The tidal stream leaves the L1 point with an angle of $\sim 25^\circ$, in good agreement with the analytic prediction. The stream becomes supersonic only 10^{10} cm downstream, with the centroid of the stream following a ballistic trajectory until the stream impacts the disk. The gas in the stream continues to accelerate, reaching a Mach number at impact of ~ 16 .

The width of the tidal stream ($\sim 7 \times 10^{10}$ cm) is in good agreement with Lubow and Shu [1975]; 70 % of the stream mass flux is within their quoted width. The stream cross section is consistently oblate, with the stream width being about 4/3 of the stream height. As shown by Lubow and Shu [1976], the vertical structure of the stream is determined entirely by the foot points of the streamlines in the tidal stream, and hence the stream has a scale height much larger than that expected for hydrostatic equilibrium. The density in the tidal stream, and hence the mass transfer rate, is determined by the placement of the stellar surface relative to the L1 point (an arbitrary boundary condition in our model). Both the width of, and the density in, the tidal stream decrease as the stream accelerates toward the compact object.

By the end of the simulation the accretion disk has relaxed into a roughly steady-state configuration. The accretion flow has fully circularized and is nearly Keplerian, the vertical density profile matches that of an isothermal steady-state disk, and the outer radius is truncated at $\sim 8 \times 10^{10}$ cm, corresponding to $\sim 70\%$ of the Roche lobe of the compact object. Note, however, that the mass flux through the disk is not in equilibrium – even if such an equilibrium were possible in this numerical model, it would take far too long to reach.

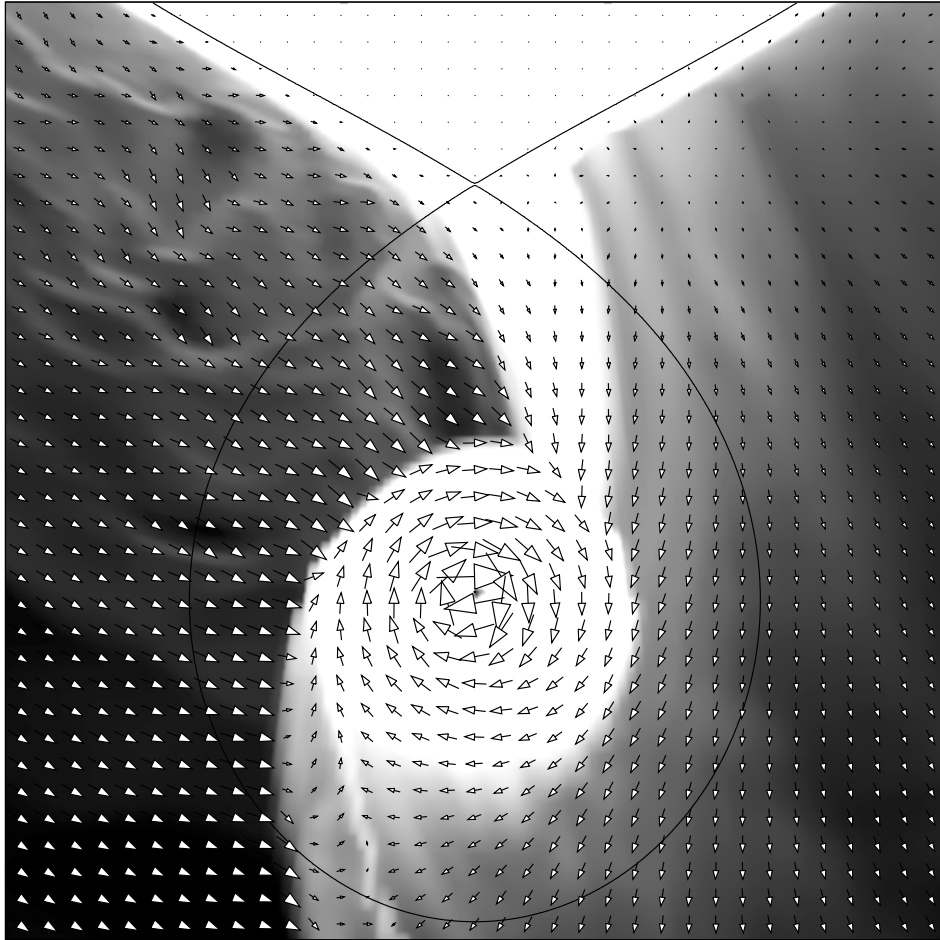


Figure 3.10: The velocity field of the circumstellar gas in the equatorial plane of the binary system. Here black represents the relatively low density of the equatorial wind, while white represents the high density of the primary star, tidal stream, and accretion disk. The solid line marks the critical potential surface.

The outer edge of the disk has a scale height of $\sim 2 \times 10^9$ cm, although the disk is somewhat thinner on the side nearest the primary star and fatter on the far side. This scale height is consistent with that of an isothermal accretion disk in steady state (the sound speed of the cold disk gas in our model is $c_s = 2.136 \times 10^6$ cm s⁻¹). The width of the tidal stream in the vicinity of the disk edge is noticeably wider, with a scale height of order $\sim 3 \times 10^9$ cm. As a result, a significant fraction of the tidal stream gas is not stopped at the disk edge, but rather flows over and under the disk along its surface. This stream overflow ultimately merges with the accretion disk in the vicinity of the point of closest approach: the location at which a ballistic trajectory from the L1 point would reach the closest to the compact companion.

In addition to the impact by the tidal stream, the outer edge of the disk is continually ablated by the strong stellar wind from the primary star. Note that this equatorial wind is enhanced by the wind compressed disk effect, and it is not directly affected by the X-ray source since it is shadowed by the accretion disk. As a result, the equatorial wind is strong enough to ablate a significant mass flux off the edge of the disk, particularly on the back side as seen in Figure 3.10. Furthermore, the ram pressure of this equatorial wind inflates the outer edge of the disk, creating a small outer rim that extends higher than the rest of the disk.

Although the outer regions of the disk are sufficiently resolved by our numerical grid, the inner regions of the disk are not. The scale height of a steady isothermal disk at a disk radius of 1.5×10^{10} cm should be $\sim 2.6 \times 10^8$ cm, but the limited resolution of our numerical model limits the disk thickness to values approximately three times larger.

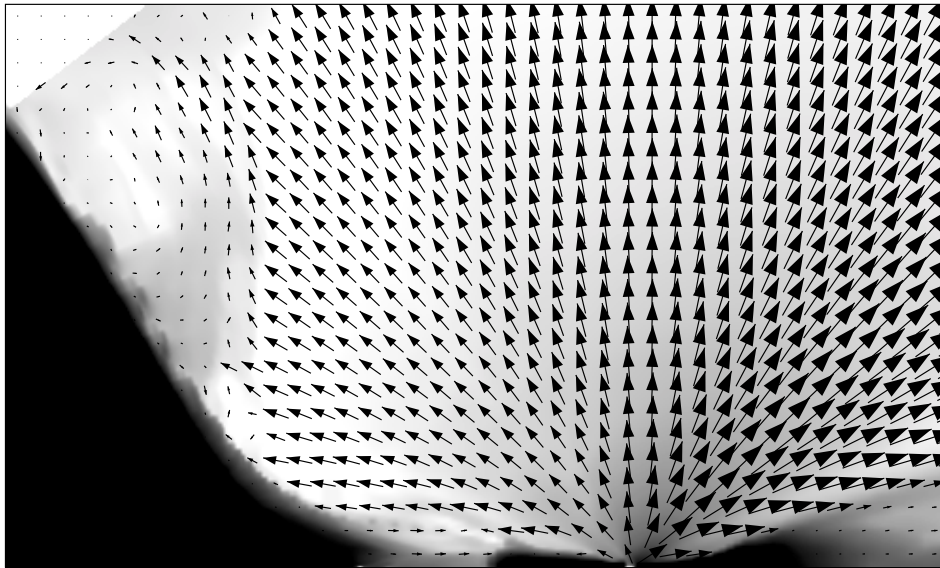


Figure 3.11: The bipolar disk wind emanating from the inner region of the accretion disk is evident in this two-dimensional slice along the line of centers of the binary system. Note that the disk wind crashes into an irradiation-driven wind off the surface of the primary star.

This limitation has direct bearing on the results of this paper in that this poor numerical resolution effectively limits (through the high opacity of the disk material) the cone of X-rays to a smaller opening angle than if the disk was adequately resolved at small disk radii.

The intense X-ray luminosity of the accreting compact companion can influence the circumstellar gas in many ways, but in this numerical model the dominant effect is a strong bipolar wind driven off the inner region of the accretion disk via X-ray irradiation. The dense, cool gas on the surface of the accretion disk is heated by the incident X-ray flux to several million Kelvins. The ensuing high thermal pressure drives a strong wind with velocities reaching 2000 km sec^{-1} . This irradiation is so intense in this numerical

model that the X-ray flux striking the inner disk edge completely ablates the inner disk, leaving a substantial hole. As seen in Figure 3.11, this disk wind is roughly spherical. This has the interesting effect of producing a large volume of X-ray heated gas with a roughly constant ionization parameter. Since both the gas density and X-ray flux are decreasing as the square of the distance from the X-ray source, the ionization parameter in this gas remains at a constant value.

Because the poor numerical resolution in the inner accretion disk affects the vertical structure of the disk, the conservation of angular momentum in the disk gas, and the thermal transition of the X-ray heated gas, the geometry and mass flux in this bipolar wind is very uncertain. Nonetheless, it is clear from both simple order of magnitude estimates and from detailed calculations [de Kool and Wickramasinghe, 1999] that the intense X-ray flux present in X-ray binaries will drive a substantial mass loss from the accretion disk.

Due to the shadowing effects of the accretion disk, the effects of X-ray photoionization are restricted to the bipolar disk wind in this model. Gas outside of the disk wind is shielded from the X-ray source, and as a result, there is no independent photoionization wake visible in this model. Instead, there is a relatively dense wake of circumstellar gas piled up along the leading surface separating the disk wind and the stellar wind. This modest wake, with a density contrast of ~ 4 , can be seen in the horizontal slices shown in Figure 3.12.

As seen in Blondin and Woo [1995], the radiatively-driven wind of the primary star is replaced by a thermally driven wind on the X-ray irradiated face of the primary.

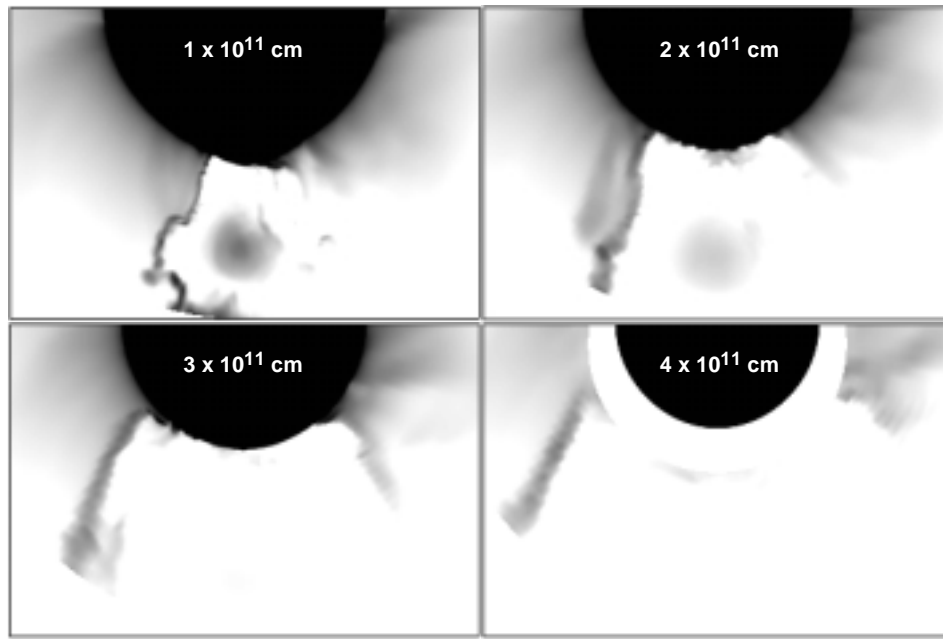


Figure 3.12: The influence of the disk wind on the circumstellar structure is seen in these two-dimensional slices parallel to the equatorial plane. The density in the leading wake (left of the disk wind) is 4 times higher than the normal stellar wind at that radius. Note that in the top slice the inner edge of the grid is beyond the surface of the primary star.

The high X-ray flux on the irradiated surface is strong enough to suppress the radiative driving force and quench the normal radiatively driven stellar wind. Instead, the X-ray flux heats the outer atmosphere of the star up to X-ray temperatures, and the ensuing high thermal pressure drives an outflow off the stellar surface. In this particular model, however, the thermally-driven stellar wind is effectively snuffed by the disk wind. The momentum in the disk wind is sufficiently high that it stops the stellar wind before it can reach a sonic point. This subsonic outflow is then redirected up over the top of the star along with the supersonic disk wind. This dynamical interaction between star and

disk winds can be seen in Figure 3.11.

Boroson et al. [2001] compared these simulations with observations of UV P Cygni lines from the GHRS and STIS spectrographs on the Hubble Space Telescope. A Monte Carlo technique was used to evaluate the UV P Cygni line profile by simulating the radiative transfer of the UV photons that are emitted from the donor's surface and scattered by the circumstellar gas. Note that the radiative transfer modeling was considerably more sophisticated than that used for the hydrodynamic modeling. The results were reassuring.

In comparison of the simulation to observations for the nitrogen N V $\lambda\lambda 1238, 1242$ and carbon C IV $\lambda\lambda 1548, 1550$ doublets observed with GHRS and STIS on board Hubble, the model spectra have errors of $\sim 5\%$ of the flux for each 60 km sec^{-1} bin and errors of $\sim 1\%$ of the flux for each 30 km sec^{-1} bin (STIS only). The simulations qualitatively reproduce the observed "Hatchett-McCray effect" (the absorption of the N V and C IV lines is reduced at phase 0.5). Some N V absorption remains at phase 0.5, in agreement with observations, owing to absorption (from collisional de-excitation) and scattering from the photosphere, as well as dense regions in the circumstellar gas that are not fully ionized by the X-rays.

The qualitative orbital variation predicted by our model is similar to observations, although the model does not produce the strong orbital asymmetry that is observed, where the observed absorption is strongest for phases > 0.5 . Our model predicts a mid-eclipse X-ray flux due to Compton scattering that is too low by a factor of 4. These data provide important feedback on our understanding of our model. It may be the

case that the mid-eclipse scattered flux is too low because our accretion disk is too thick, which may artificially constrict the X-ray illuminated portion of the wind. The numerical resolution at the center of the disk is poor; at its center the disk scale-height is much smaller than a single zone. This almost certainly artificially narrows the X-ray illuminated region. It may be the case that the lack of orbital asymmetry in the absorption is due to the constraint of the outer grid boundary, which extends out to only about $2R_*$. At high latitudes, a trailing photoionization wake forms that spirals outward on the primary wind. This wake is artificially truncated by the simulation, limiting the absorption at late phase. If the wake were allowed to propagate further out, and hence fall farther back in orbit to later phases, it could possibly account for the late phase absorption and the resulting orbital asymmetry.

Some discrepancies may arise due to the high terminal wind velocities used in the simulation (2000 km sec^{-1}), as it appears that the data are better fit by a $v_\infty = 1150 \text{ km sec}^{-1}$ wind [Boroson et al., 1999]. For example, the combination of too fast a terminal wind velocity and too small a value for r_{max} put the maximum observed velocity at the wrong phase, while absorption is predicted at too high a velocity, as well.

Random variability in the P Cygni lines was checked by using two different simulation frames separated by approximately 3300 seconds, about one Hubble orbit. The variability due to local random changes in the density and velocity fields did not exceed that which was expected, $\sim 5\%$ of the flux in each 60 km sec^{-1} wavelength bin. Hence it is safe to assume that variability of observed line profiles of $> 5\%$ from orbit to orbit are representative of real changes in the wind structure, rather than random fluctuations in

the local flow field.

Chapter 4

3D Hydrodynamic Disks

Accretion disks in close binary systems are some of the most luminous galactic objects, and are the majority of galactic X-ray point sources. Their high X-ray luminosities (both sustained and during outburst) imply high mass transfer rates onto a compact star. Conservation of the binary orbital angular momentum of gas flowing from the donor star requires that the accreting material cannot fall directly onto a compact accretor, and instead forms an accretion disk around it. One may expect a first approximation of such a disk to have a Keplerian or near-Keplerian rotation curve, to have some equilibrium, steady-state structure, to lie flat in the binary orbital plane, and to be truncated at some radius interior to the accretor's Roche lobe, with radial inflow (and consequently the liberation of gravitational potential energy) powering the observed X-ray luminosity. However, this transport through the disk remained largely inexplicable for many years, as the molecular viscosity of the gas is too low to explain the observed implied accretion rates. Typically, accretion is assumed to occur according to the α -*disk* prescription [Shakura and Sunyaev, 1973], where the origin of the viscosity remains unknown, and

is instead simply parameterized (where viscous stresses are a fraction α of the thermal pressure).

4.0.4 Local and Global Transport

In general, we expect that accretion may be driven on one of two scales: local and global. Local effects such as hydrodynamic or magnetohydrodynamic turbulence would operate anywhere within the disk where the proper conditions (whatever they may be) apply. Global effects such as large scale wave modes depend on the global structure of the disk. These global modes are of interest because they may have effects on the observable qualities of the disk, e.g. the thickness of the disk, the presence of spiral structure, and transport.

Because the disk is embedded in the binary potential, it experiences tidal forcing. This creates differential acceleration of the gas as it orbits, creating regions of increased density along the orbit. These regions steepen into shock waves that are sheared by the Keplerian motion of the disk into spirals. The shocks' equilibrium position is determined by the balance between the ram pressure ahead of them and the gas pressure behind them; i.e. the shocks are sheared by the flow until they are sufficiently oblique to lower the ram pressure to equilibrium with the gas pressure behind them. Hence at smaller radii (and higher Keplerian velocity) the shocks must become ever more oblique. The spirals become more tightly wound at smaller radii until the spirals are essentially circular and the shocks have faded away.

It has been argued that global hydrodynamic modes such as spiral shocks can drive

accretion. As the gas orbits and crosses the spiral shocks, the gas compresses and its angular velocity drops. Orbital mechanics requires that this dense, slower moving gas fall toward the accretor. As it accelerates, the flow behind the shock thins. Because the spiral is two-armed, this occurs twice per orbit for each gas parcel.

Because spiral shocks remain still (in the rotating frame) as the disk gas is repeatedly shocked, they act as a sink of angular momentum and can drive accretion. However, at smaller radii the ever increasing shock obliquity implies that the component of a gas parcel's orbital motion that is perpendicular to the shock front goes to zero. Because their efficiency at driving accretion is tied directly to their ability to dissipate orbital motion, spiral shocks become less and less efficient at the increasingly steep angles at smaller radii. Hence we expect accretion via spiral shocks to be most efficient at large radii, where both the tidal forces are the strongest, and the Mach number is the smallest. See, for example, Larson [1990].

Recently, much progress has been made in understanding the role of local magnetohydrodynamic effects such as the magneto-rotational instability, or MRI, as a mechanism for mediating angular momentum transport within the disk [Balbus and Hawley, 1998]. However, it may be the case that strong spiral shocks, such as those expected to exist due to tidal forcing in close binary stars or young planetary systems, may act to inhibit or even shut off the MRI [Winters et al., 2003].

Regardless of this, however, it may be the case that accretion via spiral shocks may dominate the outer regions of the disk. Indeed the outer disk is truncated by tidal forces that essentially tear the disk apart at large radii; by definition they dominate

at the disk's outer edge. Tidal forces and the global wave modes they excite control the dynamics of the outer disk. X-ray occultation by some regions of the disk and not others, as well as reprocessed UV light curves, indicate that the outer disk has some global, vertical structure. These questions really come down to what radii this remains true to, and what is the quantitative and qualitative nature of hydrodynamically driven transport in this regime. In light of this, it behooves us to re-examine the role of vertical structure and dynamics within such disks.

Accretion disks in close binary systems cannot be resolved, making direct observation of spiral shocks problematic (although Clampin et al. [2003] observed a protoplanetary disk being tidally forced by a companion star, showing clear spiral structure, and Maoz and McKee [1998] demonstrate that maser emission from circumnuclear disks is consistent with spiral shocks. Typically, Doppler tomograms can be constructed from spectral and time (and hence phase) dependent observations which allow us to image the disk in velocity space. We expect emission to preferentially come from areas that are both dense and hot. Spiral shocks are perfect candidates for this. Much of the gas in the disk is accumulated behind the shocks at any particular time, and the shocks are by definition dissipating energy and heating the gas. Because this emission occurs at preferred positions within the disk, and hence preferred velocity components, we should be able to observe the signature of spiral structure with a Doppler tomogram. Unfortunately the observational evidence for spiral shocks in close binary accretion disks had long been lacking. This paucity of observations is beginning to change, however. The dwarf nova IP Peg shows evidence of spiral structure during outburst (Steenhals et al. [1997], although

Ogilvie [2002] shows that the observation may also be consistent with central illumination of the tidally thickened disk surface). Morales-Rueda and Marsh [2002] use spectra of 63 CV systems during high mass transfer state to identify 24 candidates for spiral structure. 5 of these 24 are confirmed to show spiral-like structure during outburst.

Previous investigators have demonstrated the formation of sharp, two-armed spiral shocks in high-resolution 2D simulations (*e.g.* Sawada et al. [1986a], Rozyczka and Spruit [1993], Godon et al. [1998], Armitage and Murray [1998], Blondin [2000]). The vertical structure of these shock waves, as well as the effects of vertical wave modes within the disk, are of course neglected. Typically this has been done out of numerical necessity. Very fine time-resolution is required by the high orbital velocities in the disk interior, implying many thousands of cycles per orbital period. Hence high resolution three dimensional calculations have not been practical in the past. Some authors have argued that the neglect of the vertical structure is unjustified as they expect spiral structure to be weaker in a 3D disk because of the presence of additional wave modes, vertical expansion of the spiral shocks (which are artificially confined in 2D), and refraction of the spiral wave modes out of the disk [Lin et al., 1990]. All of these concerns become stronger the hotter (and hence thicker) the disk becomes. It has generally been assumed that for relatively cold, thin accretion disks the restriction to 2D is reasonable, but the high resolution 3D simulations necessary to confirm this have not been practical.

Even with these restrictions, non-negligible hydrodynamic transport within the disk has been demonstrated. Blondin [2000] found $\alpha \approx 0.1$ in the outer regions of the disk, where tidal forcing is strongest. However, he found that within the disk interior (where

tidal forces are smaller and the gravity of the accretor dominates) transport is inadequate to explain observed X-ray luminosities.

4.0.5 Effects of the Stream Impact

Shu [1976] suggests that the impact of the tidal stream may drive an accreting $m = 1$ spiral shock into the disk. However, little effort has gone into measuring the effect of the stream impact on accretion through the disk. The main difficulty has been the same as that with measuring accretion due to tidally driven spiral shocks; it is simply very difficult to accurately model and track the extremely small quantities involved ($\langle v_r \rangle / v_\phi \ll 1$). Rozyczka and Spruit [1993] simulate the gas dynamics of accretion disks including the tidal stream in 2D, and find that the main influence of the stream is to perturb the steady-state disk, rendering the flow very non-steady. 3D smoothed particle hydrodynamics simulations are unable to accurately measure transport due to either tidal effects or the stream impact [Makita et al., 2000].

4.0.6 Tilted Disks

As discussed in Chapter 1, many X-ray binaries show super-orbital periodicities. For example, Her X-1 exhibits a 35 day periodicity in X-ray flux that is attributed to periodic obscuration by a precessing, warped accretion disk [Larwood, 1998a]. The 35 day cycle has four distinct phases: the main high flux state, a low state, a shorter high state, and a final low state. This 35 day cycle is occasionally disrupted, as in extended anomalous low states (ALS), which may be due to changes in the disk warp due to variation in the

mass accretion rate [Vrtilek et al., 2001]. The normal high and low states are believed to result from varying obscuration by the precessing disk. Other XRBs exhibiting super-orbital periodicities attributable to tilted precessing disks include SS 433 (164 days), LMC X-4 (30.5 days), and SMC X-1 (55 days).

Recent observations of Her X-1, such as long term variability in the phase shift between hard and soft X-ray bands during the main high state [Ramsay et al., 2002], and X-ray spectral variation over the 35-day period [Jimenez-Garate et al., 2002], provide evidence that the disk is indeed tilted and precessing.

RXTE observations during low states show that the soft X-ray and extreme ultraviolet radiation are modulated by the binary orbital period, indicating that the flux is due to cold reflection from the companion star, with the hard X-ray source (i.e. the accreting neutron star) completely obscured (Leahy [2003]; Leahy [2002]; Still et al. [2001]). Doppler tomograms indicate that the heating of the inner face of HZ Her (Her X-1's donor star) is not symmetric; this may imply partial obscuration of the surface by the tilted disk [Vrtilek et al., 2001].

Keck II spectroscopy of mHz quasi-periodic oscillations in the light curve of Her X-1 indicates a small hot region, possibly where the ballistic stream impacts the disk, not at the disk's outer edge, but deep within the disk, in the vicinity of a tidal stream's ballistic point of closest approach [O'Brien et al., 2001] This should not be surprising; if the disk is tilted, then it is reasonable to assume that the tidal stream will only be incident upon the disk's outer edge twice per orbital period; the remaining time, the stream will impact one surface of the disk or the other.

The goals of this chapter are to extend the work of Blondin [2000] to three dimensions, to investigate the vertical structure and evolution of the disk at high resolution, to assess the effect of the tidal stream on the disk, and to assess the fluid response of a tilted disk in a tidal potential.

4.1 An Idealized Disk Model

We assume an inviscid, supersonic accretion disk with an isothermal equation of state. There is certainly no reason to believe that physical disks would not contain vertical and radial temperature gradients. However, the assumption of an isothermal gas allows for a simpler problem, by alleviating the need to model the vertical energy transport out of the disk, as well as a faster numerical solution, since there exists an analytic solution to the Riemann problem in the isothermal case rather than the usual computationally intensive iterative solution. We discuss the possible implications of non-isothermal disks for our results later.

We assume a spherical coordinate system centered on the accreting star. This provides for a naturally increasing vertical resolution within the disk at lower radius. However, since the scale height within the isothermal disk is proportional to $R^{3/2}$, the resolution of the grid fails to scale with the disk thickness, with the disk becoming less resolved vertically at smaller radii. We choose a mass ratio $q = 1$, and scale our problem such that $GM_1 = GM_2 = 1$, and the binary separation $a = 1$. In these units, $\Omega = \sqrt{1+q} = \sqrt{2}$, with orbital period $P_{orb} = 2\pi/\Omega = \sqrt{2}\pi$.

We initialize the disk with a density profile given by:

$$\rho(R, z) = \frac{\exp(-z^2/2H^2)}{R^n}, \quad (4.1)$$

where for simplicity we have written the density in the cylindrical coordinates R and z . H is the scale height of the disk assuming vertical hydrostatic equilibrium: $H^2 = c_s^2 R^3$ in our scaling. The factor of $1/R^n$ allows us to adjust the density profile as a function of radius. We examine three cases, $n = 0$, $n = 3$, and $n = 15/8$. The $n = 0$ case will be referred to as the “flat” disk, the $n = 3$ case the “steep” disk, and the $n = 15/8$ case (corresponding to the standard α -disk solution for a $\gamma = 5/3$ gas with diffusive energy transport assuming Kramer’s opacity [Frank et al., 2002]) will be called the “medium” disk.

We initialize the disk with a slightly sub-Keplerian velocity:

$$v_\phi = \sin \theta \left[r^{-\frac{1}{2}} - r\Omega \right], \quad (4.2)$$

where the factor of $\sin \theta$ accounts for the vertical gradient in the Keplerian velocity and the $-r\Omega$ term balances the Coriolis acceleration, providing for a smoother initial condition.

We truncate the disk at inner and outer radii in order to minimize the effects of boundary and initial conditions. The first ten zones of each radial column are evacuated ($r \lesssim 0.025$), and the disk is terminated at an outer radius of $r = 0.25 \approx \frac{1}{2}r_{Roche}$, slightly smaller than the tidal truncation radius of ~ 0.3 .

In the case of the tilted disk, we initialize the disk with a uniform tilt of $i = 10^\circ$, with the angle of the line of nodes ψ coincident with the binary line of centers, and the disk

gas ascending opposite the L1 point. In general, the height z above the disk of a fluid zone located at r, θ, ϕ becomes:

$$z = r[\cos \phi \sin \theta \sin \psi \sin i - \sin \phi \sin \theta \cos \psi \sin i + \cos \theta \cos i],$$

while the velocity components are:

$$u_r = 0 \tag{4.3}$$

$$u_\theta = \frac{v_k}{C} \sin i \cos(\phi - \psi) \tag{4.4}$$

$$u_\phi = \frac{v_k}{C} [\sin \theta \cos i + \cos \theta \sin i \sin(\phi - \psi)], \tag{4.5}$$

where C is given by:

$$C = \left([(\sin i \cos(\phi - \psi))^2 + [\sin \theta \cos i + \cos \theta \sin i \sin(\phi - \psi)]^2 \right)^{1/2}.$$

4.2 Computational Method

The computational domain extends radially from 0.02 to 0.4 or 0.5 (the radius of the L1 point), in polar angle from $\pi/4$ to $3\pi/4$, and azimuthally from $-\pi$ to $+\pi$. Figure 4.1 shows the extent of the computational domain. Our simulations utilize a computational grid of 256 radial by 127 polar by 127 azimuthal, or about four million zones. While the time stepping is variable, the simulation requires about 100,000 steps per binary orbit (approximately 2000 CPU hours on the IBM SP3 we utilized).

Very low density gas outside of the disk is initialized with $\vec{v} = 0$ in order to minimize the constraints on the Courant time step at the inner boundary. Boundary conditions are azimuthally periodic, with all other boundaries being constrained to allow gas to

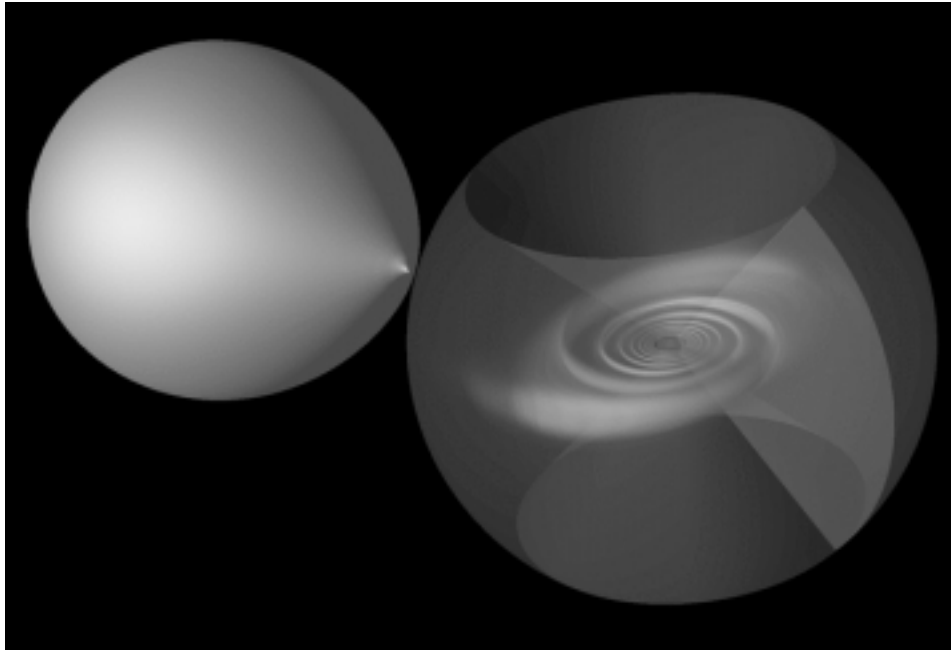


Figure 4.1: The computational domain extends from $r = 0.02$ to 0.4 , or 80% of the distance to the inner Lagrange point, from $\pi/4$ to $3\pi/4$ in polar angle, and a full 2π radians azimuthally. The companion star and tidal stream are not simulated; the equipotential surface of the companion is shown to illustrate scale only.

flow freely off the grid, but not onto it. The inner radial ghost zones are set with a pressure gradient that helps to sweep waves off the grid.

We wish to examine transport within the disk, hence we will need to define some metrics. We will follow the general literature and quantify transport in terms of an effective α viscosity of the disk. However, there are a number of ways of approaching the calculation of α . The fundamental quantity that governs accretion efficiency is the mass accretion rate through the disk as a function of radius, $\dot{M}(R)$. Following Blondin [2000] we define an α as a measure of the mass accretion rate within the disk \dot{M} :

$$\alpha_{\dot{M}} = \frac{\dot{M}v_{\phi}}{2\pi R\Sigma c_s^2}, \quad (4.6)$$

where $\dot{M} = \iint \rho v_R R d\phi dz$ and $\Sigma = \iint \rho R d\phi dz$ is the average surface density of the disk at radius R . Using azimuthal and vertical averages this definition reduces to:

$$\alpha_{\dot{M}} = -\frac{\langle v_{\phi} \rangle \langle v_r \rangle}{c_s^2}, \quad (4.7)$$

where $\langle X \rangle$ is a density weighted average of quantity X over the cylindrical surface of radius R . For computational convenience we integrate over a sphere of radius $r = R$ rather than vertically through the disk; as the disk is thin the error in this method is negligible:

$$\langle X \rangle = \frac{\iint X \rho r^2 \sin \theta d\theta d\phi}{\iint \rho r^2 \sin \theta d\theta d\phi}. \quad (4.8)$$

However, the quantity $\dot{M}v_{\phi}$ can be averaged in more than one way. Therefore we will also calculate an α based on the radial flux of angular momentum, $\rho r v_{\phi} v_r$, which reduces to:

$$\alpha_L = -\frac{\langle v_{\phi} v_r \rangle}{c_s^2}. \quad (4.9)$$

Following Shakura and Sunyaev [1973], Balbus and Hawley [1998] suggest that the α for hydrodynamic transport is given by the spatial average of the $R\phi$ component of the Reynolds stress $W_{R\phi}$, the correlation between deviations in v_ϕ and v_r :

$$\alpha_{W_{R\phi}} = \frac{\langle \delta v_\phi v_r \rangle}{c_s^2}, \quad (4.10)$$

where $\delta v_\phi = v_\phi - \langle v_\phi \rangle$. Note the interesting result that $\alpha_{W_{R\phi}} = \frac{1}{c_s^2} \langle (v_\phi - \langle v_\phi \rangle) v_r \rangle = \frac{1}{c_s^2} (\langle v_\phi v_r \rangle - \langle v_\phi \rangle \langle v_r \rangle) = \alpha_M - \alpha_L$.

In the case of the tilted disks, we need to measure the tilt and precession of the disk. We integrate to find the total angular momentum vector of the fluid contained within a shell of constant radius for each radial coordinate. The tilt angle and line of nodes are then found from the angular momentum vector.

$$\ell_x = -r \langle u_\phi \cos \theta \cos \phi + u_\theta \sin \phi \rangle \quad (4.11)$$

$$\ell_y = r \langle u_\theta \cos \phi - u_\phi \cos \theta \sin \phi \rangle \quad (4.12)$$

$$\ell_z = r \langle u_\phi \sin \theta \rangle \quad (4.13)$$

$$i = \tan^{-1} \left(\frac{\sqrt{\ell_x^2 + \ell_y^2}}{\ell_z} \right) \quad (4.14)$$

$$\psi = \tan_2^{-1}(\ell_x, \ell_y) \quad (4.15)$$

where the function \tan_2^{-1} returns a value between $-\pi$ and π in the correct quadrant.

4.3 Numerical Simulations

We take our standard model to be the $n = 0$ flat disk. The Mach number within the disk varies from ≈ 6.6 at the tidal truncation radius to ≈ 23 at the inner disk edge. Initial

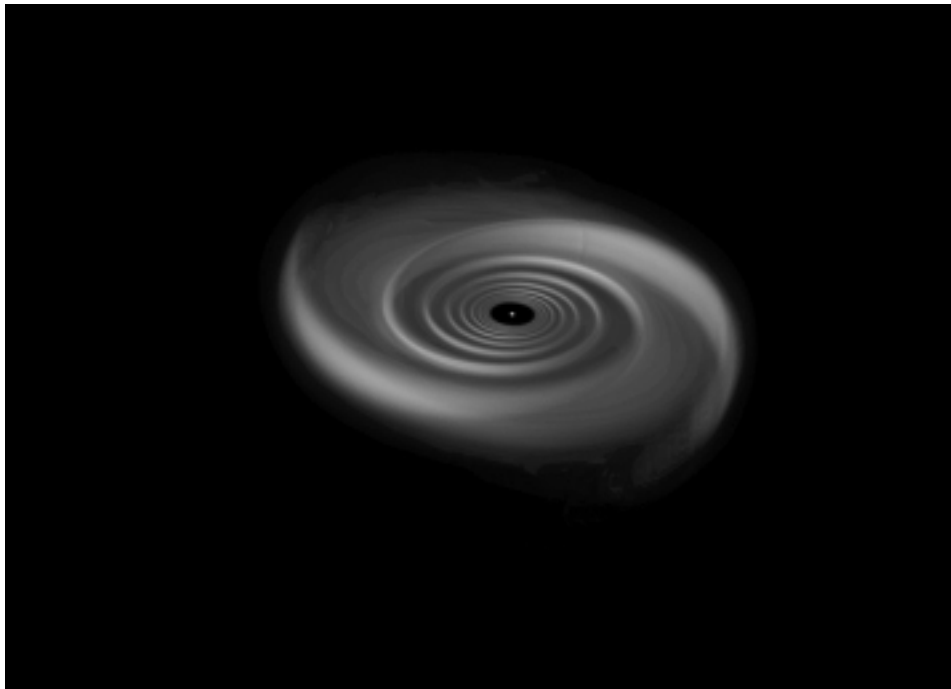


Figure 4.2: Tidally driven spiral waves in the disk.

transient waves exit the system rapidly, and strong spiral shocks, as shown in Figures 4.2 and 4.3, form within a time $t \approx 0.2P_{orb}$. The average density and scale height of the disk as a function of radius match theoretical expectations well. The spiral shock angles agree well with theory and 2D simulations [Blondin, 2000].

4.3.1 Vertical Shock Structure and Dynamics

As the spiral shocks form at the beginning of the simulation, they do not form straight, vertical planar shocks. Rather they are concave, inward facing ribbons, as in the third frame of Figure 4.5. As the shock jumps continue to steepen, the inward facing concavity deepens, until a point is reached where the vertical pressure support condition is violated,

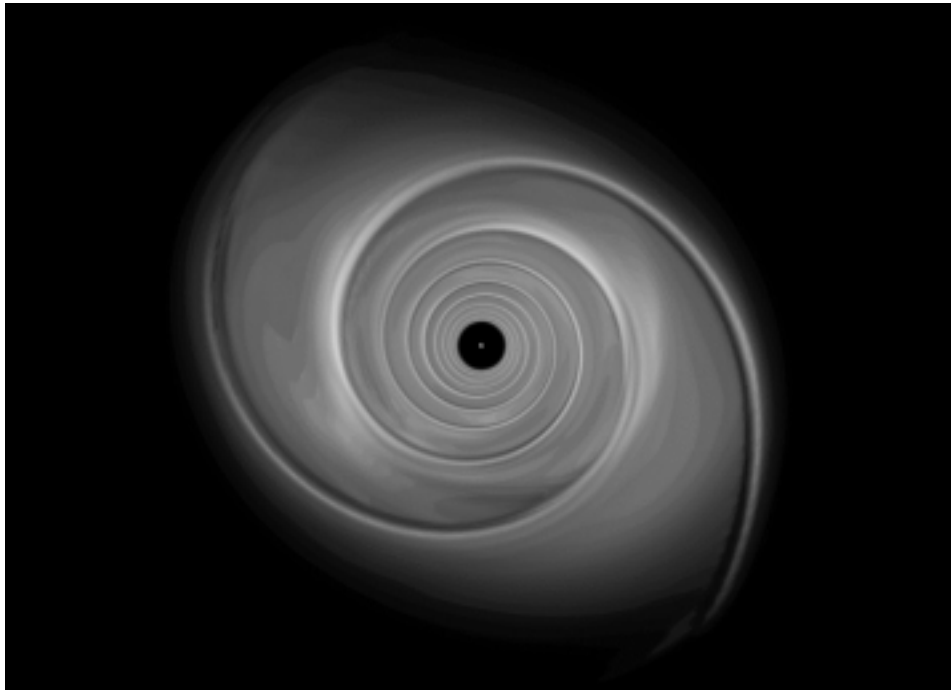


Figure 4.3: The disk at early time. The spiral shocks are strong and crisp, and in excellent agreement with theory and 2D.

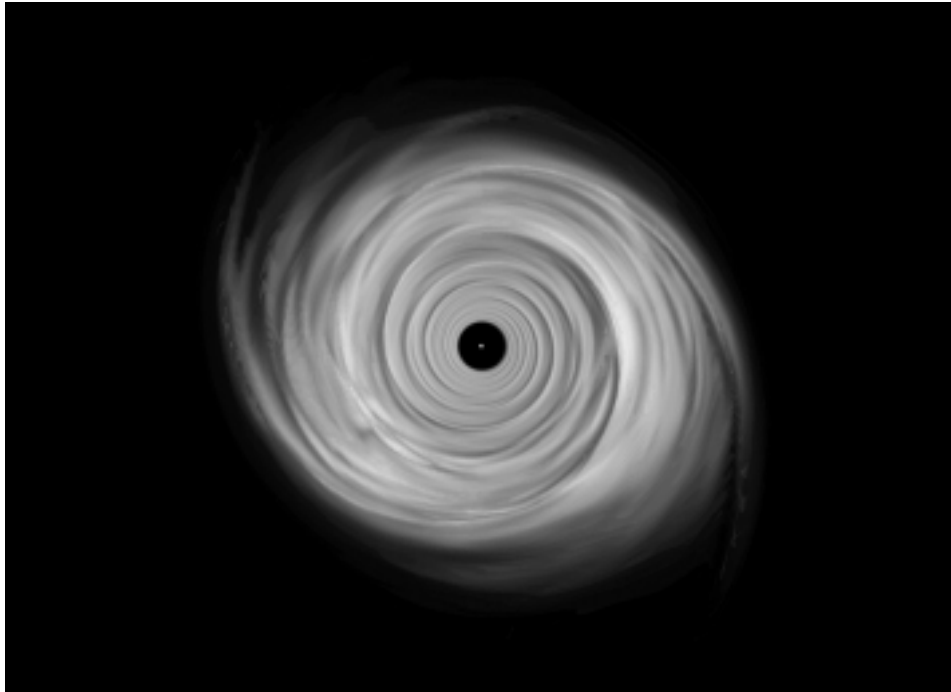


Figure 4.4: The disk at late time. Note the many waves modes traveling between the spiral shocks, as well as the decrease in the over-density of the shocks as compared with the rest of the disk.

and the shocks fall back toward the orbital plane (see the middle frames of Figure 4.5). As it falls toward the plane, this gas steepens into vertically traveling shock waves in the disk between the spiral shocks (see the latter half of the frames from Figure 4.5). The end result (by $0.5P_{\text{orb}}$) is that a) the spiral shocks are “smeared out,” i.e. the ratio of the average gas density within the spiral shocks to the average gas density between them is lowered, b) the disk is “noisy,” i.e. there are many wave modes other than the spiral shocks traveling through the disk (see Figure 4.4). Symmetry about the orbital plane is broken, and there are large scale vertical motions within the disk, including a slight tilt ($\approx 1^\circ$) at the inner disk edge (at times later than approximately P_{orb}), as well

as the previously mentioned vertically traveling shocks between the spirals.

In order to explain this striking behavior, we note that spiral shock waves within the disk are unstable to vertical ram pressure gradients within the disk. Consider a parcel of gas at some distance above the plane. The vertical component of the accretor's gravity is balanced by hydrostatic equilibrium, hence the centrifugal acceleration of the gas parcel need only balance the cylindrical radial component of the accretor's gravity. Furthermore, the gas parcel's distance to the accretor is slightly larger than that of a parcel below it in the plane. Hence we expect there to be a vertical gradient in the equilibrium Keplerian velocity of the gas. The equilibrium position of the spiral shocks is determined by the balance of the ram pressure entering the shock and the gas pressure behind it. At some altitude above the binary orbital plane, the lower Keplerian velocity ahead of the shock lowers the ram pressure. This ram pressure deficit allows the gas pressure behind the shock to equilibrate by displacing the shock front forward (toward the oncoming flow). Because the Keplerian velocity near the plane is proportional to $\sin^{3/2} \theta$, the ram pressure is proportional to $\sin^3 \theta$, and the forward displacement of the shock should become greater at higher altitude.

A back-of-the-envelope calculation shows that the inward deflection of the shock from this mechanism is of order z^2/R^2 , inadequate to explain the behavior of our simulations. However, once the shock front is slightly curved due to the mechanism outlined above, the shock becomes more oblique, which lowers the ram pressure, which displaces the shock forward, which makes the shock more oblique, which lowers the ram pressure, etc., until the shock becomes so bowed inward that the vertical gas pressure gradient is

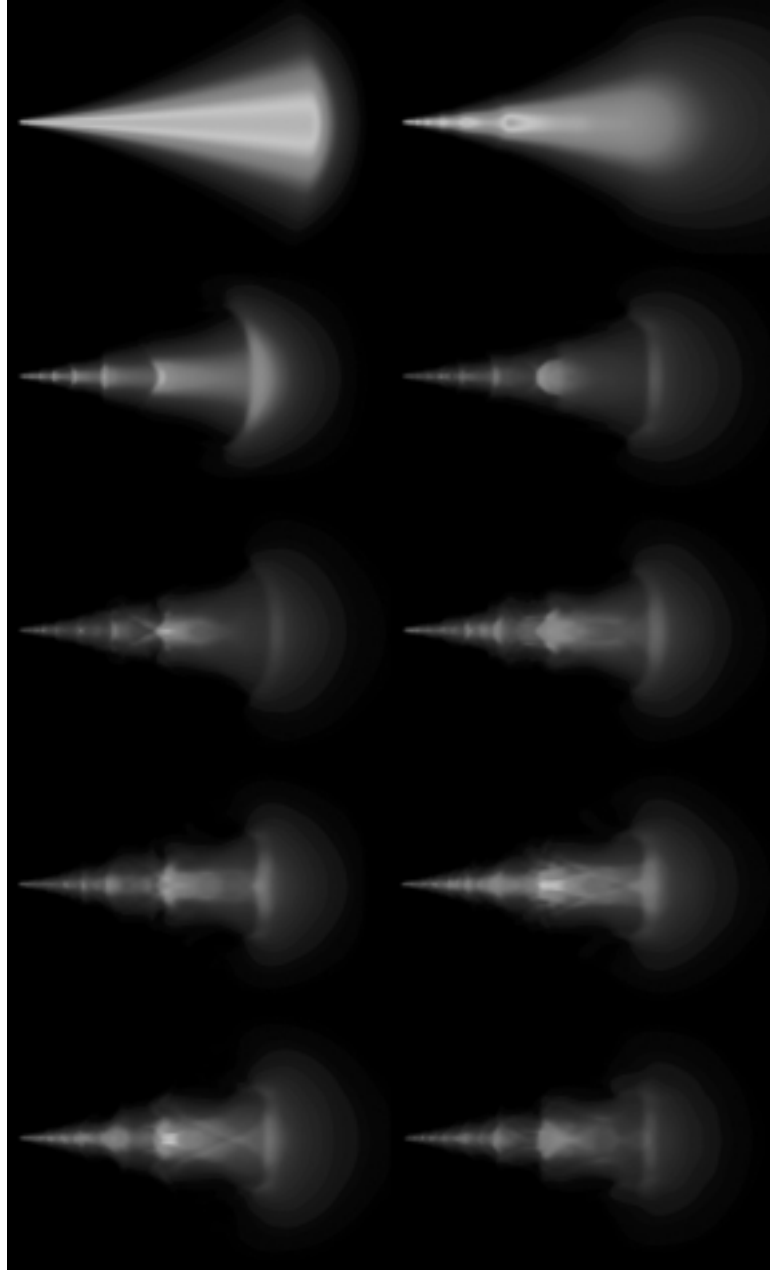


Figure 4.5: The tidally driven spiral shocks form concave inward, deepening until they collapse downward due to the loss of vertical pressure support. This creates vertically traveling shocks between the spirals. The time sequence is from left to right, top to bottom, and covers a time of approximately $0.5P_{orb}$.

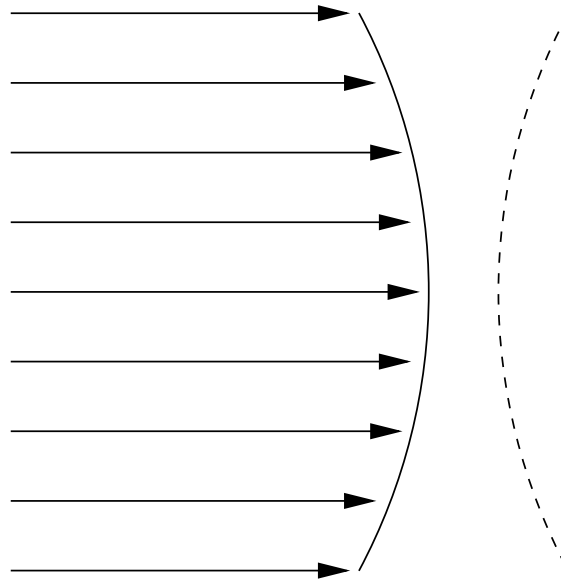


Figure 4.6: The seed of the ram pressure gradient instability. The incoming ram pressure and the gas pressure behind the shock are both dependent on the gas density, which varies vertically by the same factor both ahead of and behind the shock, $\exp(-\frac{z^2}{2H^2})$. The incoming ram pressure varies vertically as $v^2 \propto \sin^3 \theta$. The ram pressure deficit allows the gas pressure behind the shock to equilibrate by displacing the shock forward by an amount that increases with altitude above and below the disk. This steepens the shock angle, again dropping the incoming ram pressure, which exacerbates the situation until the shock collapses vertically.

inverted, and the vertical structure of the spiral shock, no longer supported, collapses down into the plane. This gas steepens into vertically traveling shocks between the positions of the spiral shocks in the orbital plane.

4.3.2 Tidal Bulging of the Outer Disk

Differential vertical tidal forcing around the rim leads to vertical thickening of the disk. Our simulation produces results that are similar to those of Ogilvie [2002], who used a semi-analytical model of non-linear tidal distortions to demonstrate tidal thickening in the outer disk. As gas orbits in the disk, it experiences vertical tidal forcing, which we may expect to generate vertical motions of the gas. For radii where tidal forcing is resonant with a natural oscillatory mode of the disk, we may expect the construction of large vertical resonant waves within the disk. For mass ratios near unity, the $m = 2$ vertical tidal resonance is within the tidal truncation radius (Ogilvie [2002]), and hence we may expect to find $m = 2$ tidal thickening of the outer disk.

We find that the scale height of the disk is alternately thickened and thinned by as much as 30-40% in two limbs in the outer third of the disk. The thickened limbs are centered at phases approximately $\frac{1}{8}$ and $\frac{5}{8}$ before mid-eclipse, and display spiral-like structure due to the shearing of the $m = 2$ wave mode. Ogilvie states that observation of spiral-like structure in accretion disks may thus be consistent with illumination of a tidally bulged disk rather than the presence of spiral shocks. However, our simulations show that this tidal thickening of the scale height is concomitant with the positioning of the actual spiral shocks; the shocks' over-density in comparison to the disk increases the

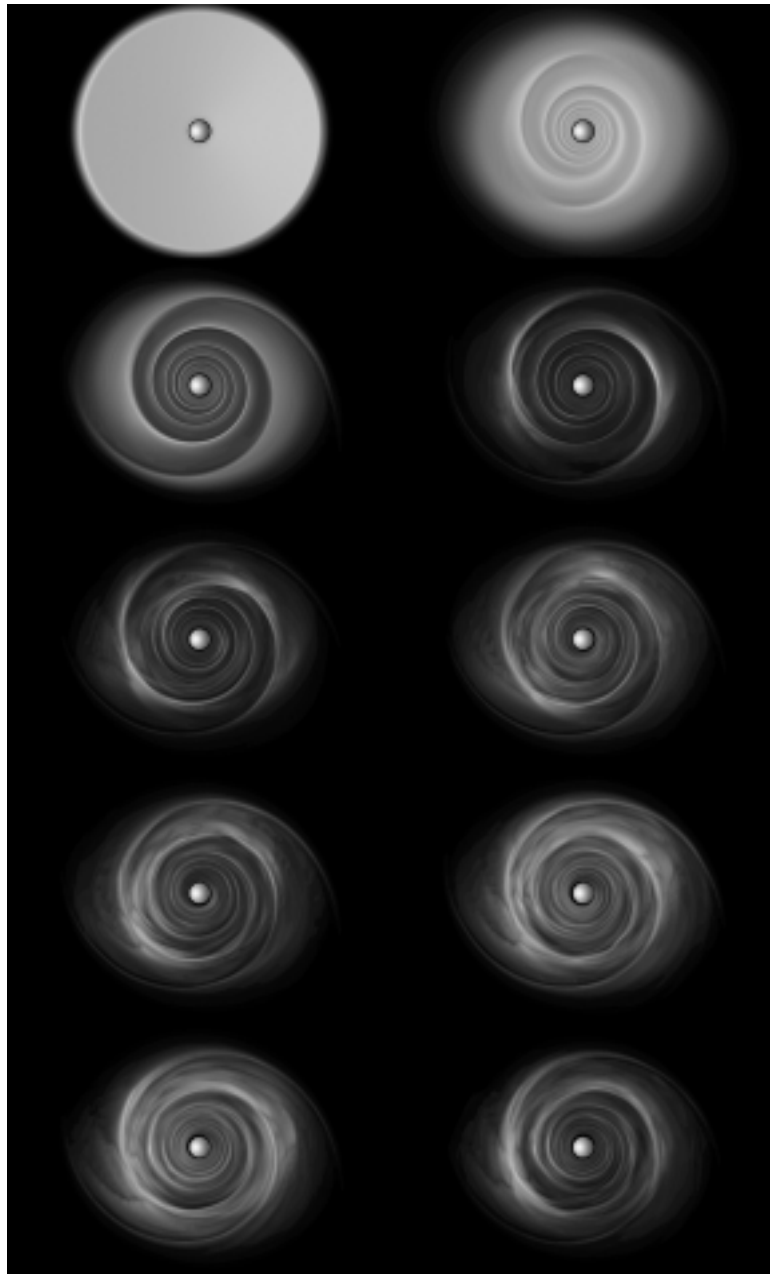


Figure 4.7: The evolution of the $n = 0$ disk until approximately $0.5P_{orb}$. Note the decreasing signal-to-noise ratio of the spiral shocks, the increase in intra-shock wave modes, and the tendency of the two-armed spiral to become one-armed.

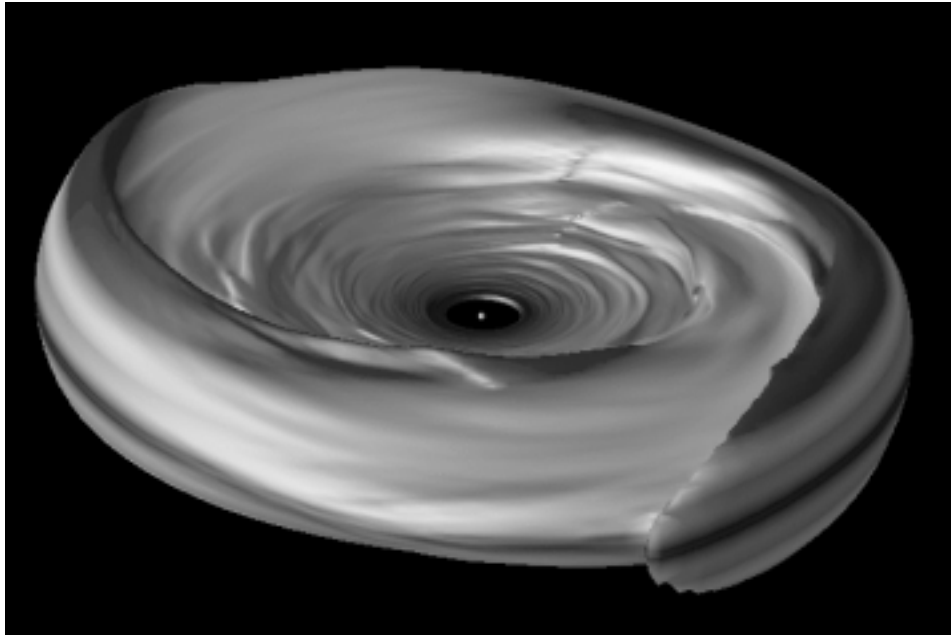


Figure 4.8: A density isosurface of the disk, shaded by altitude above and below the plane, indicating the regions where tidal bulging and spiral structure combine to increase the disk height. Because both effects exaggerate the concavity of the disk in these regions, we may expect preferential illumination and reprocessing of X-rays from the accretor there.

outer disk's actual thickness at precisely the same phases. Hence it may be problematic to attempt to assign observational evidence of spiral-like structure to one effect or the other; it is likely that both mechanisms are operating (see Figure 4.8).

4.3.3 Epicyclic Motions

The flat density profile simulation showed strong epicyclic motions near the center of the disk, with the development of an $m = 1$ mode (Figure 4.9). As in the 2D simulations of Blondin [2000] and Godon [1997], a one-armed spiral wave develops near the center of the disk, while the two-armed spiral structure remains strong in the outer regions of the

disk. Orbits near the accretor are off-set and precess with a frequency of approximately four times the binary orbital frequency, which is the gas orbital frequency of the outer disk.

4.3.4 $n = 3$ and $n = 15/8$

The density profile of the disk had little effect on the results presented to this point. All three cases show the same susceptibility to the vertical instability of the spiral shocks, as well as tidal thickening in the disk rim. The exception to this is the large scale epicyclic motion of the $n = 0$ disk, which is absent from the two steeper disks (although all three disks show evidence of epicyclic motions in $\alpha(r, t)$; see the next section).

We postulate that the $n = 0$ disk is more susceptible to resonant driving of the inner disk. The mass contained in successive annuli of the flat disk increases with radius; thus there is more inertia in the outer, heavy annuli, experiencing larger tidal torques, to move the lighter inner annuli, yielding significant off-set and precession of the inner disk and the formation of the one-armed spiral pattern. In the steeper density profile disks, it is difficult for the lighter outer annuli to displace the heavier inner disk and epicyclic motions remain small at small radii. This also explains why the epicyclic motions of the inner disk occur at the gas orbital frequency of the outer disk, since that is the region driving them.

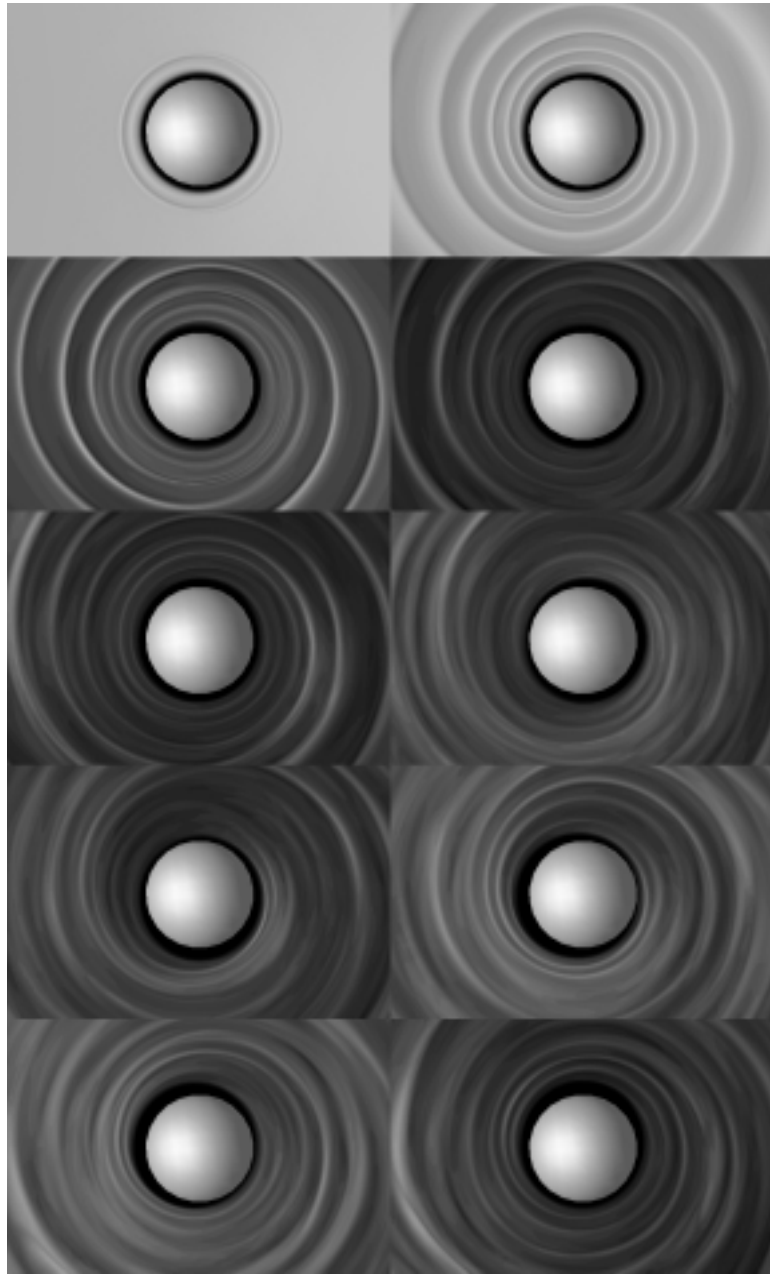


Figure 4.9: The evolution of the flat density profile disk at small radii. The sphere is the inner edge of the computational domain. Note the epicyclic motions of the inner disk edge and the formation of the $m = 1$ one-armed mode.

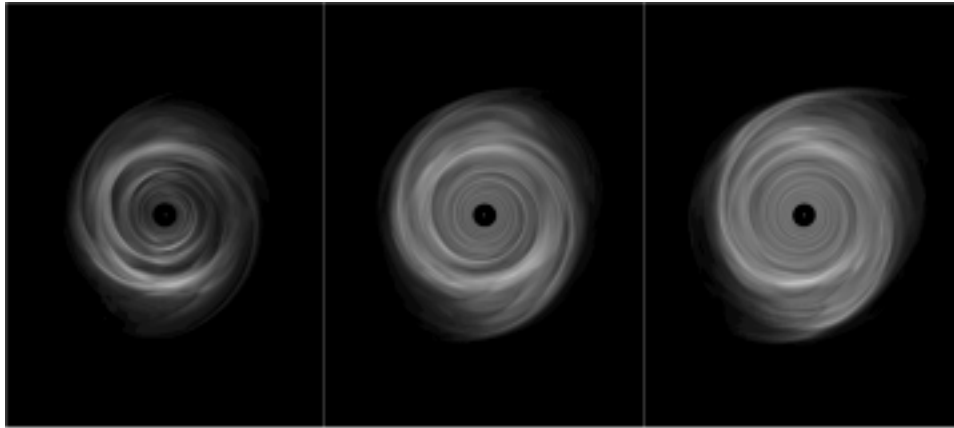


Figure 4.10: Scaled by a factor of r^n , the $n = 0$, $n = 1.875$, and $n = 3$ disks at late time. Except for the epicyclic motions of the $n = 0$ disk, all three disks behave in a qualitatively similar fashion.

4.4 Transport

Since $\alpha_{\dot{M}}$ and α_L essentially represent two methods for averaging the same quantity, we expect them to be similar and indeed they are, diverging significantly only in the outer portions of the disk where v_r and δv_ϕ become highly correlated by large scale tidal forcing. Hence, even when significant angular momentum transport and mass accretion are taking place, by definition $\alpha_{W_{R\phi}}$ remains small.

Both measures of α become large and negative beyond the tidal truncation radius, as one would intuit. They peak at around $r = 0.2$ at $\alpha \approx 0.1$ – 0.15 , decreasing with increasing density steepness of the disk. Between radii of one third and one half the disk radius, α drops rapidly with increasing disk steepness, from ≈ 0.03 for the $n = 0$ flat disk to an order of magnitude smaller for the $n = 3$ steepest disk. It should be noted that although vertical resolution is poor at such small radii, the spiral shocks are well

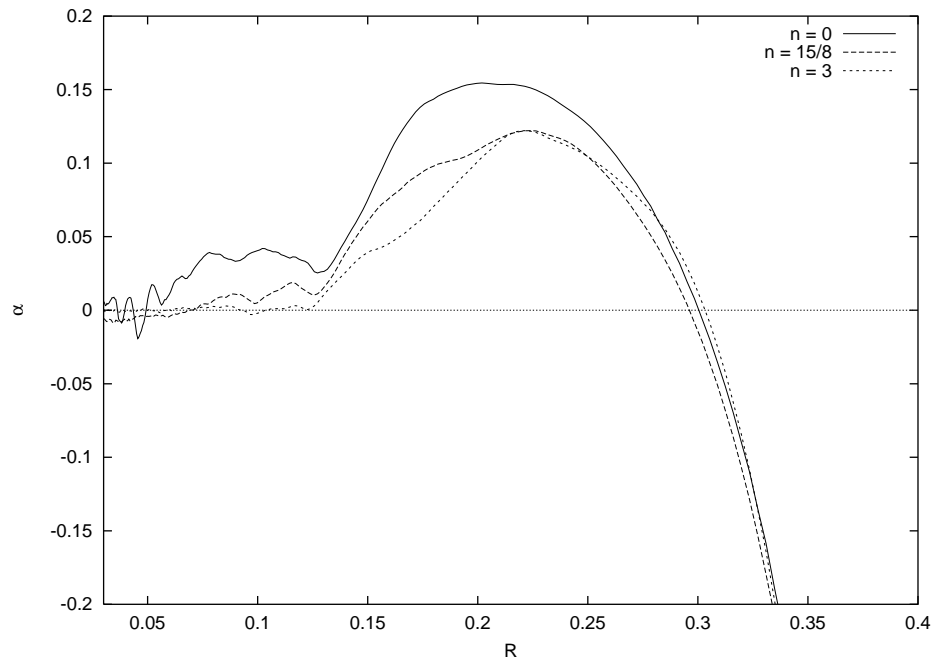


Figure 4.11: α_M for all density profiles, averaged over approximately one orbital period.

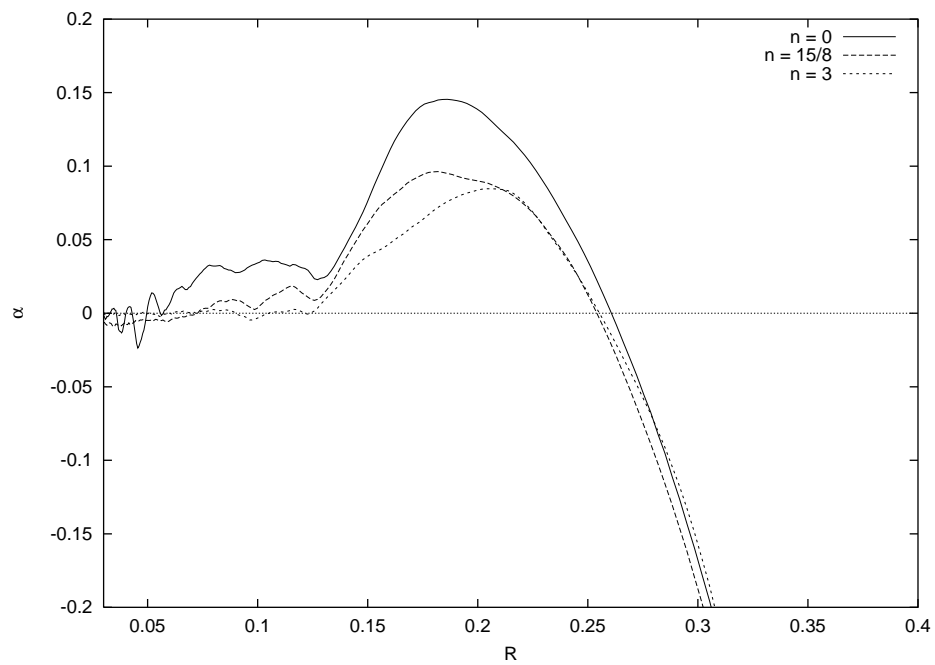


Figure 4.12: α_L for all density profiles, averaged over approximately one orbital period.

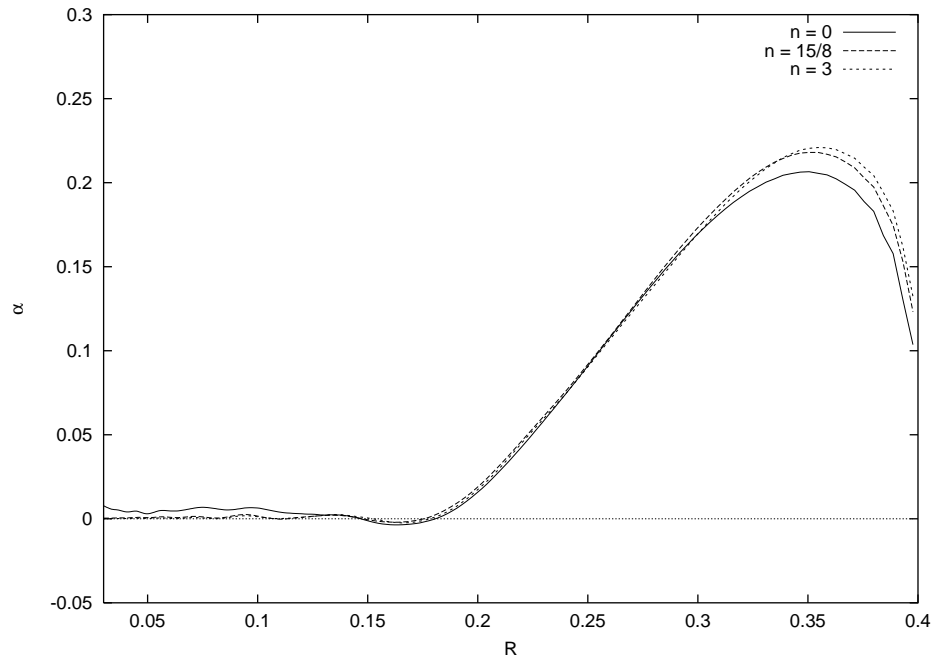


Figure 4.13: $\alpha_{W_{R\phi}}$ for all density profiles, averaged over approximately one orbital period. Note that $\alpha_{W_{R\phi}}$ only becomes large external to the disk, where tidal forces are shearing the disk apart and truncating it.

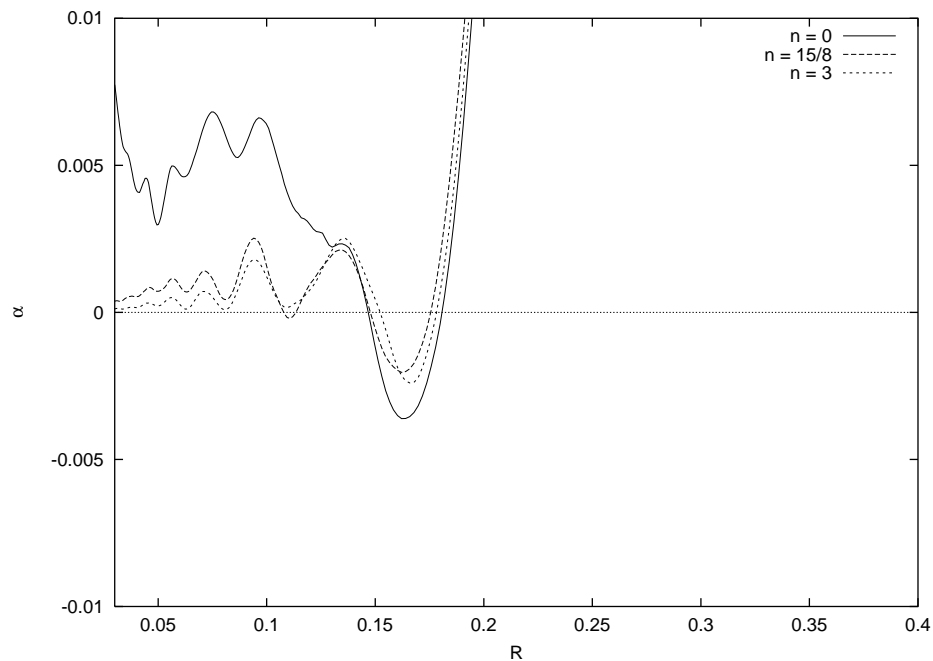


Figure 4.14: Close-up of $\alpha_{W_{R\phi}}$

resolved radially, and that many Keplerian orbits were averaged. However, due to the epicyclic motions (driven at much lower frequency) and the limitations of computational time, the values of α within a radius smaller than about one third of the disk radius for the $n = 0$ and $n = 15/8$ cases have not converged. Figure 4.15 shows $\alpha_M(R, t)$ over the period $t = 1.25P_{orb}$ to $1.5P_{orb}$ for the steep disk. In this case α remains small at small radii, though oscillatory. Figure 4.16 shows the large swings in α due to epicyclic driving at smaller radii for the flat disk.

Interestingly, $\alpha(r, t)$ exhibits “period doubling” behavior, where radial bands within the disk transport mass in steady synchronization at resonant orbital frequencies, interspersed with radial bands of unsteady transport until the flow steadies in the next resonance. The tidal truncation radius occurs at $\Omega/\Omega_{orb} = 4$, the peak in α occurs at $\Omega/\Omega_{orb} = 8$, and coherent resonant bands of transport occur at $\Omega/\Omega_{orb} = 16, 32, 64, 128, \text{ and } 256$. This may lead to banding of the disk interior at late time as $\alpha(R)$ may not be monotonic. However we simply cannot say at this point, as our disks have not evolved long enough for α to converge at small radii. We hope to extend the simulation time by at least an order of magnitude in future work.

4.4.1 Tidal Stream

After initial transients had exited ($t \sim 0.2P_{orb}$), we turned on mass transfer in the $n = 0$ disk via a tidal stream. The tidal stream was injected at the L1 point at the sound speed $c_s = 0.25$ with zero azimuthal velocity. The stream has a density profile at the edge of

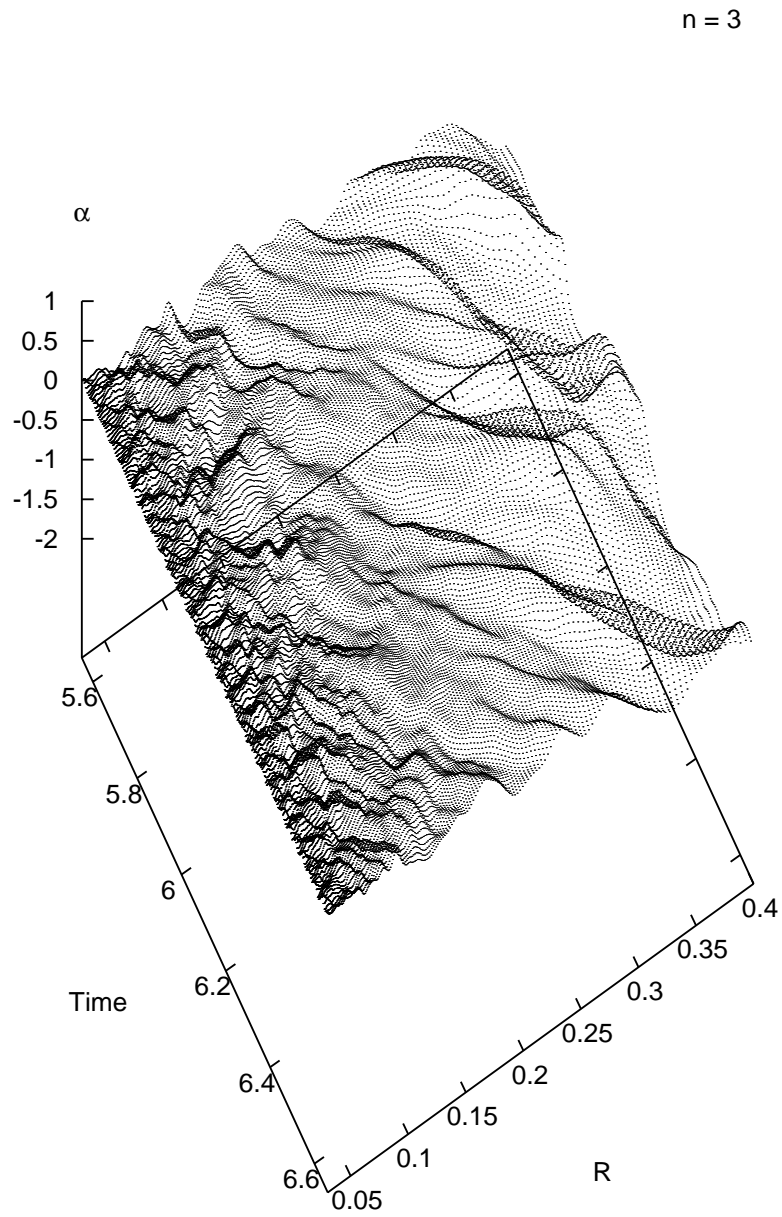


Figure 4.15: $\alpha_M(R, t)$ for $n = 3$. Oscillations in α remain small.

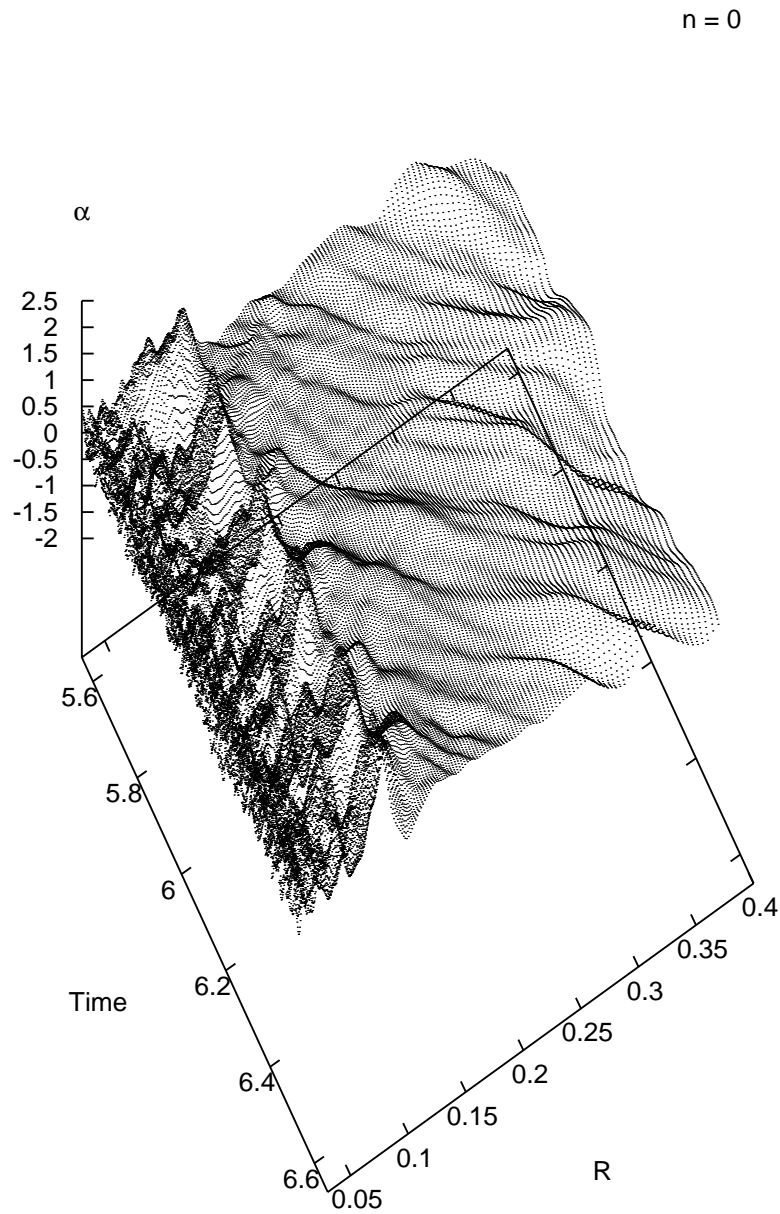


Figure 4.16: $\alpha_M(R, t)$ for $n = 0$. Note the large variation in α in the interior, due to epicyclic motions of the disk. The significance of the outward traveling waves in α , which travel at slightly supersonic speed ($v \approx 1.4c_s$) is unclear, although they may reflect the outward transport of mass and angular momentum.

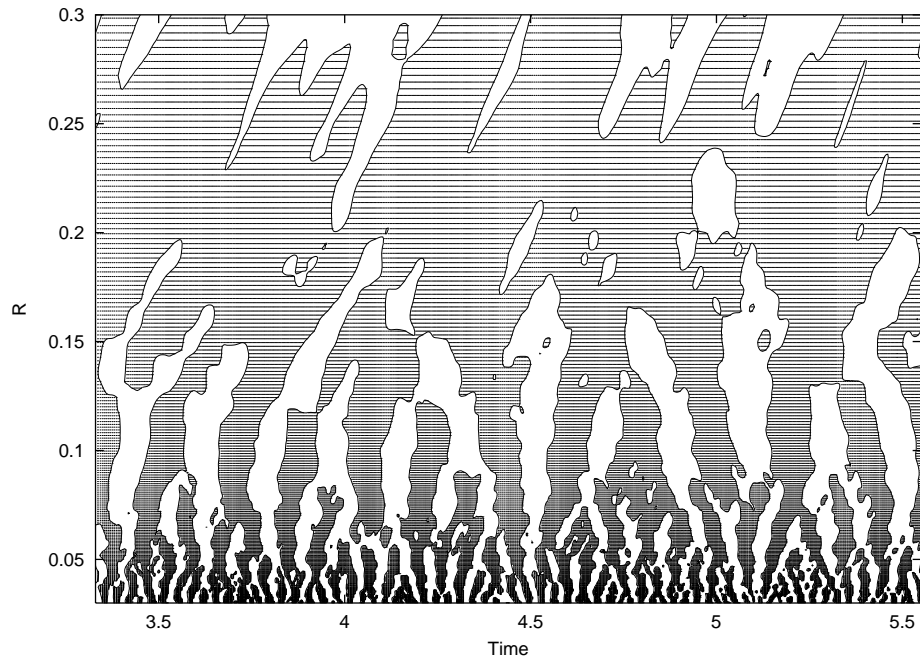


Figure 4.17: Contour of $\alpha_{\dot{M}} = 0$ for the $n = 0$ case. The shaded regions are where $\alpha_{\dot{M}} > 0$. The time axis extends from $t = 0.75P_{orb} - 1.25P_{orb}$. Note the radial banding, indicating synchronous transport around resonances with the orbital period.

the grid given by:

$$\rho = \rho_0 e^{-r/r_s}, \quad (4.16)$$

where r represents the radial position from the stream center, and r_s is a scale factor of the stream, here chosen to be 0.02. The stream is truncated radially at $2r_s$. The density of the stream was chosen to approximately match the mass transfer rate to the mass accretion rate through the disk:

$$\dot{M}_{\text{stream}} = 2\pi\rho_{0\text{stream}}c_s \int_0^{2r_s} r e^{-r/r_s} dr = \dot{M}_{\text{disk}} = 3\pi\alpha c_s H \Sigma.$$

Substituting $\Sigma = 2\pi R H \rho_{0\text{disk}}$ and $H^2 = c_s^2 R^3$, we find:

$$\rho_{0\text{stream}} \approx \frac{5\pi\alpha c_s^2 R^{5/2}}{r_s^2} \rho_{0\text{disk}}.$$

Since α varies with radius within the disk, this choice is necessarily somewhat arbitrary; we choose $\rho_{0\text{stream}} = \rho_{0\text{disk}}$, appropriate for the disk interior.

We note that Equation 4.16 is in error. The density profile of the stream is known to be Gaussian, rather than exponential. However, as this mistake was not discovered until after our simulation runs had been made, the following results include the miscalculation. We note that the net mass and angular momentum carried by the stream remains unchanged, however the particular injection profile into the disk may be altered.

As one might expect, Figure 4.18 shows that the density of outer disk increases with the tidal stream turned on. The density within the inner disk is also increasing over time. One might expect this is from the 3D nature of the problem; some fraction of the stream gas might overflow the surface of the disk and be injected near the center of the disk at the stream's point of ballistic closest approach, rather than simply being

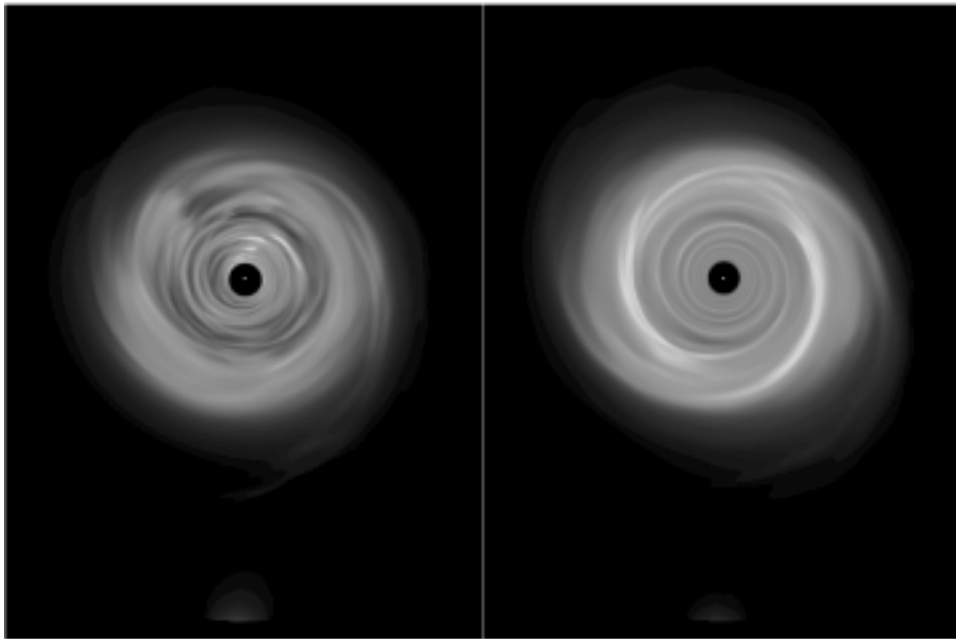


Figure 4.18: Flat ($n = 0$) profile disk (left) and medium ($n = 15/8$) profile disk (right) with tidal stream. The stream is initialized with a density to produce an incoming mass transfer rate appropriate for α at the disk's outer edge. Recall that in the medium profile case, the density is scaled by a factor of $r^{15/8}$.

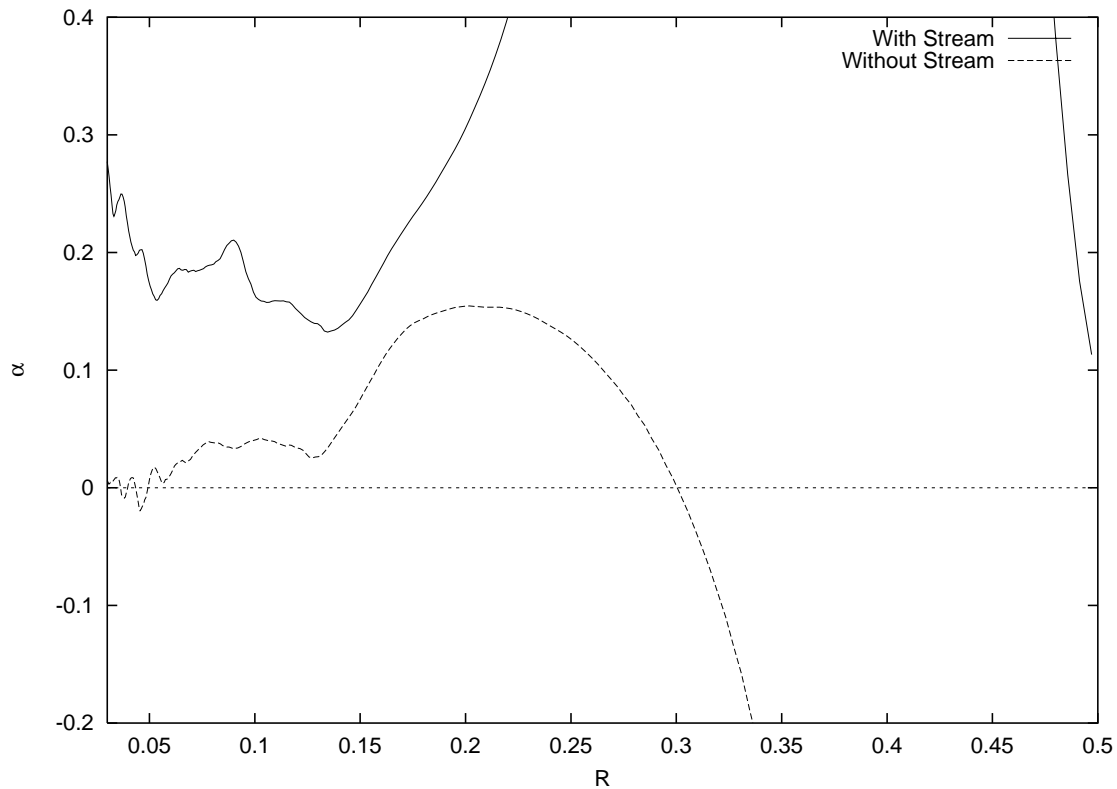


Figure 4.19: A dramatic increase in mass transport within the $n = 0$ disk is seen when the tidal stream is turned on. α is very large outside the disk due to the in-falling tidal stream. Most of the stream gas is entrained at the disk's outer edge, yet $\alpha \gtrsim 0.15$ in the interior, and ≈ 0.25 at the disk's inner edge.

entrained at the disk's outer edge. This appears to be the case to some extent; the gas stream simply does not carry enough momentum upon impact for most of it to avoid being swept up at the outer edge. The fraction of the stream mass injected at small radii is negligible. However, it is injected at large radial velocity. This makes calculation of α problematic. α should be a measure of transport due to wave modes within the disk, rather than merely a measure of mass injection.

Most interesting is the change in α due to the tidal stream. α is large outside of

the disk proper because of the tidal stream. However, within the disk, α is enhanced to $\gtrsim 0.15$ all the way down to the inner edge of the disk, even interior to the ballistic point of closest approach (≈ 0.07); inside this radius α actually rises to ~ 0.25 . Figure 4.19 shows the increase in α between two simulations with and without the tidal stream. Unfortunately, at this point we cannot disentangle α due to wave modes and stream overflow.

In contrast, Figure 4.20 shows the steeper $n = 15/8$ disk experiences almost no change in α within the disk at any radii. We postulate that the radial gradients in mass and momentum within the disk stabilize it against inward propagation of the disturbance caused by the stream impact, just as the steeper profiled disks were stable against epicyclic motions in the absence of the stream. The mass carried by the overflowing fraction of the stream gas is negligible compared to the interior disk gas in the steeper case. These effects would minimize any change in α regardless of whether we are primarily measuring wave transport or overflow, so we cannot use this result to differentiate between the two.

4.4.2 Tilted Disks

Finally, we tilt the $n = 0$ disk 10° about the line of centers, descending near the L1 point. The tilted disk was run both with and without a tidal stream, and α , the tilt angle i , and the angle of the ascending line of nodes were measured as functions of radius and time. The morphology of the disks (Figure 4.21), both with and without stream, remain very similar to the un-tilted disks. The tilted disk with stream shows the same

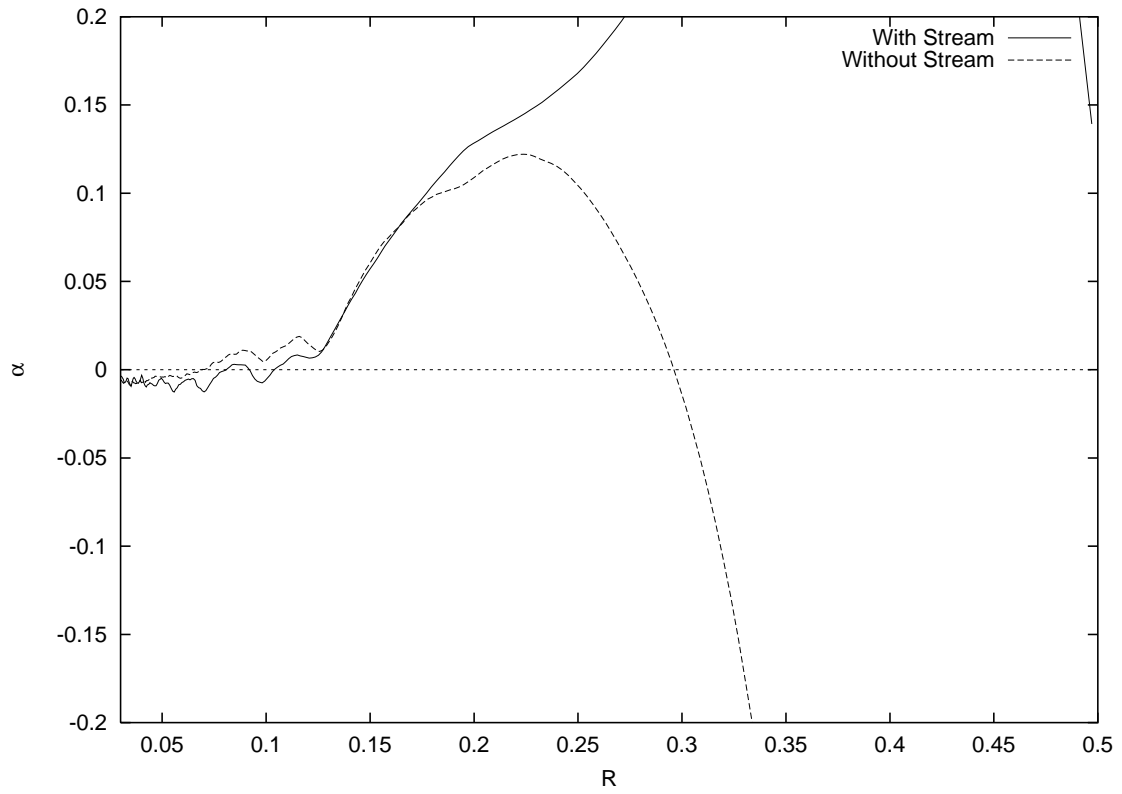


Figure 4.20: Little change is seen in the steeper $n = 15/8$ density profile disks, except for the large values of α external to the disk due to the in-falling stream.

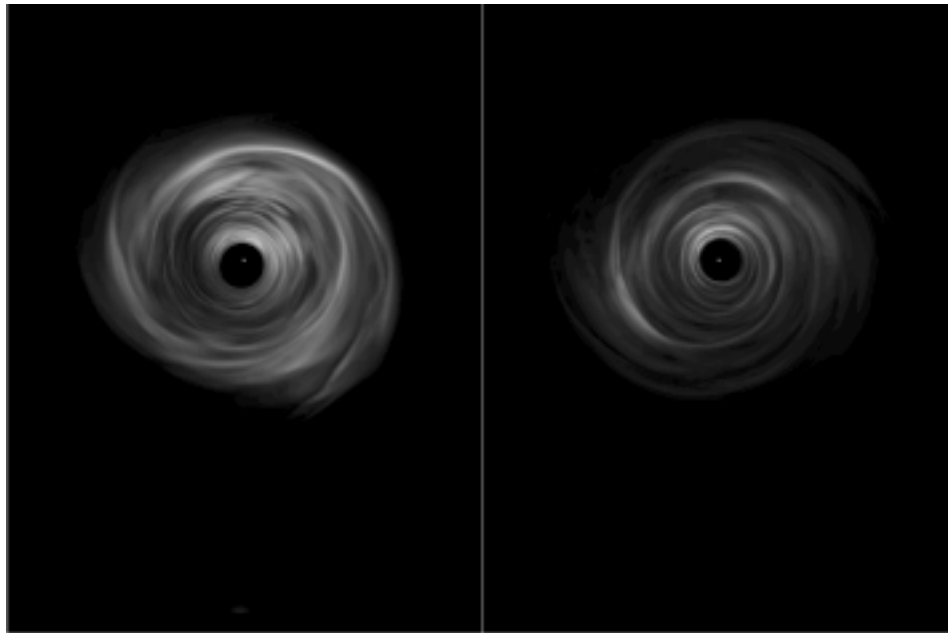


Figure 4.21: The morphology of the tilted disks remains similar to that of the un-tilted disks, including the formation and collapse of the spiral shocks, the onset of the $m = 1$ one-armed spiral and epicyclic motions, and the reinforcement of the one-armed mode by the tidal stream, including higher densities in the inner and outer disk.

behavior as the un-tilted disk with stream, with an accumulation of mass both in the disk exterior and interior. The onset of the one-armed $m = 1$ instability is the same as the un-tilted disk, as is the onset of the vertical ram pressure gradient instability within the spiral shocks. Due to the decrease in the time-step necessitated by tilting the high velocity flow within the grid, we were unable to run the tilted disk simulations for long enough to effectively measure α , although α averaged very briefly ($\approx 1/8P_{\text{orb}}$) after the initial transients had exited for the tilted disks were at least consistent with the values from the un-tilted disks.

We are able to reproduce the tidally induced precession of the disk predicted by Larwood [1998a]. Over the course of an orbital period, in the absence of precession of the disk in the inertial frame, the disk should precess exactly 2π radians in the rotating frame. We find that the disk rotates approximately 5-6% too fast in the rotating frame, corresponding to one full tidal rotation in the inertial frame about every 17-20 orbital periods. The precession is nearly rigid, with a slight radial dependence on the angle of the line of nodes that equalizes over an orbital period such that no region of the disk precesses away from another (the disk stays “connected”).

The tidal stream does affect the tidal precession period of the disk interior, with the disk interior precessing initially significantly faster than the exterior. This may be due to the change in tilt angle of the inner disk (see below). However, the angle of the line of nodes throughout the disk still equilibrates over an orbital period. If the disk interior were to become disconnected from the outer portions of the disk, then the modes presumably driving the more rapid advance could not propagate inward from the stream impact at the outer edge.

The tidal stream does have an effect on the tilt angle at the edge of the disk. The disk is initialized at a uniform tilt of 10° . After $\approx 0.5P_{\text{orb}}$, the disk without a tidal stream remains within 1° of this at all radii. However, the disk with a tidal stream has significantly increased tilt at radii smaller than $r/a \approx 0.1$; the tilt rises approximately monotonically to $\approx 13 - 14^\circ$ at the inner edge of the disk.

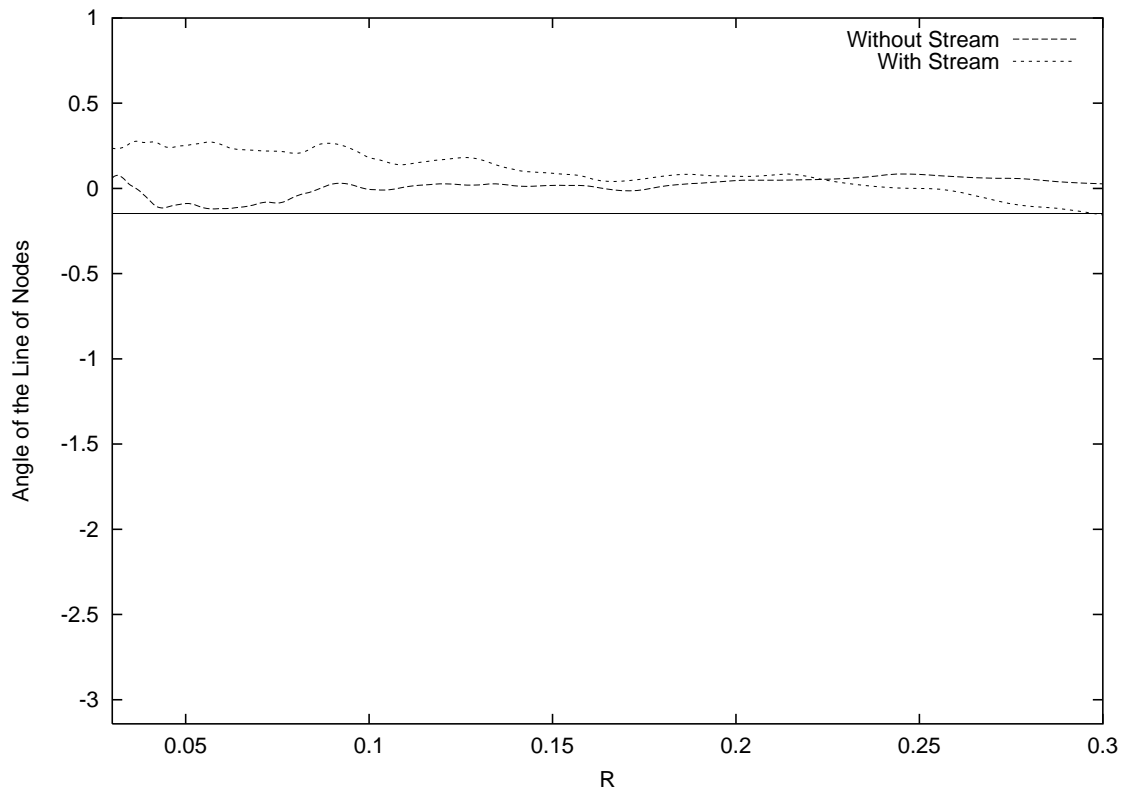


Figure 4.22: Angle of the line of nodes for the tilted disks, with and without tidal stream. The simulations were initialized with the line of nodes along $\pm\pi$; the rotating frame increases the angle during an orbital period. In the absence of tidal precession, the line of nodes should have advanced from $-\pi$ to the position of the solid line by time $t = 2.1 = 0.48P_{\text{orb}}$. However, the line of nodes has advanced beyond this point, indicating tidal precession of the tilted disk. The disk completes a full rotation in the rotating frame approximately 5 – 6% too rapidly, indicating a precession period of $\approx 17 - 20P_{\text{orb}}$.

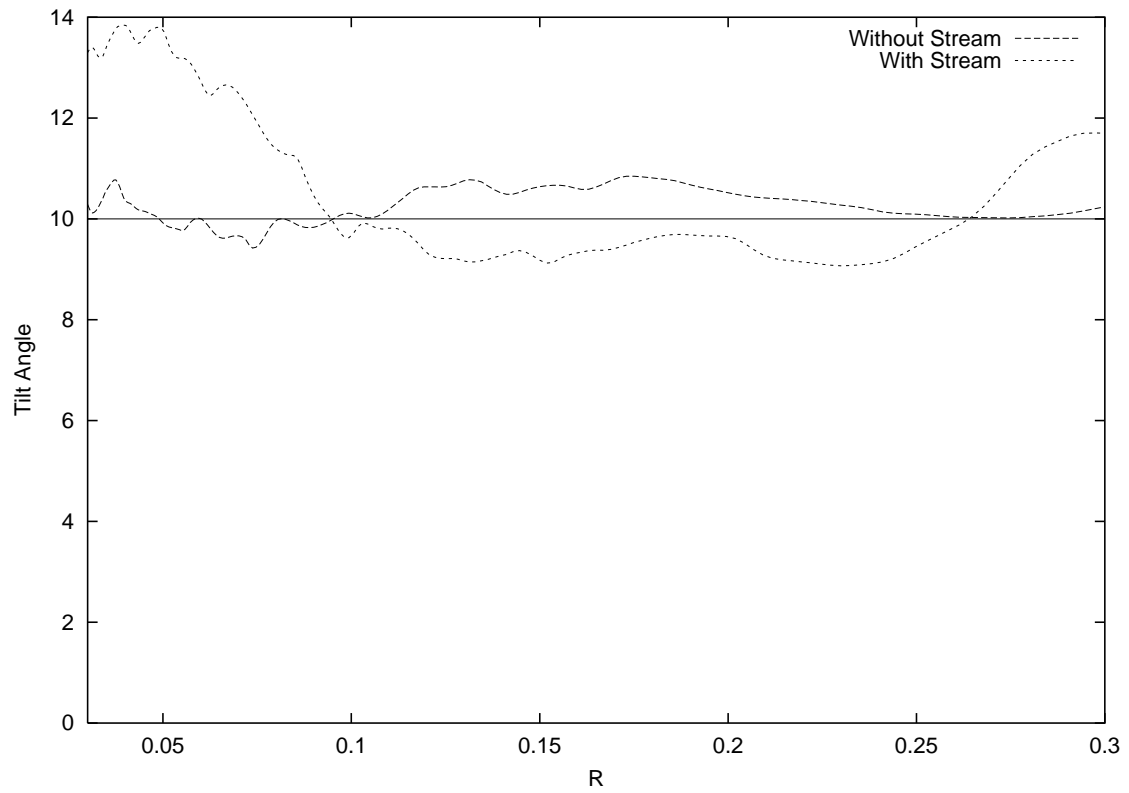


Figure 4.23: The tilt angle of the disk without stream remains within 1° of the initialized value at $0.5P_{\text{orb}}$. However, the disk with a tidal stream shows a dramatic increase in the disk tilt in the disk interior.

4.5 Discussion

We have undertaken high resolution 3D simulations of accretion disks in a binary potential, and find that the clean spiral shocks observed in 2D are unstable in 3D to vertical gradients in the velocity field of the flow. We find that α remains high (≈ 0.15) in the outer half of the disk, but diminishes rapidly with decreasing radius, in good agreement with the 2D simulations of Blondin [2000]. We find the transport in the flat density profile disk to be significantly enhanced above that of the steeper density profile disks ($\alpha \approx 0.03$ for the flat disk compared to $\alpha \approx 0.01$ for the medium disk) for moderately small radii ($0.07 \lesssim r/a \lesssim 0.13$). We were unable to run our simulations for a sufficient length of time for α at very small radii ($r/a \lesssim 0.05$) to converge, except in the steepest $n = 3$ disk. This is most significant for all disks without tidal streams, where we are unable to say with certainty that the sign of α remains consistently positive for small radii.

We observe epicyclic motions of the inner disk at a frequency of approximately four times the binary orbital frequency in the flat profile disk that are not observed in the steeper disks. We theorize this to be due to the mass and angular momentum profiles within the steeper disk stabilizing them against epicyclic motions. In the steeper disks, the low mass, low angular momentum outer annuli that experience the largest tidal forces are unable to dominate the motions of the massive, high momentum inner annuli. In the flat disk both the mass and angular momentum of successive annuli increase with radius. Hence the most massive portions of the disk feel the greatest tidal forcing.

It may be the case that resonant coupling at varying radii within the disk causes α

to not be monotonic; Figures 4.11 and 4.12 show consistent radial bands of alternately enhanced and diminished transport across all density profiles. After a long time this could conceivably lead to radial striping of the disk, but our simulations, covering only a few orbital periods, are unable to determine this.

We further find that the inclusion of the tidal stream in the flat profile disk dramatically increases α , up to ≈ 0.25 all the way to the inner disk edge. However, we are unable to distinguish whether this represents an actual increase in the efficiency of mass transport due to hydrodynamic wave modes, or simply represents the injection of high radial-velocity material from the overflowing tidal stream. This effect is not seen in the steeper profile disks, where only negligible enhancement is seen. We feel that this also may be due to the radial mass and angular momentum gradients; the disturbance due to the tidal stream impact is unable to propagate into the inner disk in the steep simulations, whereas the disturbance can easily propagate into the less massive, low momentum inner disk in the flat simulation. It could also represent the negligible magnitude of the momentum carried by the stream compared to the disk interior in the steep disk, and thus this cannot be used to differentiate which mechanism is affecting α in the flat disk. This result could be particularly interesting in light of the fact that we may expect physical disks to be closer to a flat density profile in our regime of interest than not, given previous 2D and 3D simulations of accretion disk formation (Chapter 3), but until we can disentangle transport due to wave modes and mass injection at small radii, we cannot say.

We observe tidal thickening and thinning of the outer disk due to vertical resonance

in good agreement with Ogilvie [2002].

Given that the apparent instability of spiral shocks to vertical ram pressure gradients yields both a lower ratio of gas density immediately behind the spiral shocks to the gas density between them and also increased energy dissipation between them due to vertically traveling shocks within the disk, it may be the case that the signal-to-noise ratio of spiral structure within accretion disks may be lower than might otherwise be expected. This could make detection of spiral structure in close binary accretion disks more difficult to detect via Doppler tomograms, so far the only method of even indirectly imaging disks in close binaries.

It is worth contemplating what effects a more physical disk model would have on this instability. In a physical disk, energy cannot simply be radiated away within the spiral shocks. It is likely that the shocks would be “puffed up” vertically, creating an even greater horizontal pressure overbalance for the incoming flow. Hence we expect this effect to be even stronger in physical disks. We can envision no restoring force that prevents the vertical collapse of the spiral shocks. However, it is possible that at late times a more stable equilibrium vertical structure of the spiral shocks could arise; further numerical work is needed to extend these simulations over many orbital periods to ascertain this.

Coupled with our finding that the disk rim is tidally thickened, the apparent decrease in the signal-to-noise ratio of shock detectability could be interpreted to support Ogilvie’s postulation that observed spiral structure may not be tidally-induced spiral shocks, but rather differential illumination of a tidally thickened outer disk. However, since we find

the spiral shocks and tidal bulging within the outer disk to be concomitant, we feel it is unlikely that one mechanism is operating in the absence of the other; it is likely that both effects occur in systems with observed spiral-like structure.

We show that the Reynolds stress $W_{R\phi}$, being a local transport metric, is not an adequate measure of transport due to global wave modes within the disk, hence transportation due to these modes, including spiral shocks, cannot be so easily dismissed. In their study of the role of the MRI in gap formation in protoplanetary disks, Winters et al. [2003] found that under certain circumstances, planets within the disk drove strong spiral shocks into it. In the presence of these spiral shocks, they found the Maxwell stress was heavily damped, with magneto-hydrodynamically driven transport curtailed by as much as 90%. While it is unclear whether or not this would hold true for all field configurations, it is interesting to posit a scenario in which global hydrodynamic modes drive accretion in the outer regions of a cold disk where the MRI may be ineffective, especially in light of our findings that the tidal stream impact may increase α to ~ 0.25 down to radii as small as $r/a \approx 0.03$. Deep within the disk, as accretion due to global HD modes shuts off due to the increasingly oblique shock angle and decreasing efficiency of the shocks to drive transport, the spiral modes fade away, and the MRI may operate unhindered. These two regimes, operating via completely different accretion mechanisms, cannot be expected a priori to match smoothly, and an impedance mismatch may be expected where mass could accumulate within a ring. Mass might accumulate until the critical surface density is reached for the disk to become thermally unstable and switch to the hot branch, where the higher ionization state might allow the MRI to operate

more efficiently, sustaining high accretion rates and flushing the disk in outburst. Such a two regime model provides a natural mechanism for accumulating material in a ring and then flushing it via an increased accretion rate during outburst, and could be applicable in cataclysmic variable stars and soft X-ray transients.

Finally, we find that the formation and morphology of the spiral modes, both $m = 2$ and $m = 1$, are similar in our tilted disks and un-tilted disks. We find our precession period of $17 - 20P_{\text{orb}}$ to be in excellent agreement with the analytic prediction of $P_{\text{prec}} \approx 20.4P_{\text{orb}}$ from Equation 1.2.

We show a rapid and dramatic increase of the tilt angle at small radii when the tidal stream is included. We feel that the excellent conservation of the tilt angle in the absence of a tidal stream indicates that this is not a numerical effect due to worsening vertical resolution at small radii, but a real consequence of the stream striking a tilted disk. However, we recall that the tilted disk simulations did not extend long enough in time to follow the behavior of the tilt for an extended period. For example, it may be the case that the stream acts to increase the tilt during some one binary phases, and decrease it during others, when the incidence angle has changed. Hence we cannot generally infer the long term impact on the tilt angle due to the tidal stream. Even with these caveats, however, it is significant that the tilt angle can vary so significantly on the short term, completely in absence of any other warping mechanism, such as re-radiation back-pressure.

Chapter 5

Conclusions

5.1 Mass Transfer and Accretion in High Mass X-Ray Binaries

5.1.1 Wind Accretion *vs.* Roche Lobe Overflow

We present a series of time-dependent 2D and 3D numerical simulations illustrating the evolutionary sequence between high mass X-ray binaries fed by wind accretion (where the primary star sits well within its critical tidal lobe) and those fed by Roche lobe overflow (where the primary star extends out to its tidal lobe). We define the RLOF parameter λ as the ratio of the surface potential to the critical potential.

When the primary lies well within its critical surface we find negligible tidal mass loss enhancement, and a system that is characterized by wind accretion with the development of a photoionization zone around the compact object. As the surface of the primary nears the critical surface, we observe tidally enhanced mass loss via a thin tidal stream, resulting in higher accretion wake densities. For full RLOF we observed the development of a steady accretion disk characterized by a total shadowing of the X-rays in the orbital

plane.

$\dot{M}(t)$ and $L_x(t)$ vary as an exponential in the RLOF regime, simply following the exponential atmosphere of the donor. A sharp transition then leads to the wind accretion regime, with much lower X-ray luminosities, although the L_x is underestimated for the wind regime due to the restriction to 2D and the assumption of an accretion scale-height appropriate for disk accretion. The transition case is characterized by much larger typical variations in the mass accretion rate and X-ray luminosity, due to the non-linear feedback between a weak stream and the accretion bow shock.

Although we expect the exact mass accretion rates and the position of the transitional case to change in 3D, we feel that our results explain the sharp distinction between the wind fed and disk fed HMXBs, and the lack of transitional cases, due to the sharpness of the transition regime and the expected lifetimes of HMXBs.

5.1.2 Mass Transfer in Elliptical Orbit X-Ray Binaries

High mass X-ray binary star systems with elliptical orbits, like GX 301-2, often exhibit a peak in X-ray luminosity associated with periastron passage. We use a two dimensional hydrodynamics code to examine the possibility that these X-ray flares result from tidal stripping of gas from the primary star, and subsequent accretion of this gas onto the compact companion. We find that if the primary star is rotating near corotation with the orbiting compact companion at periastron, tidally stripped gas can accrete, causing X-ray flares. Such a tidally induced flare will occur substantially after periastron, at a phase of ~ 0.2 for the parameters used in our model. This flare is characterized by a

brief disk accretion phase with a large angular momentum accretion rate. However, in our particular model this disk accretion phase was followed by an equally brief phase of accretion with the opposite sign of angular momentum, resulting in no long-term spin up of the X-ray pulsar.

5.1.3 Global Hydrodynamic Simulations of LMC X-4

We present the first global, three dimensional hydrodynamic simulations of Roche lobe overflow (RLOF) and accretion disk dynamics in an HMXB. We use the observed parameters of LMC-X4, a disk-fed X-ray binary undergoing full Roche lobe overflow. We include the Sobolev approximation to the radiatively driven primary wind, as well as first order radiative transfer of a time-dependent, self-consistent X-ray luminosity from the X-ray pulsar. The simulation is initialized with a Roche-filling geometry and a smooth CAK-type wind solution. The simulation is allowed to form its own tidal stream and accretion disk; sufficient time is allowed for the disk to reach a dynamical equilibrium. A disk of compressed primary wind also forms in the orbital plane due to the closeness of the binary orbit and the assumption of co-rotation. The stream is thicker than the accretion disk as it enters, merging with the disk material near the neutron star on the rear (opposite the primary) side. The convergent stream material generates strong spiral shocks within the disk. The simulation sustains Eddington and super-Eddington accretion rates. A fast, low density wind is driven radiatively from the surface of the accretion disk by the X-rays in the vicinity of the neutron star. This wind completely dominates any thermally driven wind that arises due to X-ray illumination of the primary surface.

Predictions of our hydrodynamic model were compared with UV P Cygni line profiles from the Goddard High Resolution Spectrograph and Space Telescope Imaging Spectrograph aboard the Hubble Space Telescope. The model determined the density and velocity fields of the stellar wind, wind-compressed disk, tidal stream, accretion disk, and X-ray illumination winds from both the disk and donor surface. A Monte Carlo code was used in post-processing of the hydrodynamic model data to determine the UV P Cygni line profiles by simulating the radiative transfer of UV photons that originate on the star and are scattered in the wind. The qualitative orbital variation predicted by the model is similar to that observed, although the model fails to reproduce the strong orbital asymmetry. The model predicts a mid-eclipse X-ray flux a factor of 4 smaller than observed with ASCA. The peak velocity is observed at the incorrect phase. The failings of the model are likely due to three factors: limited extent in the radial coordinate did not allow trailing accretion and photoionization wakes to propagate to sufficiently late phase to reproduce the observed absorption; limited numerical resolution near the accretor may have artificially restricted the X-ray illuminated region and thus lowered the scattered X-ray flux; the terminal wind velocity of $\approx 2000 \text{ km sec}^{-1}$ was too fast, allowing the wind to accelerate to the artificially truncated outer edge with an un-realistic velocity profile.

5.2 3D Hydrodynamic Disks

We have undertaken high resolution 3D simulations of isothermal disks in a binary potential, both with and without tidal streams, as well as with tilted disks. We have found

that tidally-driven spiral shocks within close binary accretion disks may be unstable to gradients in the vertical ram pressure of the disk flow. A z -dependence of the Keplerian velocity leads to a gradient in the ram pressure that allows the gas pressure behind the shock to displace the shock forward into the oncoming flow. This leads to an increase in the obliquity of the shock to the incoming fluid, which lowers the ram pressure, which tilts the shock further, which lowers the ram pressure, etc. in a feedback loop that eventually results in the inversion of the vertical pressure gradient. Vertical hydrostatic equilibrium is broken, and the wings of the spiral shock come crashing down into the plane, driving vertically traveling shocks through the disk between the spirals. This results in a significantly noisier disk, with increased density and dissipation between the spiral shocks as compared to within them. This may lower the signal-to-noise ratio of spiral shock detection with observational implications.

We find differential vertical tidal thickening and thinning of the disk in its outer rim, and confirm qualitatively and quantitatively Ogilvie's spiral-like sheared $m = 2$ vertical thickening mode. This may lend support to the notion that observed spiral structure may not be observations of spiral shocks but rather differential illumination of the outer disk rim. However, we feel it is likely that both mechanisms, spiral shocks and tidal thickening, will be operating in systems with observed spiral-like structure.

The flat density profile simulation was susceptible to large-scale epicyclic motions of the inner disks, with the inner disk edge precessing with a frequency of four times the binary orbital frequency, and the transformation to an $m = 1$ one-armed spiral mode. Simulations with steeper density profiles, while exhibiting small epicyclic motion

in the measurement of α did not exhibit this behavior. We believe that the flat density profile is susceptible to this mode because the surface density and angular momentum of successive annuli increase with radius, allowing portions of the disk at larger radii where tidal torques are stronger to more easily drive the light-weight, low momentum inner disk. Steeper density profile disks are not susceptible to this because the outer regions of the disk where tidal forces are strong carry relatively little inertia compared to the inner disk.

Without a tidal stream, we find significant transport in the outer half of the disk ($\alpha \approx 0.1$ – 0.15) where tidal forces are strongest, steady but lower transport down to $1/3$ the disk radius ($\alpha \approx 0.03$ for the $n = 0$ case), and α not yet converged at smaller radii for disks shallower than the steepest $n = 3$ case. We find α at medium radii to be strongly dependent on the density profile of the disk, with the steepest disk showing an order of magnitude less transport than the flat disk between one third and one half the disk radius. We find that $\alpha(r, t)$ exhibits period doubling behavior with radial bands transporting synchronously at radii where the gas orbital frequency is resonant with the binary orbital frequency.

We show that inclusion of a tidal stream dramatically enhances α at small radii within the flat disk. In our flat density profile disk with a tidal stream we find $\alpha \gtrsim 0.15$ in the disk interior, rising to ≈ 0.25 at the disk's inner edge. Negligible transport enhancement is seen in the steeper disks. We are unable to differentiate between higher α due to enhanced transport via wave modes and injection of low density, high radial velocity overflowing stream gas.

We show that $W_{R\phi}$, the $R\phi$ component of the Reynolds stress, a measure of hydrodynamic transport due to local processes, is not an adequate measure of accretion due to global hydrodynamic wave modes, and hence transport due to these modes cannot be casually dismissed.

Finally, we speculate that a two-regime model of strong accretion in the outer regions of the disk due to global hydrodynamic modes coupled with strong magnetohydrodynamic turbulence-driven accretion at smaller radii could provide a natural physical mechanism for the accumulation of mass and accretion change-of-state required by some CV and SXT models.

Finally, we find that the morphology of our tilted disks is similar to the un-tilted disks, in terms of the formation and collapse of the tidally driven spiral shocks, and the enhancement of the natural one-armed spiral mode in the presence of a tidal stream for the flat density profile cases. We find a tidal precession period in excellent agreement with analytic predictions, and find that the stream impact can have a significant short-term impact on the tilt angle, completely via hydrodynamic modes, without the inclusion of any other warp-driving mechanism.

Bibliography

D. C. Abbott. The theory of radiatively driven stellar winds. I - A physical interpretation. *The Astrophysical Journal*, 242:1183–1207, December 1980.

P. J. Armitage and J. R. Murray. Simulations of spiral structure in the accretion disc of IP Pegasi during outburst. *Monthly Notices of the Royal Astronomical Society*, 297:L81–L85, July 1998.

Y. Avni and I. Goldman. A discussion of the eccentric binary hypothesis for transient X-ray sources. II - Gradual acceleration stellar wind model. *Astronomy and Astrophysics*, 90:44–47, October 1980.

S. A. Balbus and J. F. Hawley. Instability, turbulence, and enhanced transport in accretion disks. *Reviews of Modern Physics*, 70:1–53, January 1998.

R. Baptista, E. T. Harlaftis, and D. Steeghs. Eclipse maps of spiral shocks in the accretion disc of IP Pegasi in outburst. *Monthly Notices of the Royal Astronomical Society*, 314:727–732, June 2000.

R. Baptista, K. Horne, R. A. Wade, I. Hubeny, K. S. Long, and R. G. M. Rutten. HST spatially resolved spectra of the accretion disc and gas stream of the nova-like variable

UX Ursae Majoris. *Monthly Notices of the Royal Astronomical Society*, 298:1079–1091, August 1998.

G. Belvedere and G. Lanzafame. SPH Simulations of Spiral Shocks in Discs around Black Holes. *Publ. of the Astronomical Society of Japan*, 54:781–785, October 2002.

J. E. Bjorkman and J. P. Cassinelli. Equatorial disk formation around rotating stars due to Ram pressure confinement by the stellar wind. *The Astrophysical Journal*, 409:429–449, May 1993.

J. M. Blondin. The shadow wind in high-mass X-ray binaries. *The Astrophysical Journal*, 435:756–766, November 1994.

J. M. Blondin. Tidally-driven transport in accretion disks in close binary systems. *New Astronomy*, 5:53–68, April 2000.

J. M. Blondin, T. R. Kallman, B. A. Fryxell, and R. E. Taam. Hydrodynamic simulations of stellar wind disruption by a compact X-ray source. *The Astrophysical Journal*, 356:591–608, June 1990.

J. M. Blondin and M. P. Owen. Wind Accretion VS Roche Lobe Overflow in HMXBs. In *ASP Conf. Ser. 121: IAU Colloq. 163: Accretion Phenomena and Related Outflows*, pages 361–+, 1997.

J. M. Blondin, I. R. Stevens, and T. R. Kallman. Enhanced winds and tidal streams in massive X-ray binaries. *The Astrophysical Journal*, 371:684–695, April 1991.

J. M. Blondin and J. W. Woo. Wind dynamics in SMC X-1. 1: Hydrodynamic simulation. *The Astrophysical Journal*, 445:889–895, June 1995.

- H. Bondi and F. Hoyle. On the mechanism of accretion by stars. *Monthly Notices of the Royal Astronomical Society*, 104:273–+, 1944.
- B. Boroson, T. Kallman, J. M. Blondin, and M. P. Owen. Testing Hydrodynamic Models of LMC X-4 with Ultraviolet and X-Ray Spectra. *The Astrophysical Journal*, 550:919–930, April 2001.
- B. Boroson, T. Kallman, R. McCray, S. D. Vrtilek, and J. Raymond. Models of X-Ray Photoionization in LMC X-4: Slices of a Stellar Wind. *The Astrophysical Journal*, 519:191–205, July 1999.
- C. B. Boyle and I. W. Walker. Numerical simulation of mass transfer in eccentric orbit binary systems. *Monthly Notices of the Royal Astronomical Society*, 222:559–568, October 1986.
- J. I. Castor, D. C. Abbott, and R. I. Klein. Radiation-driven winds in Of stars. *The Astrophysical Journal*, 195:157–174, January 1975.
- M. A. Chichkov, R. A. Syunyaev, I. Y. Lapshov, N. Lund, S. Brandt, and A. Castro-Tirado. WATCH/GRANAT observations of the x-ray pulsar GX 301-2. *Astronomy Letters*, 21:435–441, July 1995.
- M. Clampin, J. E. Krist, D. R. Ardila, D. A. Golimowski, G. F. Hartig, H. C. Ford, G. D. Illingworth, F. Bartko, N. Benítez, J. P. Blakeslee, R. J. Bouwens, T. J. Broadhurst, R. A. Brown, C. J. Burrows, E. S. Cheng, N. J. G. Cross, P. D. Feldman, M. Franx, C. Gronwall, L. Infante, R. A. Kimble, M. P. Lesser, A. R. Martel, F. Menanteau, G. R. Meurer, G. K. Miley, M. Postman, P. Rosati, M. Sirianni, W. B. Sparks, H. D. Tran,

- Z. I. Tsvetanov, R. L. White, and W. Zheng. Hubble Space Telescope ACS Coronagraphic Imaging of the Circumstellar Disk around HD 141569A. *The Astronomical Journal*, 126:385–392, July 2003.
- P. Colella and P. R. Woodward. The Piecewise Parabolic Method (PPM) for Gas-Dynamical Simulations. *Journal of Computational Physics*, 54:174–201, 1984.
- M. de Kool and D. Wickramasinghe. Thermal instability and evaporation of accretion disc atmospheres. *Monthly Notices of the Royal Astronomical Society*, 307:449–458, August 1999.
- A. K. Dupree, H. Gursky, J. H. Black, R. J. Davis, L. Hartmann, T. Matilsky, J. C. Raymond, G. Hammerschlag-Hensberge, E. P. J. van den Heuvel, M. Burger, H. J. G. L. M. Lamers, P. A. vanden Bout, D. C. Morton, C. de Loore, E. L. van Dessel, J. W. Menzies, P. A. Whitelock, M. Watson, P. W. Sanford, and G. S. G. Pollard. Simultaneous ultraviolet, optical, and X-ray observations of the X-ray source VELA X-1 /HD 77581/. *The Astrophysical Journal*, 238:969–981, June 1980.
- A. Feldmeier, U. Anzer, G. Boerner, and F. Nagase. VELA X-1: how to produce asymmetric eclipses. *Astronomy and Astrophysics*, 311:793–802, July 1996.
- J. Frank, A. King, and D. J. Raine. *Accretion Power in Astrophysics: Third Edition*. *Accretion Power in Astrophysics: Third Edition*, by Juhan Frank, Andrew King, and Derek J. Raine. Cambridge University Press, 2002, 398 pp., 2002.
- C. Fransson and A. C. Fabian. X-ray induced shocks in stellar winds. *Astronomy and Astrophysics*, 87:102–108, July 1980.

- D. B. Friend and D. C. Abbott. The theory of radiatively driven stellar winds. III - Wind models with finite disk correction and rotation. *The Astrophysical Journal*, 311: 701–707, December 1986.
- P. Godon. Numerical Modeling of Tidal Effects in Polytropic Accretion Disks. *The Astrophysical Journal*, 480:329–+, May 1997.
- P. Godon, M. Livio, and S. Lubow. Spiral shocks in accretion discs. *Monthly Notices of the Royal Astronomical Society*, 295:L11–L14, March 1998.
- P. Goldreich and S. Tremaine. Disk-satellite interactions. *The Astrophysical Journal*, 241:425–441, October 1980.
- D. E. Gruber and R. E. Rothschild. SMC X-1 variability observed from HEAO 1. *The Astrophysical Journal*, 283:546–551, August 1984.
- F. Haberl. The X-ray properties of GX 301 - 2 (4U 1223 - 62). *The Astrophysical Journal*, 376:245–255, July 1991.
- F. Haberl, N. E. White, and T. R. Kallman. An EXOSAT X-ray observation of one orbital cycle of 4U 1700-37/HD 153919. *The Astrophysical Journal*, 343:409–425, August 1989.
- S. Hatchett and R. McCray. X-ray sources in stellar winds. *The Astrophysical Journal*, 211:552–561, January 1977.
- S. R. Heap and M. F. Corcoran. Properties of the massive X-ray binary 4U 1700 - 37 = HD 153919. *The Astrophysical Journal*, 387:340–346, March 1992.

- M. H. M. Heemskerk and J. van Paradijs. Analysis of the optical light curve of the massive X-ray binary LMC X-4. *Astronomy and Astrophysics*, 223:154–164, October 1989.
- C. Ho and J. Arons. Fluctuation of wind-driven accretion in X-ray binaries. *The Astrophysical Journal*, 321:404–417, October 1987.
- D. W. Hoard, P. Szkody, A. Linnell, K. Long, E. M. Sion, I. Hubeny, and C. Knigge. Observations of Novalike Cataclysmic Variables with the Far Ultraviolet Spectroscopic Explorer. *American Astronomical Society Meeting*, 201:0–+, December 2002.
- R. C. Iping and J. A. Petterson. Quasi-periodic precession of disks in X-ray binaries, with possible application to Centaurus X-3. *Astronomy and Astrophysics*, 239:221–226, November 1990.
- M. A. Jimenez-Garate, C. J. Hailey, J. W. d. Herder, S. Zane, and G. Ramsay. High-Resolution X-Ray Spectroscopy of Hercules X-1 with the XMM-Newton Reflection Grating Spectrometer: CNO Element Abundance Measurements and Density Diagnostics of a Photoionized Plasma. *The Astrophysical Journal*, 578:391–404, October 2002.
- P. Kahabka and X.-D. Li. The recent pulse period evolution of SMC X-1. *Astronomy and Astrophysics*, 345:117–120, May 1999.
- L. Kaper, G. Hammerschlag-Hensberge, and J. T. van Loon. Observations of stellar winds in high-mass X-ray binaries: Evidence for a non-monotonic velocity structure. *Astronomy and Astrophysics*, 279:485–498, November 1993.

- L. Kaper, G. Hammerschlag-Hensberge, and E. J. Zuiderwijk. Spectroscopic evidence for photo-ionization wakes in VELA X-1 and 4U 1700–37. *Astronomy and Astrophysics*, 289:846–854, September 1994.
- L. Kaper, H. J. G. L. M. Lamers, E. Ruymaekers, E. P. J. van den Heuvel, and E. J. Zuidervijk. Wray 977 (GX 301-2): a hypergiant with pulsar companion. *Astronomy and Astrophysics*, 300:446–452, August 1995.
- J. I. Katz. Hercules X-1-Model for the 35-d periodicity. *Nature Physical Science*, 246:87–+, December 1973.
- R. L. Kelley, J. G. Jernigan, A. Levine, L. D. Petro, and S. Rappaport. Discovery of 13.5 S X-ray pulsations from LMC X-4 and an orbital determination. *The Astrophysical Journal*, 264:568–574, January 1983.
- D. T. Koh, L. Bildsten, D. Chakrabarty, R. W. Nelson, T. A. Prince, B. A. Vaughan, M. H. Finger, R. B. Wilson, and B. C. Rubin. Rapid Spin-up Episodes in the Wind-fed Accreting Pulsar GX 301-2. *The Astrophysical Journal*, 479:933–+, April 1997.
- J. H. Krolik and T. R. Kallman. Soft X-ray opacity in hot and photoionized gases. *The Astrophysical Journal*, 286:366–370, November 1984.
- P. Kumar, C. O. Ao, and E. J. Quataert. Tidal Excitation of Modes in Binary Systems with Applications to Binary Pulsars. *The Astrophysical Journal*, 449:294–+, August 1995.
- F. L. Lang, A. M. Levine, M. Bautz, S. Hauskins, S. Howe, F. A. Primini, W. H. G. Lewin, W. A. Baity, F. K. Knight, R. E. Rotschild, and J. A. Petterson. Discovery of

a 30.5 day periodicity in LMC X-4. *The Astrophysical Journal Letters*, 246:L21–L25, May 1981.

R. B. Larson. The evolution of protostellar disks. In *The Formation and Evolution of Planetary Systems*, pages 31–48, 1989.

R. B. Larson. Non-linear acoustic waves in discs. *Monthly Notices of the Royal Astronomical Society*, 243:588–592, April 1990.

J. Larwood. On the precession of accretion discs in X-ray binaries. *Monthly Notices of the Royal Astronomical Society*, 299:L32+, September 1998a.

J. Larwood. On the precession of accretion discs in X-ray binaries. *Monthly Notices of the Royal Astronomical Society*, 299:L32+, September 1998b.

J. T. Layton, J. M. Blondin, M. P. Owen, and I. R. Stevens. Tidal mass transfer in elliptical-orbit binary stars. *New Astronomy*, 3:111–119, December 1997.

D. A. Leahy. Evidence for a gas stream in GX301 - 2. *Monthly Notices of the Royal Astronomical Society*, 250:310–313, May 1991.

D. A. Leahy. Modelling RXTE/ASM observations of the 35-d cycle in Her X-1. *Monthly Notices of the Royal Astronomical Society*, 334:847–854, August 2002.

D. A. Leahy. Modelling the extreme ultraviolet emission during the low state of Hercules X-1. *Monthly Notices of the Royal Astronomical Society*, 342:446–452, June 2003.

D. N. C. Lin, J. C. B. Papaloizou, and G. J. Savonije. Propagation of tidal disturbance in gaseous accretion disks. *The Astrophysical Journal*, 365:748–756, December 1990.

- Q. Z. Liu, J. van Paradijs, and E. P. J. van den Heuvel. A catalogue of low-mass X-ray binaries. *Astronomy and Astrophysics*, 368:1021–1054, March 2001.
- S. H. Lubow and F. H. Shu. Gas dynamics of semidetached binaries. *The Astrophysical Journal*, 198:383–405, June 1975.
- S. H. Lubow and F. H. Shu. Gas dynamics of semidetached binaries. II - The vertical structure of the stream. *The Astrophysical Journal Letters*, 207:L53–L55, July 1976.
- L. B. Lucy and R. L. White. X-ray emission from the winds of hot stars. *The Astrophysical Journal*, 241:300–305, October 1980.
- D. Lynden-Bell and A. J. Kalnajs. On the generating mechanism of spiral structure. *Monthly Notices of the Royal Astronomical Society*, 157:1–+, 1972.
- K. B. MacGregor, L. Hartmann, and J. C. Raymond. Radiative amplification of sound waves in the winds of O and B stars. *The Astrophysical Journal*, 231:514–523, July 1979.
- K. B. MacGregor and P. A. J. Vitello. Stellar winds in binary X-ray systems. *The Astrophysical Journal*, 259:267–281, August 1982.
- K. Makishima, N. Kawai, K. Koyama, N. Shibasaki, F. Nagase, and M. Nakagawa. Discovery of a 437.5-s X-ray pulsation from 4U 1907 + 09. *Publ. of the Astronomical Society of Japan*, 36:679–689, 1984.
- M. Makita, H. Fujiwara, T. Matsuda, and H. M. J. Boffin. Spiral Shocks in an Inviscid Simulation of Accretion Flow in a Close Binary System. In *Astrotomography, Indirect Imaging Methods in Observational Astronomy*, pages 88–+, 2001.

- M. Makita, K. Miyawaki, and T. Matsuda. Two- and three-dimensional numerical simulations of accretion discs in a close binary system. *Monthly Notices of the Royal Astronomical Society*, 316:906–916, August 2000.
- E. Maoz and C. F. McKee. Doppler Shift Asymmetry in High-Velocity Maser Emission from Shocks in Circumnuclear Disks. *The Astrophysical Journal*, 494:218–+, February 1998.
- B. Margon, S. A. Grandi, R. Downes, H. C. Ford, L. H. Aller, M. Plavec, R. P. S. Stone, H. Spinrad, J. Stauffer, E. M. Burbidge, V. T. Junkkarinen, A. T. Koski, and H. E. Smith. The 164 and 13 Day Periods of SS 433. *Bulletin of the American Astronomical Society*, 11:671–+, June 1979.
- N. Marshall and M. J. Ricketts. Determination of a binary period for the variable X-ray source A1907+09. *Monthly Notices of the Royal Astronomical Society*, 193:7P–13P, October 1980.
- F. Mavromatakis and F. Haberl. Two Outbursts from A:0538-66 in the ROSAT All-Sky Survey. *Astronomy and Astrophysics*, 274:304–+, July 1993.
- R. McCray, T. R. Kallman, J. I. Castor, and G. L. Olson. Spectral variability in early-type binary X-ray systems. *The Astrophysical Journal*, 282:245–255, July 1984.
- H. Mendelson and T. Mazeh. Five-year photometry of V635 Cassiopeiae - The optical counterpart of 4U0115 + 63. *Monthly Notices of the Royal Astronomical Society*, 250:373–376, May 1991.
- L. Morales-Rueda and T. R. Marsh. Spectral atlas of dwarf novae in outburst. *Monthly Notices of the Royal Astronomical Society*, 332:814–826, June 2002.

- V. V. Neustroev, N. V. Borisov, H. Barwig, A. Bobinger, K. H. Mantel, D. Šimić, and S. Wolf. IP Pegasi: Investigation of the accretion disk structure. Searching evidences for spiral shocks in the quiescent accretion disk. *Astronomy and Astrophysics*, 393: 239–250, October 2002.
- K. O’Brien, K. Horne, B. Boroson, M. Still, R. Gomer, J. B. Oke, P. Boyd, and S. D. Vr-tilek. Keck II spectroscopy of mHz quasi-periodic oscillations in Hercules X-1. *Monthly Notices of the Royal Astronomical Society*, 326:1067–1075, September 2001.
- G. I. Ogilvie. Tidally distorted accretion discs in binary stars. *Monthly Notices of the Royal Astronomical Society*, 330:937–949, March 2002.
- M. P. Owen and J. M. Blondin. 3-D Hydrodynamic Simulation of Accretion Disk Formation in LMC-X4. In *ASP Conf. Ser. 121: IAU Colloq. 163: Accretion Phenomena and Related Outflows*, pages 779–+, 1997.
- S. P. Owocki, J. I. Castor, and G. B. Rybicki. Time-dependent models of radiatively driven stellar winds. I - Nonlinear evolution of instabilities for a pure absorption model. *The Astrophysical Journal*, 335:914–930, December 1988.
- S. P. Owocki and G. B. Rybicki. Instabilities in line-driven stellar winds. I - Dependence on perturbation wavelength. *The Astrophysical Journal*, 284:337–350, September 1984.
- B. Paczynski. A model of accretion disks in close binaries. *The Astrophysical Journal*, 216:822–826, September 1977.
- J. Papaloizou and J. E. Pringle. Tidal torques on accretion discs in close binary systems. *Monthly Notices of the Royal Astronomical Society*, 181:441–454, November 1977.

G. E. Parkes, J. L. Culhane, K. O. Mason, and P. G. Murdin. A spectral study of Wray 977, the optical counterpart of the binary X-ray pulsar 4U 1223-62. *Monthly Notices of the Royal Astronomical Society*, 191:547–558, May 1980.

A. N. Parmar, N. E. White, L. Stella, C. Izzo, and P. Ferri. The transient 42 second X-ray pulsar EXO 2030+375. I - The discovery and the luminosity dependence of the pulse period variations. *The Astrophysical Journal*, 338:359–372, March 1989.

A. Pauldrach, J. Puls, and R. P. Kudritzki. Radiation-driven winds of hot luminous stars - Improvements of the theory and first results. *Astronomy and Astrophysics*, 164:86–100, August 1986.

J. A. Petterson. The 35 day cycle of the X-ray binary Hercules X-1. *The Astrophysical Journal*, 218:783–791, December 1977a.

J. A. Petterson. Twisted accretion disks. I - Derivation of the basic equations. *The Astrophysical Journal*, 214:550–559, June 1977b.

J. A. Petterson. Twisted accretion disks. II - Applications to X-ray binary systems. *The Astrophysical Journal*, 216:827–837, September 1977c.

J. A. Petterson. On the occurrence of streams and disks in massive X-ray binary systems. *The Astrophysical Journal*, 224:625–630, September 1978.

S. H. Pravdo, C. S. R. Day, L. Angelini, B. A. Harmon, A. Yoshida, and P. Saraswat. ASCA and GRO Observations of GX 301-2. *The Astrophysical Journal*, 454:872–+, December 1995.

- J. E. Pringle. Self-induced warping of accretion discs. *Monthly Notices of the Royal Astronomical Society*, 281:357–361, July 1996.
- G. Ramsay, S. Zane, M. A. Jimenez-Garate, J. den Herder, and C. J. Hailey. XMM-Newton EPIC observations of Her X-1. *Monthly Notices of the Royal Astronomical Society*, 337:1185–1192, December 2002.
- M. T. Richards, G. E. Albright, and L. M. Bowles. Doppler tomography of the gas stream in short-period Algol binaries. *The Astrophysical Journal Letters*, 438:L103–L106, January 1995.
- H. Ritter and U. Kolb. Catalogue of cataclysmic binaries, low-mass X-ray binaries and related objects (Seventh edition). *Astronomy and Astrophysics*, 404:301–303, June 2003.
- W. J. Roberts. A slaved disk model for HER X-1. *The Astrophysical Journal*, 187:575–584, February 1974.
- M. Rozyczka and H. C. Spruit. Numerical Simulations of Shock-driven Accretion. *The Astrophysical Journal*, 417:677–+, November 1993.
- M. Sako, D. A. Liedahl, S. M. Kahn, and F. Paerels. The X-Ray Spectrum and Global Structure of the Stellar Wind in VELA X-1. *The Astrophysical Journal*, 525:921–934, November 1999.
- N. Sato, F. Nagase, N. Kawai, R. L. Kelley, S. Rappaport, and N. E. White. Orbital elements of the binary X-ray pulsar GX 301-2. *The Astrophysical Journal*, 304:241–248, May 1986.

- K. Sawada, T. Matsuda, and I. Hachisu. Accretion shocks in a close binary system. *Monthly Notices of the Royal Astronomical Society*, 221:679–686, August 1986a.
- K. Sawada, T. Matsuda, and I. Hachisu. Spiral shocks on a Roche lobe overflow in a semi-detached binary system. *Monthly Notices of the Royal Astronomical Society*, 219:75–88, March 1986b.
- N. Schulz, C. Canizares, J. Lee, P. Wojdowski, and W. Brandt. High Resolution Spectroscopy of Winds in Galactic X-Ray Sources. *APS Meeting Abstracts*, pages 17087–+, April 2002.
- T. Shahbaz, C. Zurita, J. Casares, G. Dubus, P. A. Charles, R. M. Wagner, and E. Ryan. The Optical Light Curves of XTE J2123-058. III. The Mass of the Binary Components and the Structure of the Quiescent Accretion Disk. *The Astrophysical Journal*, 585:443–452, March 2003.
- N. I. Shakura and R. A. Sunyaev. Black holes in binary systems. Observational appearance. *Astronomy and Astrophysics*, 24:337–355, 1973.
- F. H. Shu. Mass Transfer in Semi-Detached Binaries. In *IAU Symp. 73: Structure and Evolution of Close Binary Systems*, pages 253–+, 1976.
- G. K. Skinner, D. K. Bedford, R. F. Elsner, D. Leahy, M. C. Weisskopf, and J. Grindlay. Discovery of 69 MS periodic X-ray pulsations in A0538-66. *Nature*, 297:568–570, June 1982.
- H. C. Spruit. Stationary shocks in accretion disks. *Astronomy and Astrophysics*, 184:173–184, October 1987.

- D. Steeghs, E. T. Harlaftis, and K. Horne. Spiral structure in the accretion disc of the binary IP Pegasi. *Monthly Notices of the Royal Astronomical Society*, 290:L28–L32, September 1997.
- L. Stella, N. E. White, J. Davelaar, A. N. Parmar, R. J. Blissett, and M. van der Klis. The discovery of 4.4 second X-ray pulsations from the rapidly variable X-ray transient V0332 + 53. *The Astrophysical Journal Letters*, 288:L45–L49, January 1985.
- I. R. Stevens. An enhanced stellar wind accretion model for binary X-ray transients. *Monthly Notices of the Royal Astronomical Society*, 232:199–213, May 1988.
- M. Still, K. O'Brien, K. Horne, B. Boroson, L. G. Titarchuk, K. Engle, S. D. Vrtilik, H. Quaintrell, and H. Fiedler. Atmospheric Reflection during an Anomalous Low State of Hercules X-1. *The Astrophysical Journal*, 554:352–361, June 2001.
- G. Strang. *Journal of Numerical Analysis*, 5:506+, 1968.
- R. E. Taam and B. A. Fryxell. On nonsteady accretion in stellar wind-fed X-ray sources. *The Astrophysical Journal Letters*, 327:L73–L76, April 1988.
- R. E. Taam, A. Fu, and B. A. Fryxell. Accretion in wind-driven X-ray sources. *The Astrophysical Journal*, 371:696–707, April 1991.
- R. E. Taam and E. L. Sandquist. Common Envelope Evolution of Massive Binary Stars. *Annual Review of Astronomy and Astrophysics*, 38:113–141, 2000.
- H. Tsunemi, S. Kitamoto, and K. Tamura. Long-Term Behavior of Centaurus X-3 Observed with the All Sky Monitor on Board GINGA. *The Astrophysical Journal*, 456:316–+, January 1996.

M. P. Ulmer, W. A. Baity, W. A. Wheaton, and L. E. Peterson. Hard X-Ray Observations of Hercules X-1 by OSO-7. *The Astrophysical Journal Letters*, 178:L61+, December 1972.

S. D. Vrtilik, H. Quaintrell, B. Boroson, M. Still, H. Fiedler, K. O'Brien, and R. McCray. Multiwavelength Studies of Hercules X-1 during Short High and Anomalous Low States: On-again, Off-again. *The Astrophysical Journal*, 549:522–536, March 2001.

M. G. Watson, R. S. Warwick, and R. H. D. Corbet. The orbital period of 2S 1223-624 /GX301-2/. *Monthly Notices of the Royal Astronomical Society*, 199:915–924, June 1982.

N. E. White and J. H. Swank. The 41.5 day binary X-ray pulsar 4U 1223 - 62 (GX 301 - 2). *The Astrophysical Journal*, 287:856–867, December 1984.

W. F. Winters, S. A. Balbus, and J. F. Hawley. Gap Formation by Planets in Turbulent Protostellar Disks. *The Astrophysical Journal*, 589:543–555, May 2003.

J. W. Woo, G. W. Clark, A. M. Levine, R. H. D. Corbet, and F. Nagase. Orbital Decay, Spin-down, and Pulse-Phase-resolved Spectroscopy of LMC X-4 from GINGA and ROSAT Observations. *The Astrophysical Journal*, 467:811–+, August 1996.

P. R. Woodward and P. Colella. The Numerical Simulation of Two-Dimensional Fluid Flow with Strong Shocks. *Journal of Computational Physics*, 54:115–173, 1984.